EXPLORATION OF MIMO RADAR TECHNIQUES WITH A SOFTWARE-DEFINED RADAR

DISSERTATION

Presented in Partial Fulfillment of the Requirements for

the Degree Doctor of Philosophy in the

Graduate School of The Ohio State University

By

Mark T. Frankford, B.S.E.C.E., M.S.

Graduate Program in Electrical and Computer Engineering

The Ohio State University

2011

Dissertation Committee:

Joel T. Johnson, Adviser

Robert J. Burkholder

Emre Ertin

ABSTRACT

The application of multiple-input multiple-output (MIMO) techniques to radar has been an active research topic recently due to their successful implementation in modern wireless communications systems. Looking to further leverage this success, many researchers have studied the applicability of spatial diversity and waveform diversity to radar. It has been shown that a MIMO radar system with spatially diverse transmitters and receivers utilizing orthogonal waveforms can provide benefits in target detection and parameter estimation when compared to a traditional phased array system. The current research typically attempts to apply the Swerling-I model when analyzing the performance of the multistatic MIMO system. However, this model was originally developed for monostatic systems and may not accurately describe the bistatic scattering behavior of targets. Other research has shown that MIMO arrays with co-located transmitters and receivers could be used in imaging applications by forming virtual arrays of elements. It has been suggested that time diversity be used to unambiguously separate the transmitted waveforms at the receivers. The application of suitable transmit waveforms which could be measured simultaneously and then separated by matched filtering could extend the usefulness of the virtual array idea.

This dissertation explores MIMO concepts using both co-located and spatially diverse transmitters and receivers. A new target scattering model is presented which

extends the Swerling-I model to include a new correlation parameter. This parameter allows the bistatic scattering behavior of the model to be tuned to more accurately represent some classes of real-world targets. It is shown through simulation that increasing the amount of correlation in the target effectively decreases the target detection performance of the MIMO system, so validation of these target models is necessary.

A MIMO array with co-located antennas is also explored to study the effects of using orthogonal waveforms (or waveforms with low cross-correlations) on imaging quality. The approximation of a MIMO array by a virtual array whose elements are located at the center of mass of each transmitter/receiver pair is verified through simulation. Then images of both a point target and distributed scatterer are compared to test whether or not waveforms with small cross-correlations can be separated sufficiently in the receivers. It is shown that the separation is sufficient in both cases.

The design and development of a flexible software-defined radar system (SDR) is outlined. Utilizing a powerful digital baseband transceiver with a 1 GSPS dual-channel ADC and DAC, the system is capable of generating, receiving, and coherently processing waveforms with up to 500 MHz of bandwidth. Two independent transmit channels and two independent receive channels are available, with a center frequency which can be tuned from 2-18 GHz. This system is used to measure the scattered fields from a complex target using spatially diverse transmitters and receivers. These results are used to evaluate the correlated scatterers model presented here. Furthermore, the SDR is used to measure a sphere using co-located transmitters and receivers to experimentally verify the imaging simulations.

For my parents ...

ACKNOWLEDGMENTS

First and foremost, I would like to thank my advisor, Professor Joel T. Johnson, for his guidance and support. I have learned a great deal from his methodical approach to solving any problem and his ability to always see the big picture. I would also like to thank Ninoslav Majurec for his invaluable contributions of time, knowledge, and experience to building the software-defined radar system described in this thesis.

In my time at the ElectroScience Laboratory, which began as an undergraduate student in 2002 with very little knowledge of anything, many people have influenced my life, my work, and my outlook on life. Therefore, I'd like to thank Kenneth Browne, Dr. Michael Carr, C. J. Moncrief, William Moulder, and Matt Valerio. My daily interactions with these individuals have made the ElectroScience Laboratory so much more than just a place to work.

Finally, I would like to thank George Reynolds of Northrop Grumman and Dr. W. Dennis Burnside of the ElectroScience Laboratory who, through mutual trust and cooperation, established a program to support my work as both a graduate student at the Ohio State University and an employee of Northrop Grumman.

VITA

June 7, 1982	Born - Girard, Ohio
December, 2004	B.S. Electrical and Computer Science, The Ohio State University, Columbus, OH
December, 2006	M.S. Electrical and Computer Science, The Ohio State University, Columbus, OH

PUBLICATIONS

Journal Publications

Frankford, M.T.; Johnson, J.T.; Ertin, E., "Including Spatial Correlations in the Statistical MIMO Radar Target Model," *Signal Processing Letters, IEEE,* vol.17, no.6, pp.575-578, June, 2010.

Frankford, M.T.; Johnson, J.T., "Compensation of Faraday Rotation in Multipolarization Scatterometry," *Transactions on Geoscience and Remote Sensing, IEEE,* vol.48, no.1, pp.358-364, January, 2010.

Güner, B.; Frankford, M.T.; Johnson, J.T., "A Study of the Shapiro-Wilk Test for the Detection of Pulsed Sinusoidal Radio Frequency Interference," *Transactions on Geoscience and Remote Sensing, IEEE,* vol.47, no.6, pp.1745-1751, June, 2009.

Conference Publications

Frankford, M.T.; Majurec, N.; Johnson, J.T., "Software-Defined Radar for MIMO and Adaptive Waveform Applications," *Radar Conference, 2010 IEEE,* pp.724-728, May 10-14, 2010.

Frankford, M.T.; Johnson, J.T., "Predictions of the Spatially Correlated Statistical MIMO Radar Target Model," in *Proc. URSI National Radio Science Meeting,* Boulder, CO, January, 2010.

Majurec, N.; Park, J.; Niamsuwan, N.; Frankford, M.T.; Johnson, J.T., "Airborne L-band RFI Observations in the SMAPVEX08 Campaign with the L-Band Interference Suppressing Radiometer," *International Geoscience and Remote Sensing Symposium, 2009 IEEE, IGARSS 2009,* vol.2, pp.158-161, July 12-17, 2009.

Güner, B.; Frankford, M.T.; Johnson, J.T., "On the Shapiro-Wilk Test for the Detection of Pulsed Sinusoidal Radio Frequency Interference," *International Geoscience and Remote Sensing Symposium, 2008 IEEE, IGARSS 2008,* vol.2, pp.157-160, July 7-11, 2008.

Frankford, M.T.; Johnson, J.T., "Compensation of Faraday Rotation in Multi-Polarization Scatterometry," *International Geoscience and Remote Sensing Symposium, 2008, IGARSS 2008,* vol.2, pp.169-172, July 7-11, 2008.

FIELDS OF STUDY

Major Field: Electrical Engineering

Studies in:

Applied Electromagnetics
Radar Design and Testing
Digital Signal Processing

TABLE OF CONTENTS

Page

LIST OF TABLES

Table **Page**

LIST OF FIGURES

Figure **Page**

CHAPTER 1

INTRODUCTION

1.1 Motivation and Challenges

A multiple-input multiple-output (MIMO) radar system consists of M transmitters and N receivers which may be co-located or distributed spatially. Typically, it is assumed that a method exists at each receiver for separating unambiguously the fields resulting from each transmitter, so that MN measurements are obtained. This can be accomplished through a variety of methods such as time-division multiple access (TDMA) as proposed in [1–3], Doppler-division multiple access (DDMA) as described in [4], or using waveforms with sufficiently low cross-correlation such as those proposed in [5, 6]. It is common in the literature to assume that the transmitted waveforms in a MIMO system are "orthogonal" such that they can be separated perfectly. It has been pointed out that this ideal MIMO waveform does not exist [7], but nevertheless orthogonality is a useful assumption which significantly simplifies modeling. The use of orthogonal waveforms across multiple transmit antennas has also been referred to elsewhere as a synthetic impulse and aperture radar (SIAR) [8–10].

If the geometry of transmit and receive antennas in a MIMO radar system provides angular diversity in observations of a target, it has been shown that for sufficiently

complex targets the MIMO radar system can provide benefits in target detection compared to a traditional phased array system, as the impact of variations in the target's radar cross section (RCS) with angle can be reduced. Several recent publications have examined the potential advantages of spatially diverse MIMO radars, including their use in target detection and parameter estimation applications [11–16]. These previous works have attempted to apply the Swerling-I model, originally derived to predict RCS fluctuations versus angle for monostatic radars, to the multistatic MIMO case with spatially diverse transmitters and receivers. However, while the Swerling-I model has been used to model fluctuations in the monostatic RCS for many years, it fails to predict the variation in target scattering versus the bistatic angle between transmitters and receivers. Therefore, a new model which captures these bistatic effects in addition to the monostatic effects is desirable. Validation of any of the MIMO target models is required as development and deployment of a spatially diverse MIMO radar is potentially expensive.

MIMO systems with co-located antennas are also being studied as a logical progression beyond phased arrays for imaging systems. If the transmitters and receivers are sufficiently close to one another, the MIMO array can be approximated by a "virtual array" of MN synthetic elements located at the centers of mass of each transmitter/receiver pair. If proper spacing is chosen for the sparse transmitters and receivers, the MIMO array with $M + N$ real elements can form a filled virtual array of length MN which satisfies the element spacing required to eliminate grating lobes. The ARTINO airborne radar for UAVs, for example, utilizes a co-located sparse MIMO array to form 3D images [1–3]. The sparse array is located on the wings of the UAV and points in the nadir direction. Resolutions in the three imaging dimensions

are generated by range compression in the nadir dimension, digital beamforming in the across-track dimension, and synthetic aperture processing in the along-track direction. For acceptable resolution in the across-track dimension, a standard phased array would require approximately 1120 elements. However, the ARTINO principle uses the sparse array with a far fewer number of transmitters and receivers to emulate the standard filled array using a MIMO virtual array. It has been proposed that the ARTINO system utilize time diversity to separate the returns for each MN pair of elements. However, if suitable orthogonal waveforms could be used instead of time diversity to separate the returns, the virtual array could be utilized in other imaging applications as well.

1.2 Contributions

In this dissertation, a new statistical MIMO target model is developed in an effort to model more accurately the bistatic scattering behavior of some classes of real-world targets. This model provides a closed form solution for the covariance matrix describing the scattered fields from a complex target for specific locations of the transmitter and receiver elements. The applicability of this new model to real-world complex targets is studied using measurements of a small UAV provided by a software-defined radar (SDR) system developed as part of this dissertation.

The SDR system consists of two independent transmit and receive channels with 500 MHz of instantaneous bandwidth whose center frequencies can be tuned from 2-18 GHz. An RF switch matrix is included to multiplex the two transmit and receive channels among four dual-polarized transmit antennas and four dual-polarized receive antennas. The system has the ability to transmit and receive independent

waveforms thereby forming a 2x2 MIMO system. If the switch matrix is utilized, a 4x4 MIMO system can be formed by cycling through different antenna combinations. The SDR provides experimentally measured data to support MIMO research with either spatially diverse or co-located antenna elements.

In addition to presenting and evaluating a new target model for MIMO with spatially diverse antennas, an analysis of using MIMO techniques with closely spaced antennas for imaging is presented. It is shown here that a sparse MIMO array can be approximated by a virtual array with MN elements, as images calculated using the near-field imaging algorithm for the virtual array elements or real MIMO array elements are similar. In addition, simulation results are presented to show that orthogonal waveforms, or waveforms with sufficiently low cross-correlations, can be used instead of time diversity to form the virtual array and accurately image a complex distributed target. Finally, images formed using the SDR system with independent waveforms are shown which confirm the simulated results.

1.3 Outline

Chapter 2 begins with an introduction to the statistical MIMO detection problem for spatially diverse transmitters and receivers. The original Swerling-I target model, which consists of many independent scattering centers, is first reviewed. This is followed by the introduction of a new model which includes correlation among the scatterers. The bistatic scattering behavior of these models is analyzed to show how changing the correlation distance allows for the tuning of the bistatic scattering pattern. Detection statistics are calculated for varying correlation lengths to study the effects of the bistatic scattering pattern on the target detection statistics. This is

followed by a Monte Carlo analysis to study to effects of antenna positioning on the detection statistics as well.

Details of the SDR system are outlined in Chapter 3. The system is examined starting first with the digital baseband transceiver followed by the multichannel, tunable RF up/downcoverter section. Finally, the software framework which controls the whole system is presented. Analysis of the framework includes all levels of processing beginning with the graphical user interface on the SDR PC, continuing with the software running on the DSPs, and ending with low-level FPGA functionality. During the construction of the SDR, the system was periodically tested to validate the system performance whenever possible. The results of this testing and validation are given in Chapter 4.

Chapter 5 outlines the method used to measure the scattered fields from a UAV in the anechoic chamber at The ElectroScience Laboratory - The Ohio State University. The measurement, conducted using the SDR with $M = 2$ transmitters and $N = 4$ receivers, provides calibrated bistatic scattering data which is used to evaluate the accuracy of the models presented in Chapter 2. The correlated scatterers model is fitted to the measured scattered fields from the UAV, and the results show that a statistical model consisting of uncorrelated scatterers best fits the measured data. Furthermore, the detection performance of the spatially diverse MIMO system is verified by comparing the detection statistics predicted by the models to those calculated from the measured data.

Chapter 6 starts by first comparing the images from a 2x2 sparse MIMO array, formed using time division to separate the waveforms, to those images obtained using 4 synthetic elements placed in the virtual array locations. The results show

that the approximation of a MIMO array by a virtual array is valid. Then the images formed with the MIMO array using time division or orthogonal waveforms to separate the returns at the receivers are compared to study the effects of non-zero cross-correlations between waveforms. Finally, the SDR system using 2x2 antenna elements and orthogonal waveforms is used to image a sphere in the anechoic chamber. This measurement effectively demonstrates generating four synthetic elements simultaneously with imaging results which agree well with the simulations.

CHAPTER 2

THE STATISTICAL MIMO TARGET MODEL

Fishler et. al. develop a statistical target scattering model to analyze the performance of a MIMO system which utilizes spatial diversity to improve target detection over a traditional phased array with the same number of elements [11]. Geometrical conditions on the locations of the transmit and receive antennas are first derived to determine what is considered sufficient angular diversity for all transmitter-receiver pairs for the given scattering model. If these spatial diversity conditions are met, it is shown that the optimal detector for operation in the presence of additive white Gaussian noise involves a incoherent summation of the received fields across all transmit/receive antenna pairs (i.e. the total received power). This is contrary to standard phased array radars which utilize a coherent summation of fields across the elements (beamforming). The performance of the MIMO detector is then derived assuming the spatial diversity conditions are satisfied, and it is shown that the performance of the spatially diverse MIMO radar system is superior to a standard phased array system if the signal-to-noise ratio exceeds some threshold.

The statistical target scattering model used in [11] describes the target as a finite rectangular area within which an infinite number of scatterers are contained. Each of these scatterers has a scattering amplitude that is a zero-mean complex Gaussian

random variable, and the scattering amplitudes are uncorrelated spatially; this is a "spatial white noise" model of the target. A modification of this model to include a finite number of spatially uncorrelated scatterers has also been presented [17], with a similar model in [18]. As will be shown, an important property of this model is that the bistatic scattering pattern is constant versus the bistatic angle between a given transmitter and receiver. This is often unrealistic in practice, as the tendency of real complex targets to scatter more in the forward direction has been demonstrated through both numerical simulation [19] and experimental measurement [20].

To more accurately model the bistatic scattering behavior of real targets, the scattering model of [11] is extended here to include spatial correlations among the random scatters that make up the rectangular target. This new target model utilizes an azimuthally symmetric Gaussian correlation function. The derivation of this model is described in Section 2.1 (originally presented in [21]). Under this assertion, only a single new target parameter, the correlation distance, is introduced. Increasing the correlation distance, or the amount of correlation between scatterers in the target, has the effect of altering the bistatic scattering properties of the target such that forward scattering is emphasized as is demonstrated in Section 2.2. The performance of the MIMO detector is studied for this new target in Section 2.3 for a fixed antenna geometry. In addition, the MIMO detector is compared to the optimal quadratic detector which utilizes *a priori* knowledge of the target's correlation distance. Finally, the effects of the antenna locations on the performance of the MIMO system are studied using a Monte Carlo simulation (results originally presented in [22]).

2.1 Correlated Scattering Model

Following [11], a two-dimensional geometry that includes all transmit and receive antennas and the target is utilized, as illustrated in Fig. 2.1. The target considered is not range resolved, and a single amplitude and phase characterizes the measurement for each transmit/receive pair. It is also assumed that the range from each transmitter and receiver to the target is similar, so that the range dependence of the received power (as well as the transmitter power) can be neglected here and incorporated later as part of the system signal-to-noise ratio in Section 2.3. The rectangular target is of dimensions $\Delta X \times \Delta Y$, and is composed of an infinite number of random scatterers whose complex scattering amplitudes are given by $\Sigma(\gamma, \beta)$ where (γ, β) are the local coordinates relative to the center of the target (x_0, y_0). The vector $\vec{r}_q$ in Fig. 2.1 indicates the direction and distance from the q^{th} transmitter to the center of the target, while the vector $\vec{r}_p$ indicates the direction and distance from the center of the target to the p^{th} receiver. The vectors $\vec{k}_q$ and $\vec{k}_p$ are defined identically, except that their amplitude is the electromagnetic wavenumber ($\frac{2\pi}{\lambda}$, where λ is the electromagnetic wavelength).

Using this model, the scattered field measured by the p^{th} receiver that results from the q^{th} transmitter (labeled α_{pq}) is proportional to a sum over all the individual scatterers of the target including appropriate phase delays:

$$\alpha_{pq} = \int_{-\frac{\Delta X}{2}}^{\frac{\Delta X}{2}} \int_{-\frac{\Delta Y}{2}}^{\frac{\Delta Y}{2}} \Sigma(\gamma, \beta)\, e^{-j\vec{k}_q \cdot (\vec{r}_q + \vec{r})} e^{-j\vec{k}_p \cdot (\vec{r}_p - \vec{r})} d\gamma d\beta \tag{2.1}$$

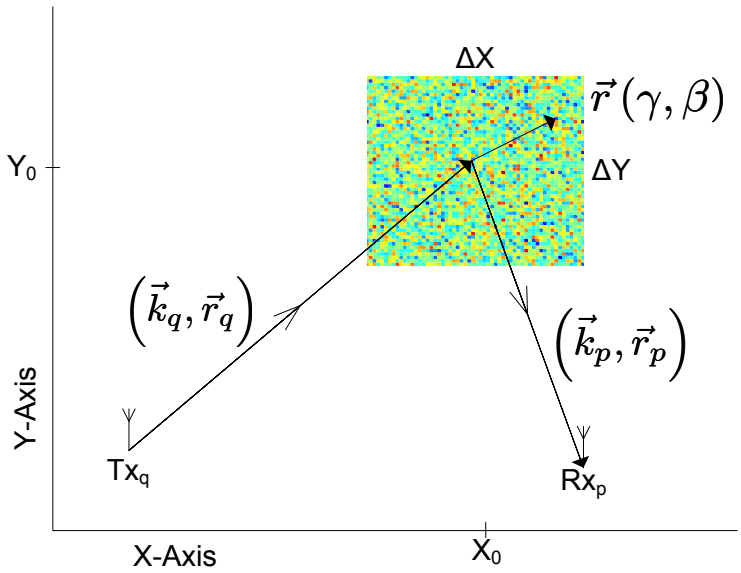

Figure 2.1: Bistatic scattering from a rectangular target of size ΔX by ΔY. The antennas are assumed to be in the far field of the target.

in which only $\vec{r}$ and Σ are functions of γ and β. (2.1) can be further simplified to

$$\alpha_{pq} = e^{-j\vec{k}_q\cdot\vec{r}_q} e^{-j\vec{k}_p\cdot\vec{r}_p} \int_{-\frac{\Delta x}{2}}^{\frac{\Delta x}{2}} \int_{-\frac{\Delta y}{2}}^{\frac{\Delta y}{2}} \Sigma(\gamma,\beta)\, e^{-j\vec{p}_{qp}\cdot\vec{r}} d\gamma d\beta \tag{2.2}$$

where $\vec{p}_{qp} = \vec{k}_q - \vec{k}_p$. The measurements of the MIMO system consist of MN α_{pq} values, which are grouped into the vector $\bar{\alpha}$.

If $\Sigma(\gamma,\beta)$ are described as zero-mean complex Gaussian random variables, it is apparent from (2.2) that each α_{pq} is also a zero-mean complex Gaussian random variable. The vector $\bar{\alpha}$ is then a zero-mean complex Gaussian vector ($\sim \mathcal{CN}(0, \boldsymbol{A})$) whose complete specification requires knowledge only of the covariance matrix $\boldsymbol{A} =$

$E\left\{\bar{\alpha}\bar{\alpha}^H\right\}$. Elements of this covariance matrix can be derived from (2.2).

$$E\left\{\alpha_{pq}\alpha_{st}^*\right\} = e^{j\left(\vec{k}_p\cdot\vec{r}_p+\vec{k}_q\cdot\vec{r}_q-\vec{k}_s\cdot\vec{r}_s-\vec{k}_t\cdot\vec{r}_t\right)} \cdot \int_{-\frac{\Delta X}{2}}^{\frac{\Delta X}{2}}\int_{-\frac{\Delta Y}{2}}^{\frac{\Delta Y}{2}}\int_{-\frac{\Delta X}{2}}^{\frac{\Delta X}{2}}\int_{-\frac{\Delta Y}{2}}^{\frac{\Delta Y}{2}} E\left\{\Sigma\left(\gamma,\beta\right)\ \Sigma^*\left(\gamma',\beta'\right)\right\} e^{j\vec{p}_{qp}\cdot\vec{r}(\gamma,\beta)}e^{-j\vec{p}_{ts}\cdot\vec{r}'(\gamma',\beta')}d\gamma d\beta d\gamma' d\beta' \tag{2.3}$$

Here, $\vec{p}_{qp} = \vec{k}_q - \vec{k}_p = p_x^{qp}\hat{x} + p_y^{qp}\hat{y}$ and $\vec{p}_{ts} = \vec{k}_t - \vec{k}_s = p_x^{ts}\hat{x} + p_y^{ts}\hat{y}$. Computation of the covariance matrix elements requires that the spatial covariance of the target point scatterers $E\left\{\Sigma\left(\gamma,\beta\right)\ \Sigma^*\left(\gamma',\beta'\right)\right\}$ be specified.

2.1.1 Uncorrelated Target Model

Reference [11] uses a spatially uncorrelated target model:

$$E\left\{\Sigma\left(\gamma,\beta\right)\Sigma^*\left(\gamma',\beta'\right)\right\} = \frac{1}{\Delta X\Delta Y}\delta(\gamma-\gamma')\delta(\beta-\beta') \tag{2.4}$$

where the factor of one over the target area ensures that the total target "energy" is independent of its size; this factor could also be omitted and absorbed into the final system signal-to-noise ratio in Section 2.3, but is included here for consistency with [11]. The Dirac delta functions of (2.4) greatly simplify the evaluation of the covariance matrix entries, and it can be shown that the diagonal entries of $\boldsymbol{A}$ ($E\{|\alpha_{pq}|^2\}$) are identical and equal to unity. This implies that the expected value of the received power for an uncorrelated target is identical for all bistatic transmitter and receiver geometries.

Off-diagonal entries of the covariance matrix are not computed in [11], but conditions for separations of transmit and receive antennas are derived to make the off-diagonal entries small. Since these terms describe the covariances between fields

measured in one transmit-receive pair and another, small off-diagonal terms indicate that near independent (i.e. angularly diverse) observations of the target are achieved.

2.1.2 Correlated Target Model

Correlation among the random scatterers is introduced by modifying (2.4) to

$$E\left\{\Sigma\left(\gamma,\beta\right)\ \Sigma^{*}\left(\gamma',\beta'\right)\right\}=\frac{1}{\Delta x\Delta y}\frac{1}{2\pi C_{d}^{2}}\exp\left(\frac{-\left(\left(\gamma-\gamma'\right)^{2}+\left(\beta-\beta'\right)^{2}\right)}{2C_{d}^{2}}\right) \tag{2.5}$$

where an azimuthally symmetric Gaussian correlation function has been chosen for mathematical convenience. This form allows for the introduction of spatial correlation while still yielding a closed-form solution. The parameter C_d is a correlation length: as C_d approaches zero, the point scatterers in the target become fully uncorrelated, and (2.4) is recovered. As C_d is increased, the point scatterer amplitudes are correlated over larger distances. Sample realizations of targets with varying correlation lengths are shown later in Section 2.4.1.

The normalization used in (2.5) again could be omitted, but is included to retain some analogy with the uncorrelated case. However, the form utilized does not guarantee that the integration of the variance of Σ over the target area yields unity, unless C_d is significantly less than the target dimensions. A correction could be introduced to account for this fact, but is unnecessary as will be discussed in Section 2.3.

The entries in the covariance matrix $\boldsymbol{A}$ can be calculated from (2.3) and (2.5), resulting in (2.6)

$$\begin{aligned}E\left\{\alpha_{pq}\alpha_{st}^{*}\right\}=&\frac{e^{-j\left(\vec{k}_{p}\cdot\vec{r}_{p}+\vec{k}_{q}\cdot\vec{r}_{q}-\vec{k}_{s}\cdot\vec{r}_{s}-\vec{k}_{t}\cdot\vec{r}_{t}\right)}}{2\pi C_{d}^{2}\left(\Delta X\Delta Y\right)}\\&\cdot\int_{-\frac{\Delta X}{2}}^{\frac{\Delta X}{2}}\int_{-\frac{\Delta X}{2}}^{\frac{\Delta X}{2}}e^{\left(\frac{-\left(\gamma-\gamma'\right)^{2}}{2C_{d}^{2}}\right)}e^{-j\left(p_{x}^{qp}\gamma-p_{x}^{ts}\gamma'\right)}d\gamma d\gamma'\int_{-\frac{\Delta Y}{2}}^{\frac{\Delta Y}{2}}\int_{-\frac{\Delta Y}{2}}^{\frac{\Delta Y}{2}}e^{\left(\frac{-\left(\beta-\beta'\right)^{2}}{2C_{d}^{2}}\right)}e^{-j\left(p_{y}^{qp}\beta-p_{y}^{ts}\beta'\right)}d\beta d\beta'\end{aligned} \tag{2.6}$$

where $\vec{p}_{qp} = \vec{k}_q - \vec{k}_p = p_x^{qp}\hat{x} + p_y^{qp}\hat{y}$ and $\vec{p}_{ts} = \vec{k}_t - \vec{k}_s = p_x^{ts}\hat{x} + p_y^{ts}\hat{y}$. The two double integrals can each be transformed into a product of two single integrals by a rotation of coordinates, namely $(\gamma_d = \gamma - \gamma', \gamma_s = \gamma + \gamma')$ and $(\beta_d = \beta - \beta', \beta_s = \beta + \beta')$, where $d\gamma d\gamma' = \frac{d\gamma_d d\gamma_s}{2}$ and $d\beta d\beta' = \frac{d\beta_d d\beta_s}{2}$. Analytical solutions can then be found both for the diagonal ($p = s$, $q = t$) and off-diagonal entries of the covariance matrix through use of an integral table [23]. Both cases have the general form

$$E\left\{\alpha_{pq}\alpha_{st}^*\right\} = \frac{e^{-j\left(\vec{k}_p\cdot\vec{r}_p + \vec{k}_q\cdot\vec{r}_q - \vec{k}_s\cdot\vec{r}_s - \vec{k}_t\cdot\vec{r}_t\right)}}{2\pi\left(\Delta X \Delta Y\right)} F_x F_y \tag{2.7}$$

where F_x and F_y are functions of C_d and the geometry of the system. For diagonal entries, F_ν (where $\nu = x$ or y, and $\Delta\nu = \Delta X$ or ΔY respectively) is

$$\begin{aligned} F_{\nu,\text{diag}} = & 2C_d \text{Re}\left\{\sqrt{\frac{\pi}{2}}\left(\frac{\Delta\nu}{C_d} + jp_\nu^{qp}C_d\right) T\left(jp_\nu^{qp}C_d, \frac{\Delta\nu}{C_d}\right)\right. \\ & \left. + \exp\left(\frac{-\Delta\nu^2}{2C_d^2}\right)\cos(p_\nu^{qp}\Delta\nu) - 1\right\} \end{aligned} \tag{2.8}$$

and for off-diagonal entries,

$$\begin{aligned} F_{\nu,\text{off-diag}} = & \left(\frac{\sqrt{2\pi}}{p_\nu^{qp} - p_\nu^{ts}}\right) \text{Im}\left\{e^{\left(\frac{j(p_\nu^{qp} - p_\nu^{ts})\Delta\nu}{2}\right)}\right. \\ & \left. \cdot \left[T\left(-jp_\nu^{ts}C_d, \frac{\Delta\nu}{C_d}\right) + T\left(jp_\nu^{qp}C_d, \frac{\Delta\nu}{C_d}\right)\right]\right\} \end{aligned} \tag{2.9}$$

where

$$T(A, B) = e^{\frac{A^2}{2}}\left[\Phi\left(\frac{A+B}{\sqrt{2}}\right) - \Phi\left(\frac{A}{\sqrt{2}}\right)\right] \tag{2.10}$$

with the error function denoted by Φ evaluated for a complex argument [23]. The covariance matrix element amplitudes are now a function of the angular geometry (as included in p_ν^{qp} for example), the target sizes (ΔX, ΔY), and the correlation length C_d.

2.2 Scattering Behavior of a Correlated Target

In the case of the uncorrelated target, it was shown by [11] that the diagonal terms of $\boldsymbol{A}$ were unity, while the off-diagonal terms were negligibly small for spatially diverse antennas. This implies that each pair of antennas receives on average an equal amount of scattered power from the target ($E\left\{|\alpha_{pq}|^2\right\}$) and that the received fields are uncorrelated ($E\left\{\alpha_{pq}\alpha_{st}^*\right\} \approx 0$). However, if target spatial correlations are introduced, these conclusions are no longer true. The complexity of (2.7)-(2.10) make physical interpretation difficult. Example results are shown in this section to illustrate the scattering behaviors captured by the correlated target model.

2.2.1 Diagonal Covariance Matrix Entries

In the limit that C_d approaches zero, (2.7) becomes unity for all diagonal terms ($p = s$ and $q = t$), independent of the locations of the transmitters and receivers. For non-zero C_d, however, (2.8) depends on the locations of the transmitters and receivers relative to one another, and therefore the average bistatic radar cross section is no longer a constant function of angle.

Fig. 2.2 shows $E\left\{|\alpha_{pq}|^2\right\}$ as a function of the bistatic scattering angle by fixing transmitter p at 0° and moving receiver q in a circle about an axis-aligned rectangular target of size $3\lambda \times 3\lambda$. The bistatic patterns illustrated are normalized so that the maximum value of the pattern is unity. Fig. 2.2(a) considers $C_d = 0\lambda$, where the magnitude of $E\left\{|\alpha_{pq}|^2\right\}$ is unity for all scattering angles. For $C_d = .25\lambda$ in Fig. 2.2(b), the bistatic scattering pattern becomes stronger in the forward scattering direction. A direct consequence of this is that the diagonal entries in the covariance matrix for a given MIMO geometry are no longer identical as they would be in the $C_d = 0\lambda$

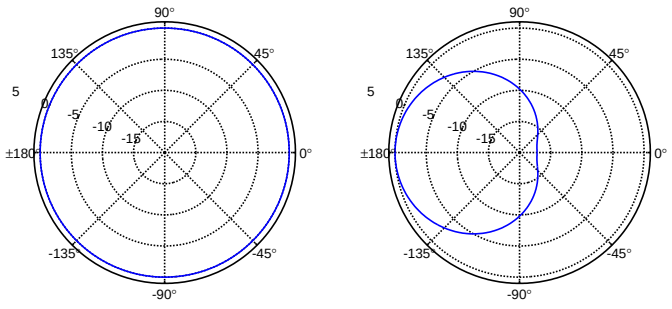

(a) $C_d = 0\lambda$ (b) $C_d = 0.25\lambda$

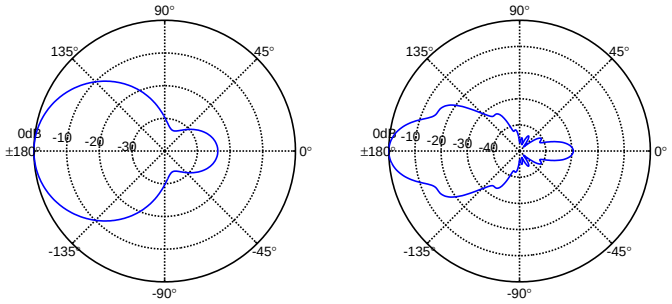

(c) $C_d = 0.5\lambda$ (d) $C_d = 2\lambda$

Figure 2.2: Normalized bistatic scattering patterns in dB for varying correlation lengths. The incident field on the target at 0° moving in the $-\hat{x}$ direction.

case. Increasing the correlation of the target further increases the forward scattering strength as is evident in Figs. 2.2(c) and 2.2(d). The lobing in the scattering pattern observed in Fig. 2.2(d) is associated with the square target geometry used, and also varies with target size and orientation. Since some classes of realistic targets often produce larger scattering amplitudes in the forward scattering direction than in other directions, the incorporation of correlations into the MIMO target model may expand the range of applicability for such stochastic target descriptions.

Note that the forward scattered (i.e. $\vec{p}_{qp} = \vec{0}$) value for $E\left\{|\alpha_{pq}|^2\right\}$ in (2.7) actually decreases as C_d increases, due to the normalization used in (2.5). Again issues of normalization will be addressed in Section 2.3.

2.2.2 Off-diagonal Covariance Matrix Entries

For the uncorrelated target model, reference [11] derived conditions relating the transmitter and receiver geometries and the target size to obtain small off-diagonal covariance matrix entries. However, if $C_d \neq 0$, received signals for each bistatic scattering pair may have appreciable correlations even if the derived spatially diversity conditions are satisfied for an equally sized uncorrelated target. To illustrate this effect, the correlation between two backscattering geometries is analyzed. A target is placed at the origin and a co-located transmitter and receiver observe the target at 0° incidence. A second co-located transmitter and receiver pair is moved in a circle about the target, and $E\left\{\alpha_{pq}\alpha_{st}^*\right\}$ is calculated as a function of the angle between the monostatic pairs.

Fig. 2.3 shows the resulting magnitude of $E\left\{\alpha_{pq}\alpha_{st}^*\right\}$ versus the angle between the two monostatic radars, and is normalized such that the maximum over the angular pattern is unity. When $C_d = 0$, the covariance is maximum when the two monostatic pairs are close to one another in angle, and decreases as the angular separation increases. Equation (16) in [11] applied to this geometry shows that an angular separation of approximately 20° (marked by dashed lines in Fig. 2.3(a)) is required to achieve approximately independent observations. Increasing C_d tends to increase the magnitude of the covariance in all directions, particularly the covariance between the monostatic returns when the two radars are 180° from each other. Fig. 2.3(d) uses

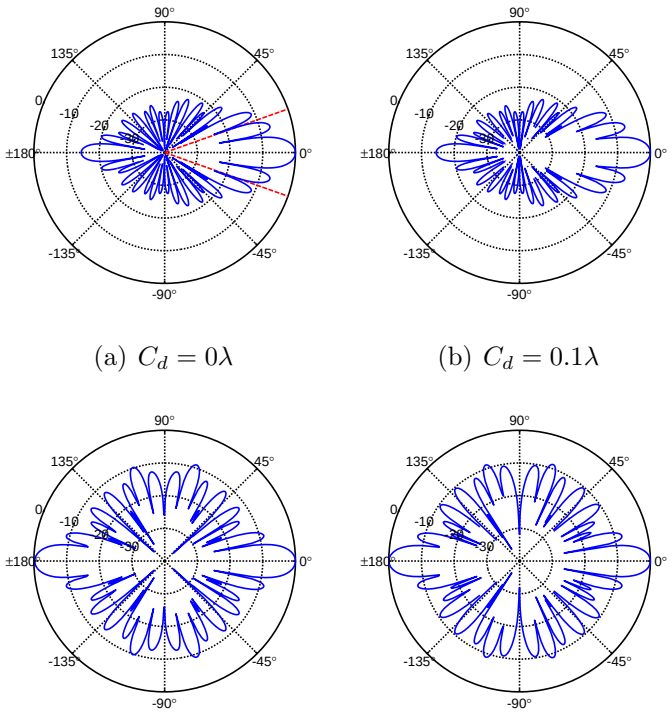

(a) $C_d = 0\lambda$ (b) $C_d = 0.1\lambda$

(c) $C_d = 0.5\lambda$ (d) $C_d = 2\lambda$

Figure 2.3: Normalized covariance in dB of two monostatic transmitter and receiver pairs as a function of the difference in observation angle.

$C_d = 2\lambda$, and shows for this case that backscattered fields are strongly correlated over a range of angles. It should be noted that these figures show the magnitude of the normalized covariance in dB, but the covariance for the case where the two radars are separated by 180° is actually a negative value. The lobing nature of these figures is again associated with the rectangular nature of the target and would vary with target size and orientation. An averaging of the covariance matrix entries over target azimuthal rotations could be performed to reduce these effects and is explored later in Section 2.4.1.

2.3 Detector Formulation

MIMO radar measurements are corrupted by thermal noise in the radar receivers; noise corrupted measurements are represented in what follows by the vector $\bar{x}$. Detection performance in the presence or absence of target correlations is investigated for a fixed system signal-to-noise ratio. Following [11], the latter is defined as the ratio of the average total received power (summed over all transmit-receive antenna pairs, and neglecting thermal noise) to the average thermal noise power summed over N receivers. This results in

$$\text{SNR} = \frac{\mathcal{E}}{\sigma_n^2}\left(\frac{\text{trace}\boldsymbol{A}}{N\ M}\right) \tag{2.11}$$

where $\mathcal{E}$ is the total transmitted power, assumed to be divided equally among the M transmit antennas, and σ_n^2 is the average thermal noise power in a single receiver. For an uncorrelated target, the term in the parenthesis above is unity. This definition of the SNR is also equal to M times the ratio of the average total received power in the presence of the target (and neglecting thermal noise) to that in its absence.

To reduce the number of variables and to take into account the total transmitted power $\mathcal{E}$, a vector $\bar{\beta}$ can be defined that is proportional to the received signal vector $\bar{\alpha}$:

$$\bar{\beta} = \sqrt{\frac{\mathcal{E}}{M}}\left(\frac{\bar{\alpha}}{\sigma_n}\right) \tag{2.12}$$

For the target model considered, $\bar{x}$ then has the form

$$\bar{x} = \begin{cases} \bar{n} & \mathcal{H}_0 \\ \bar{\beta} + \bar{n} & \mathcal{H}_1 \end{cases} \tag{2.13}$$

under $\mathcal{H}_0$ and $\mathcal{H}_1$, where a division of $\bar{x}$ by σ_n has been included. Here $\bar{n} \sim \mathcal{CN}\left(0, \boldsymbol{I}_{MN}\right)$ is an additive complex Gaussian vector that models receiver thermal

noise contributions. Note that both $\bar{\beta}$ and $\bar{n}$ have been scaled by the standard deviation of the noise σ_n. Also $\bar{\beta} \sim \mathcal{CN}(0, \boldsymbol{B})$ can be determined from $\bar{\alpha}$, (2.11), and (2.12) to have covariance matrix

$$\boldsymbol{B} = N \text{ SNR} \frac{\boldsymbol{A}}{\text{trace}\boldsymbol{A}} \tag{2.14}$$

The detection problem reduces to testing the hypothesis of whether a given complex vector observation is drawn from a complex Gaussian distribution having a first ($\boldsymbol{I}_{MN}$) or a second ($\boldsymbol{M} = \boldsymbol{B} + \boldsymbol{I}_{MN}$) covariance matrix.

For problems with no unknown parameters, the likelihood ratio test (LRT) provides the optimal detector in the Neyman-Pearson sense for detecting signals in noise. The LRT for this case reduces to [24]

$$\bar{x}^H \boldsymbol{Q} \bar{x} \underset{<_{\mathcal{H}_0}}{>^{\mathcal{H}_1}} \delta \tag{2.15}$$

where

$$\boldsymbol{Q} = \boldsymbol{I}_{MN} - \boldsymbol{M}^{-1} \tag{2.16}$$

Implementing this detector requires a-priori knowledge of $\boldsymbol{M}$, which implies knowledge of the target size, orientation, correlation distance, and SNR. Because such information is unlikely to be available, implementation of (2.15) is not expected in practice. However, the performance of this LRT detector can serve as a standard by which to assess the performance of other detectors.

In the case of the uncorrelated target model and for sufficient spatial separations to achieve "MIMO" operation, the LRT detector reduces to the "energy detector" of [11]:

$$\|\bar{x}\|^2 \underset{<_{\mathcal{H}_0}}{>^{\mathcal{H}_1}} \delta \tag{2.17}$$

The performance of this energy detector for the correlated target model is formulated in what follows.

2.3.1 Performance of the Energy Detector

Under the null hypothesis, the test statistic $\|\bar{x}\|^2$ is a scaled chi-square random variable

$$\|\bar{x}\|^2 \sim \frac{1}{2}\chi^2_{(2MN)} \tag{2.18}$$

and the threshold δ can be set as a function of the probability of false alarm [11]

$$\delta = \frac{1}{2}F^{-1}_{\chi^2_{2MN}}(1 - P_{FA}) \tag{2.19}$$

where $F^{-1}_{\chi^2_{2MN}}$ is the inverse cumulative distribution function (CDF) of a chi-square random variable with $2MN$ degrees of freedom.

In order to calculate the probability of detection (P_D), the CDF of $\|\bar{x}\|^2$ must be found under the alternate hypothesis $\mathcal{H}_1$. Since the elements of $\bar{x}$ are correlated, it is difficult to write the CDF of $\|\bar{x}\|^2$ directly. However, reference [17] provides a procedure for computing P_D by diagonalizing the covariance matrix of $\bar{x}$ to create a second random vector whose entries are uncorrelated.

The covariance matrix $\boldsymbol{M}$ can be computed for a specified MIMO geometry and target properties using the analytic expressions for $E\left\{\bar{\alpha}\bar{\alpha}^H\right\}$ derived in Section 2.1.2. Following [17], a singular value decomposition (SVD) of $\boldsymbol{M}$ can be written as $\boldsymbol{M} = \boldsymbol{U}\boldsymbol{\Lambda}\boldsymbol{U}^H$ since the covariance matrix is Hermitian. $\boldsymbol{\Lambda}$ is a diagonal matrix whose k^{th} entry along the diagonal is the k^{th} eigenvalue (λ_k) of $\boldsymbol{M}$, and $\boldsymbol{U}$ is a unitary matrix whose k^{th} column is the eigenvector corresponding to the k^{th} eigenvalue of

$\boldsymbol{M}$. Defining a vector $\bar{\kappa} = \boldsymbol{U}^H \bar{x}$, we can calculate it's covariance matrix as:

$$\begin{aligned} E\left\{\bar{\kappa}\bar{\kappa}^H\right\} &= E\left\{\boldsymbol{U}^H \bar{x}\bar{x}^H \boldsymbol{U}\right\} \\ &= \boldsymbol{U}^H E\left\{\bar{x}\bar{x}^H\right\} \boldsymbol{U} = \boldsymbol{U}^H \boldsymbol{M}\boldsymbol{U} \end{aligned} \tag{2.20}$$

Therefore, $\bar{\kappa}$ has the distribution:

$$\bar{\kappa} \sim \mathcal{CN}\left(0, \boldsymbol{U}^H \boldsymbol{M}\boldsymbol{U}\right) = \mathcal{CN}\left(0, \boldsymbol{\Lambda}\right) \tag{2.21}$$

Since the covariance matrix of $\bar{\kappa}$ is diagonal, the entries of $\bar{\kappa}$ are uncorrelated. In addition, since $\boldsymbol{U}$ is unitary, $\|\bar{\kappa}\|^2 = \|\bar{x}\|^2$. Therefore, the task of calculating the CDF of a sum of correlated random variables becomes calculating the CDF of a sum of uncorrelated random variables, where each random variable has a different variance λ_k.

Reference [17] writes the characteristic function of $\|\bar{x}\|^2$ as the product of the characteristic functions of scaled chi-square random variables. A partial fraction expansion is performed to transform the product of characteristic functions into a sum of characteristic functions, and an inverse Laplace transform is taken to find the probability density function (PDF). The upper incomplete Gamma function is then used to convert the PDF to the CDF. These steps are described in equations (9)-(12) in [17] and only the result is repeated here. The final form for P_D is

$$P_D = \sum_{m=1}^{N} \sum_{n=1}^{\mu_m} A_{m,n} \lambda_m^{\mu_m - n + 1} e^{\frac{-\delta}{\lambda_m}} \sum_{p=0}^{\mu_m - n} \frac{\left(\frac{\delta}{\lambda_m}\right)^p}{p!} \tag{2.22}$$

where $A_{m,n}$ are the partial fraction expansion coefficients defined by equation (10) in [17], λ_m is the m^{th} eigenvalue of the covariance matrix $\boldsymbol{M}$, μ_m is the algebraic multiplicity of λ_m, and δ is the decision threshold calculated in (2.19). The performance for the full LRT detector (equation (2.15)) can be formulated in a similar fashion and is not detailed here.

2.4 Results

The previous section determined the probability of detection for the energy detector for a specified arrangement of transmit and receive antennas, target correlation properties, and SNR. For comparison, the probability of detection for a phased array system is derived in reference [11], and the reader is directed to the reference for details. For the phased array case, the SNR is defined using the average value of the power in the total received field following beam-forming. Due to the normalization utilized, this implies that target correlations do not impact the results, and the detection performance of the phased array system is only dependent on the SNR at the receivers, not the amount of correlation present in the target. In the results that follow, the performance of the phased array and the original MIMO target model as derived by [11] will serve as standards for evaluating the effects of correlated scatterers on MIMO performance. The behavior of the energy detector will be studied for a fixed antenna geometry in Section 2.4.1. Then, the effects of the antenna geometry itself on detection performance will be studied through the utilization of a Monte Carlo simulation in Section 2.4.2.

2.4.1 Results for a Fixed MIMO Geometry

Fig. 2.4 illustrates a representative MIMO geometry with $M \times N = 2 \times 4$ for which the probability of detection and missed detection were calculated for targets with varying degrees of spatial correlation using the energy detector. This configuration satisfies the conditions derived in [11] for the covariance matrix to be approximately diagonal in the uncorrelated target case.

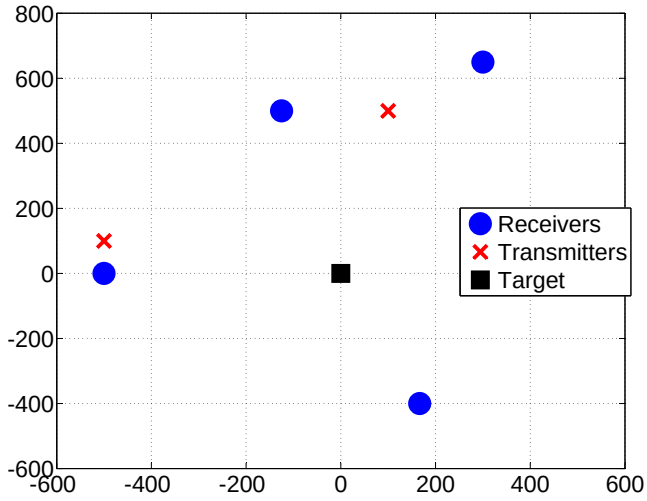

Figure 2.4: MIMO geometry with $M = 2$ transmitters and $N = 4$ receivers spaced around a target located at the origin. The units of the X and Y coordinates are in wavelengths λ.

The rectangular target has $\Delta X = \Delta Y = 3\lambda$; three sample realizations of the colored noise process corresponding to this target are provided in Fig. 2.5, using $C_d = 0\lambda$, 0.25λ, and 2λ, respectively. The corresponding covariance matrix $\boldsymbol{B}$ amplitudes in decibels are also shown (note $\boldsymbol{B}$ does not include any diagonal contributions from additive white noise.) The uncorrelated case in Figs. 2.5(a) and 2.5(b) has constant amplitudes along the diagonal with small (but non-zero) off-diagonal entries. As the correlation length is increased as depicted in Figs. 2.5(c) and 2.5(e) for $C_d = .25\lambda$ and 2λ respectively, the corresponding covariance matrices (Figs. 2.5(d) and 2.5(f)) are no longer uniform along the diagonal. In addition, the off-diagonal entries become appreciable.

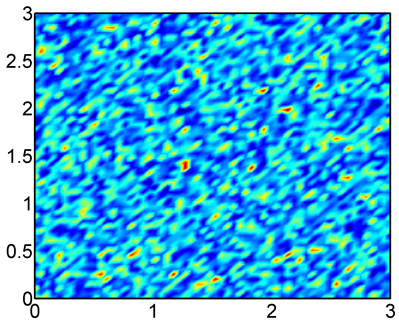

(a) Target for $C_d = 0\lambda$

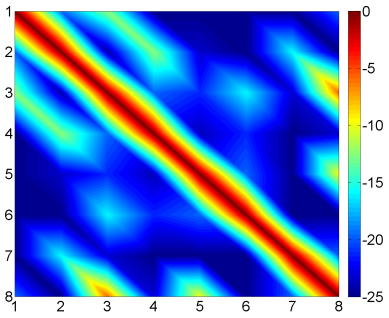

(b) Covariance matrix for $C_d = 0\lambda$ in dB

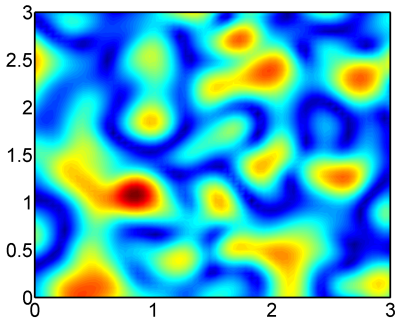

(c) Target for $C_d = 0.25\lambda$

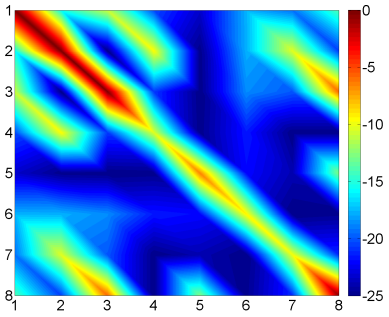

(d) Covariance matrix for $C_d = .25\lambda$ in dB

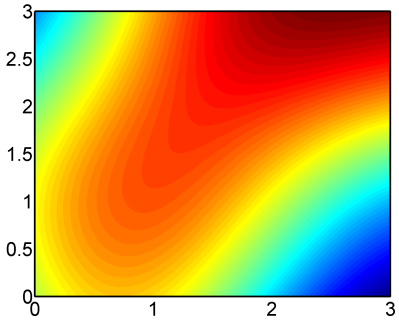

(e) Target for $C_d = 2\lambda$

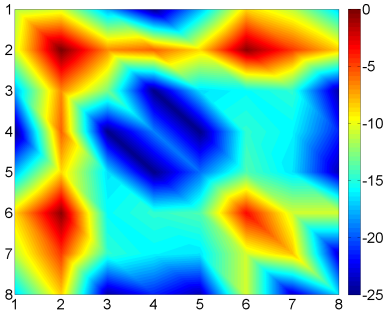

(f) Covariance matrix for $C_d = 2\lambda$ in dB

Figure 2.5: Realizations of a $3\lambda \times 3\lambda$ target for increasing correlation C_d along with the resulting covariance matrix $\boldsymbol{B}$. $\boldsymbol{B}$ is dependent on the MIMO geometry and C_d, and is shown here in dB.

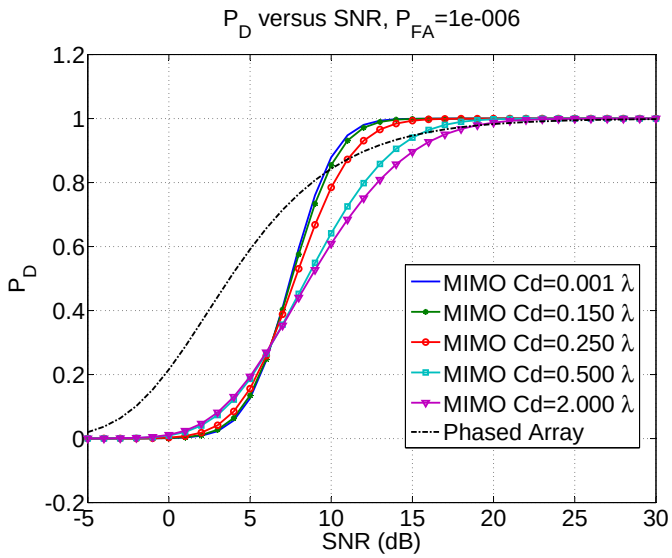

Figure 2.6: Probability of detection of the energy detector for $P_{FA} = 10^{-6}$.

The probability of detection (P_D) for the energy detector versus SNR calculated for varying target correlations using (2.22) is plotted in Fig. 2.6 for $P_{FA} = 10^{-6}$ on a linear scale. The corresponding probability of a missed detection, ($P_{MD} = 1 - P_D$), is shown on a log scale in Fig. 2.7.

The P_{MD} of the MIMO system for $C_d = 0.001$ agrees almost exactly with the uncorrelated scatterers case presented by Fishler *et al.* in Fig. 4 of [11]. This is expected since the correlation function of (2.5) simplifies to (2.4) when the correlation length C_d is small. For low SNRs, P_D is slightly larger for targets with more correlation. However, this trend reverses here for SNR greater than approximately 8 dB, and the performance of the MIMO system decreases for increasing target correlation lengths. The SNR required for the MIMO detector performance to exceed that of the phased array system is a parameter of interest. In this example, this SNR increases

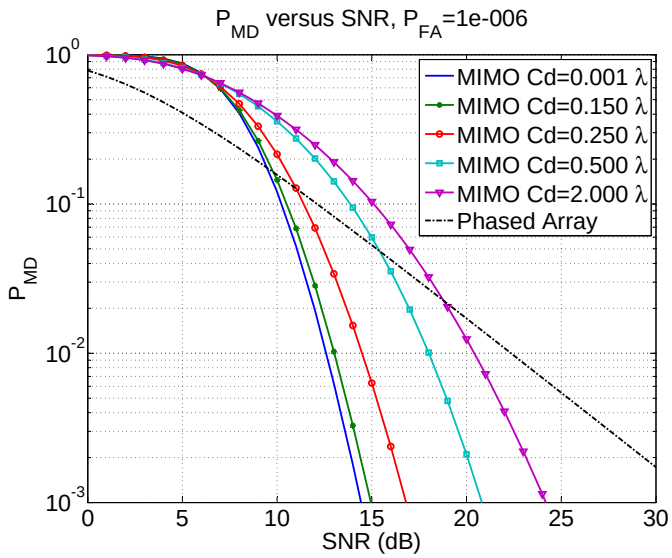

Figure 2.7: Probability of missed detection of the energy detector for $P_{FA} = 10^{-6}$.

by approximately 10 dB as the correlation length of the target is increased from zero to $C_d = 2\lambda$. These results suggest that the uncorrelated target model represents a best case scenario for evaluating the performance of a MIMO system using the energy detector.

Fig. 2.8 compares the P_{MD} performance of the energy and LRT quadratic detectors for $P_{FA} = 10^{-4}$. As expected, the two perform identically in the uncorrelated target case. However, the performance of the LRT detector is only slightly better than the energy detector derived for the uncorrelated target case even for targets consisting of correlated scatterers. This implies that decreased performance is observed primarily due to a reduction of information in the measurements rather than due to use of the energy detector. A reduction of information in the measurements can be interpreted as arising from the preferential distribution of power into the forward scattering region,

which, for a fixed signal-to-noise ratio, reduces the power available to observe the target at other aspect angles.

For the correlated target model, P_D is dependent on the geometry of the MIMO system, and the results shown apply only for the geometry of Fig. 2.4. For larger C_d in particular, the orientation of the target becomes significant since the bistatic scattering pattern is irregular. To address the degree of variability in these results, Fig. 2.9 plots minimum, maximum, and mean P_{MD} (energy detector) curves for $C_d = 2\lambda$ as the target orientation is rotated through 360° and the transmitter and receiver locations stay the same. These curves were generated by computing the P_{MD} for all target orientation angles in steps of 0.5° for a given SNR, and then taking the maximum, minimum, and mean for every SNR point. The P_{MD} with no rotation from Fig. 2.7 (labeled "representative") is also shown for comparison. As is evident from the figure, the orientation of the target has a significant impact on the performance of the system.

2.4.2 Geometry-Specific Results

Since the performance of the MIMO system is highly dependent on the specific locations of the transmitters and receivers, it is useful to study the average performance over many possible MIMO geometries. To this end, a Monte Carlo simulation is utilized where the locations of the transmitters and receivers are uniformly distributed inside some restricted space with respect to the target. Specifically, if the target is assumed to be located at the origin, the polar coordinates (r, θ) of the MIMO transmitters and receivers are uniformly distributed on the intervals $500\lambda \leq r \leq 501\lambda$ and $-\phi \leq \theta \leq \phi$. This restricted space will be referred to here as the T_x/R_x *Region*

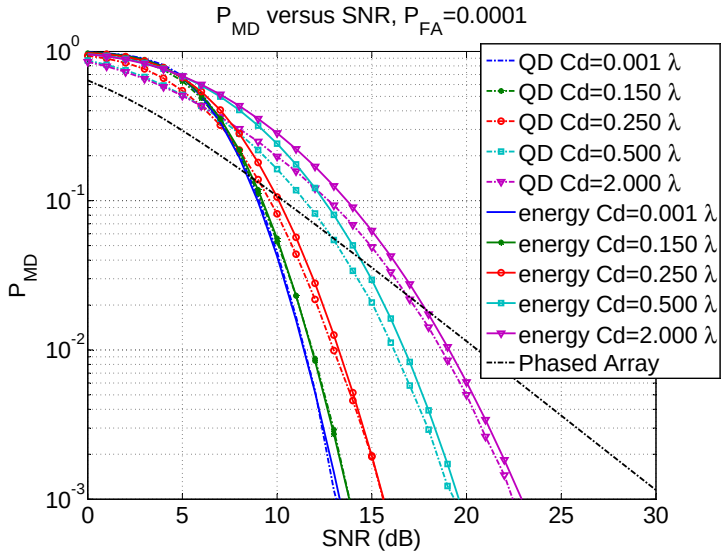

Figure 2.8: Probability of missed detection for both the LRT detector (QD) and the energy detector (energy) for $P_{FA} = 10^{-4}$.

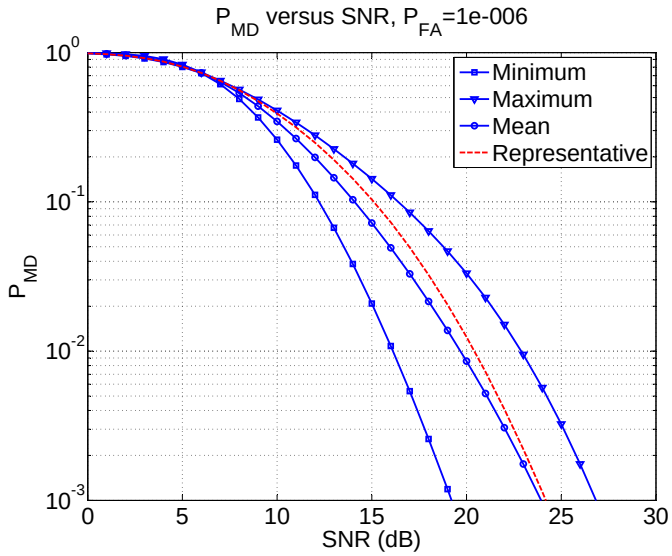

Figure 2.9: Maximum, minimum, and mean P_{MD} for the energy detector for $C_d = 2\lambda$ as the orientation of the target is rotated through 360°.

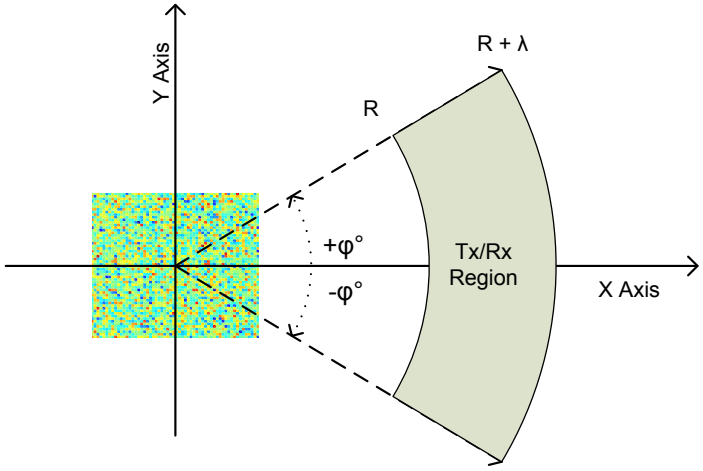

Figure 2.10: Definition of region to which random transmit and receive antenna locations are restricted.

and is illustrated in Fig. 2.10. Since the MIMO target model only accounts for phase effects in range, the radial size of the T_x/R_x *Region* can be limited to one wavelength as described without affecting the results. For the results shown in this section, 200 realizations of the MIMO geometry are generated.

The MIMO target studied here has the dimensions $3\lambda \times 3\lambda$, with the MIMO system consisting of two transmitters and four receivers ($M = 2$, $N = 4$) as before. Since the target is rectangular, the orientation of the target with respect to the MIMO system affects the probability of detection as was shown in the previous section. Therefore, the results in this section have been averaged over the target orientation angle (0.5° resolution) in addition to the varying MIMO geometries to remove this dependence.

Fig. 2.11 shows the probability of missed detection ($P_{MD} = 1 - P_D$) versus SNR with $P_{FA} = 10^{-6}$ for several values of the correlation length (C_d). For this figure,

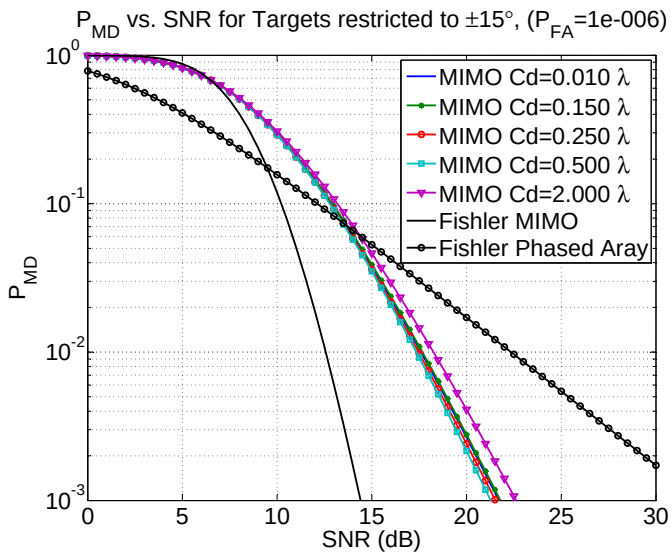

Figure 2.11: P_{MD} for a $3\lambda \times 3\lambda$ target and MIMO transmitters and receivers restricted to $\phi = \pm 15°$.

the locations of the transmitters and receivers are restricted to $-15° \leq \theta \leq +15°$. In addition, the P_{MD} for the phased array and the uncorrelated MIMO case are shown for reference. The correlation distance is seen to have little effect in this case, as each transmitter-receiver pair observes a similar aspect of the target. Since the transmitters and receivers are within the angular bounds determined by *Fishler et. al.* to be necessary for true angular diversity, the P_{MD} is worse than that predicted by *Fishler et. al.* for an uncorrelated target where the antennas are sufficiently angularly diverse.

However, as the angular diversity of the MIMO system is increased, the performance increases as well. Fig. 2.12 shows the P_{MD} when the transmitters and receivers are restricted to $-45° \leq \theta \leq +45°$, and Fig. 2.13 shows the P_{MD} when the transmitters and receivers are restricted to $-90° \leq \theta \leq +90°$. As expected, the P_{MD} for the

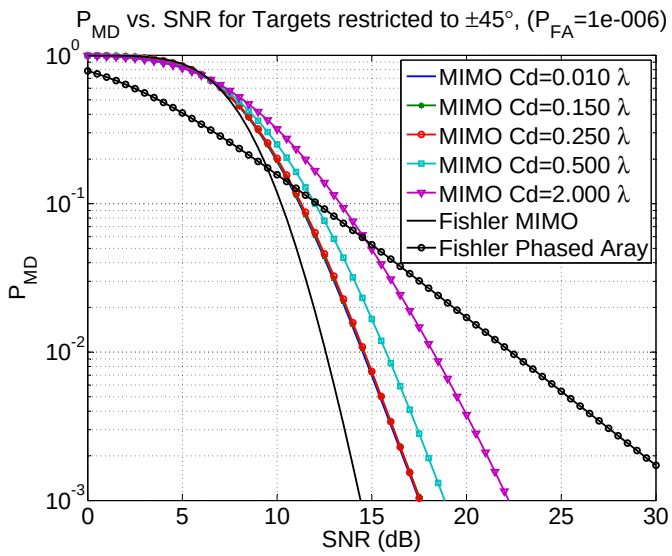

Figure 2.12: P_{MD} for a $3\lambda \times 3\lambda$ target and MIMO transmitters and receivers restricted to $\phi = \pm 45°$.

the shortest correlation distance ($C_d = 0.01\lambda$) begins to approach the uncorrelated MIMO result predicted by *Fishler et. al.*. However, for larger C_d values, the performance degrades. This occurs because the correlated target begins to focus scattered energy into the forward direction for larger values of C_d. Therefore, the detection statistic is dominated by transmit/receive pairs that are closer to forward scattering, while other pairs contribute less information about the target.

Fig. 2.14 shows the results for the case where the transmitters and receivers can be placed at any angle around the target. The performance of the smallest correlation in this case is very close to that predicted by *Fishler et. al.*, with the difference being attributed to the fact that, while the transmitters and receivers can be placed at any angle, every realization of the MIMO geometry is not *guaranteed* to be angularly diverse. Therefore, the realizations of the antenna locations that are not angularly

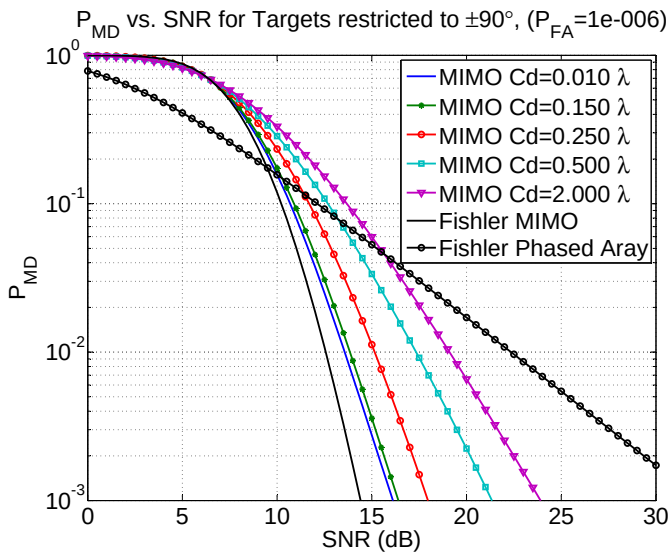

Figure 2.13: P_{MD} for a $3\lambda \times 3\lambda$ target and MIMO transmitters and receivers restricted to $\phi = \pm 90°$.

diverse slightly decrease the average performance of the system. As the correlation distance is increased, the performance of the MIMO system again decreases due to changes in the bistatic scattering behavior of the target. This is an important effect as it is evident that the SNR where the MIMO system begins to outperform the phased array increases considerably from the uncorrelated case to the most correlated case studied.

2.5 Summary

This chapter introduced the statistical target model for MIMO radar systems with angularly diverse antennas derived by *Fishler et. al.* in [11] which describes the scattered fields from a complex target consisting of uncorrelated scatterers . Analysis in this chapter showed that the model has a constant bistatic scattering pattern which

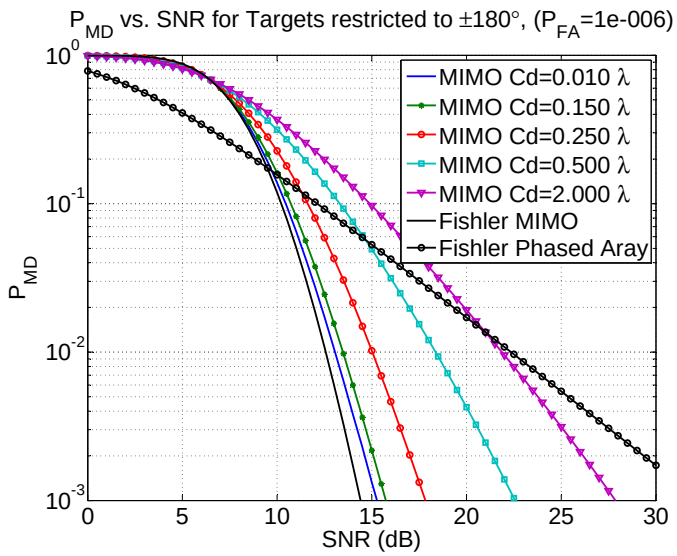

Figure 2.14: P_{MD} for a $3\lambda \times 3\lambda$ target and MIMO transmitters and receivers restricted to $\phi = \pm 180°$.

is unrealistic for some classes of targets. To rectify this, spatial correlation between the scatterers comprising the target was added to the model, and a new closed form solution for the covariance matrix of the received fields was derived. It was then shown that increasing the correlation between the scatterers increases the amount of forward scattering exhibited by the target. This implies that the average received power for a given pair of antennas is dependent on the bistatic angle between them.

For the uncorrelated scatterers target model, *Fishler et. al.* derived the optimal detector for angularly diverse transmitters and receivers in the presence of white noise as the incoherent summation of the received fields from all transmit/receive antenna pairs. The optimal detector for the correlated scatterers model, however, is the quadratic detector which requires *a priori* knowledge of the target size and correlation length. Since application of the quadratic detector is unlikely in practice,

the performance of the energy detector when applied to the correlated scatterers case was studied and was found to behave very similarly to the quadratic detector. Both detectors showed that increasing the amount of correlation in the target negatively impacts the performance of the MIMO system. Particularly, the SNR required for the MIMO system to outperform a phased array system in terms of the probability of detection is increased with increasing correlation. Finally, a Monte Carlo simulation was utilized to study the effects of antenna placement and target orientation on the performance of the detector, and as expected, increasing the angular diversity in antenna locations improves the performance of the MIMO radar system.

Building and deploying a MIMO radar system represents a potentially significant increase in cost and complexity when compared to a traditional phased array system. In addition, it is not directly clear how either Fishler's model or the extended model derived here can be applied to real world targets. Therefore, it is necessary to evaluate these target models with real-world measurements of complex targets. Chapters 3 and 4 outline the design, construction, and validation of a multi-channel software-defined radar system which will be used to experimentally evaluate the applicability of the models described here. Chapter 5 will discuss the final results of this evaluation.

CHAPTER 3

SOFTWARE-DEFINED RADAR DESIGN

A new radar platform has been developed to enable evaluation of the MIMO target models described in the previous chapter, as well as other advanced techniques such as the application of MIMO ideas to radar antenna arrays. This platform is called the software-defined radar (SDR) . The SDR is a very low power radar system with a nominal range of approximately 100 meters, based on a network of powerful digital signal processors and a very flexible RF front end. Details of the digital and RF hardware are discussed in Section 3.2. A comprehensive software framework to control the SDR in support of a range of experiments is outlined in Section 3.3.

3.1 Theory of Operation

At its core, the SDR is essentially a pulsed doppler radar which transmits a coherent pulse train to measure the range and doppler frequency shift created by a moving target [25]. The doppler frequency shift in Hertz (Hz) due to the motion of a target is given by

$$f_d = \frac{2 f_t v_r}{c} \tag{3.1}$$

where f_t is the transmitted frequency, v_r is the radial velocity of the target in meters-per-second, and c is the speed of light also in meters-per-second [26]. To measure

doppler without ambiguity, the pulse repetition frequency (PRF) of the radar must be equal to at least twice the maximum expected doppler shift. In normal pulsed doppler radars, a trade-off must be made between unambiguous range and unambiguous doppler, and often the radar is operated with a PRF that results in both ambiguous range and doppler. However, since the SDR is primarily a low power radar with a short range of interest, the PRF can be very high without introducing ambiguities in the measured range returns. In addition, most targets of interest for the SDR are slow moving, in which case a relatively low PRF is often desirable. The ability to operate with a high PRF without range ambiguities allows the SDR to transmit a number of pulses at a high PRF and coherently average the range returns into a single range return with an improved signal-to-noise ratio (SNR). This process is repeated at a fixed slower PRF for the purposes of measuring doppler. The resulting pulse train is outlined in Fig. 3.1. In the presence of white Gaussian noise, coherent

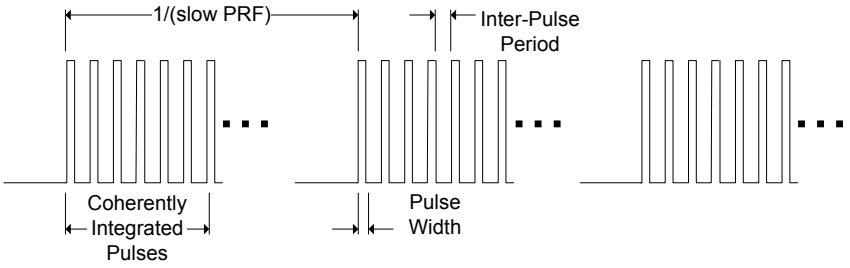

Figure 3.1: Coherent transmit pulse train utilizing both a fast and slow PRF for coherent integration of range returns and doppler detection of slower moving targets respectively.

integration improves the SNR by a factor equal to the number of pulses integrated, n_p [27]. However, in low SNR situations where the interference in the signal can be

attributed directly to some other source such as artifacts introduced by the receiver which may be coherent as well, the improvement in SNR can be less.

The SDR is designed such that almost all core operating parameters of the pulsed doppler radar can be tuned, including the center frequency of operation, the transmitted waveform, the number of pulse returns coherently integrated, the fast PRF of the coherently integrated pulses, and the slower effective PRF of the system used for doppler processing. In addition, the system includes two transmit and receive channels which can be operated fully independently of one another, and through the use of an antenna switch matrix, can be connected to four dual-polarized transmit and four dual-polarized receive antennas. This is accomplished through the use of a dual-channel frequency-tunable RF up/downconverter and a powerful baseband transceiver capable of generating coherent pulse trains in the digital domain. Using high speed sampling devices, all baseband processing including pulse compression and doppler analysis can be accomplished digitally for maximum flexibility. The remainder of this chapter is dedicated to describing this hardware and the corresponding software framework to control the system.

3.2 Hardware

The SDR hardware consists of three distinct sections: a commercially available high speed digital processing system with 1 giga-sample per second (1 GSPS) analog-to-digital (ADC) and digital-to-analog (DAC) converters, a custom multi-channel RF up/downconverter with 500 MHz of instantaneous bandwidth and a tunable center frequency in the 2-18 GHz range, and a switch matrix which multiplexes two transmit and receive channels among an array of antennas. The commercially available digital

transceiver will be outlined first in Section 3.2.1, followed by the tunable RF front end in Section 3.2.2. Finally, the antenna assemblies with the associated antenna switch matrix will be discussed in Section 3.2.3.

3.2.1 Digital Baseband Transceiver and Processor

The SDR is based on a modular digital signal processing platform whose components are commercially available from *Sundance Multiprocessor Technology Ltd.*. A block diagram of the complete platform is given in Fig. 3.2(a). The system consists of two peripheral component interconnect (PCI) carrier cards that are housed in a standard personal computer (PC). Each PCI carrier card has four Texas Instruments module (TIM) sites, allowing each PCI carrier card to support up to four independent TIMs. A TIM adheres to a standard specification for a signal processing component which can include a digital signal processor (DSP), a field-programmable gate array (FPGA), or some combination of the two [28]. Each TIM can have up to six standardized communications ports, referred to as comports, which are accessible through connectors on the backside of the PCI carrier card [29]. These comports are extremely flexible and can be connected together in many different ways using flat ribbon cables called FMS cables. In addition, TIMs can also implement dedicated high speed data links called Sundance High Speed Buses (SHB) [30] which are accessible from the top sides of the modules themselves and provide faster data transfer rates than comports. The SDR uses a combination of both FPGA- and DSP-based TIMS to perform the radar's signal processing tasks. The *Sundance* part numbers for each individual TIM are given in parenthesis in Fig. 3.2(a), and additional information on each of these modules can be found in reference [31]. Fig. 3.2(b) is a photograph of the digital

transceiver hardware as provided by *Sundance Multiprocessor Technology Ltd.*. The SHB connections are emphasized by red arrows.

All four of the TIM sites on the first PCI carrier card are occupied by two quad-DSP modules (SMT395Q), providing the system with a network of eight Texas Instruments TMS320C6416T DSPs. These are 32-bit fixed-point DSPs operating at a 1 GHz clock rate. In addition, each quad-DSP module contains a Xilinx Virtex-II Pro field-programmable gate array (FPGA). These FPGAs implement the fabric required for intercommunication between each of the four processors on a given module. For communication between modules, each quad-DSP module also contains a set a high-speed data bus connections. These can be used to connect the two DSP modules to each other or to modules located on the second PCI carrier card, as indicated in the figure.

The second PCI carrier card houses the ADC and DAC modules. Both the ADC (SMT391) and DAC (SMT381) modules utilize dual-channel devices operating at 1 GSPS for each channel, providing effectively 500 MHz of instantaneous bandwidth in each channel. The DAC is a 14-bit device, while the ADC is an 8-bit device. Since these devices require extremely high data rates, each is attached to its own FPGA module. These FPGA modules (both the SMT368 and SMT368A as shown in Fig. 3.2) utilize Xilinx Virtex-4 SX35 FPGAs to implement the digital interface to the DAC and ADC. In addition, these FPGAs control high speed data buses that connect to the DSP modules housed on the first PCI carrier. On the transmit side, the two data buses are used to transfer samples of the transmit waveforms for each channel from the DSPs to the DAC. On the receive side, the two buses transfer independent channels of sampled data from the ADC to the DSPs for further processing. An

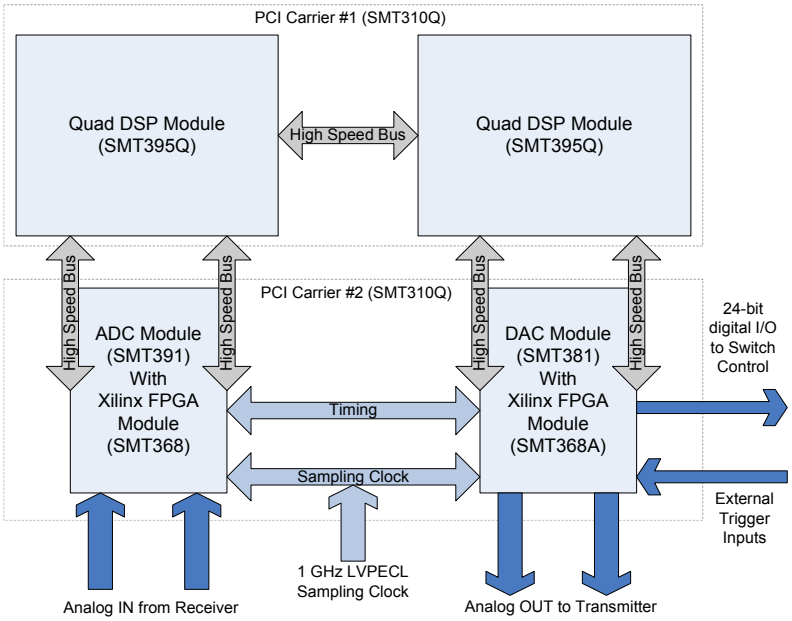

(a) Block Diagram of SDR Digital Transceiver

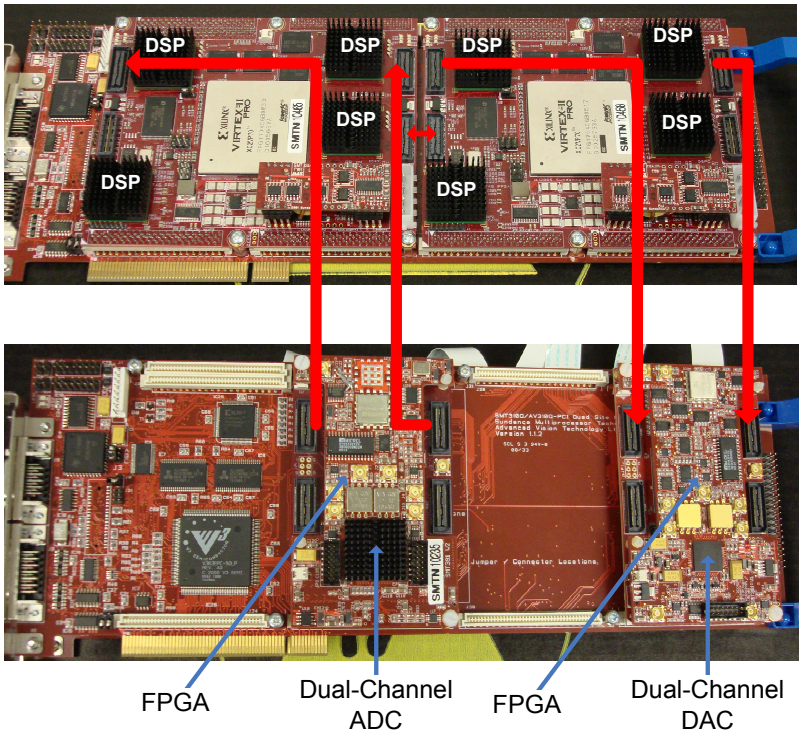

(b) SDR Digital Transceiver Hardware

Figure 3.2: The SDR digital back end consists of two PCI carrier cards. The first carrier card is dedicated to signal processing, while the second holds ADC and DAC modules with their associated FPGAs.

additional digital connection between the FPGAs is used to maintain transmit and receive timing.

For fully coherent operation, the phase between the ADC and DAC sampling clocks must be constant. To achieve this, a common differential low voltage positive emitter coupled logic (LVPECL) clock is generated using a bench source and provided to both modules. This bench source outputs the positive and negative clock signals on separate coaxial cables. However, the SMT391 and SMT381 modules require the differential signals to be combined onto a single coaxial cable such that the positive clock is connected to the inner conductor while the negative clock is connected to the outer conductor. A custom printed circuit board (PCB), utilizing an LVPECL clock distribution integrated circuit (IC), was designed and built which has the proper input connectors for the bench source and output connectors for both the SMT381 and SMT391 sampling modules. Further details of the PCB and sample clock distribution are given in Appendix A.1. The ADC module divides the 1 GHz clock by a factor of four and provides this new 250 MHz clock to its associated FPGA. The DAC similarly divides the 1 GHz clock by two and provides a 500 MHz clock to its FPGA. The FPGAs then further divide these clocks internally for use by the user logic.

The SDR includes an antenna switch matrix to multiplex the two independent transmit and receive channels among a set of eight dual-polarized transmit and receive antennas. To control the high speed switches which comprise this system (described in Section 3.2.3), custom buffer boards have been created which provide access to 24 general-purpose input-output (I/O) pins on the transmitter (SMT368A) FPGA. These I/O pins provide a means to switch between antennas or polarization on a

pulse-to-pulse basis. Additional details on these buffer boards are available in Appendix A.2. The 24-bit output control signals are available on two DB-15 connectors on the back of the PC.

For some SDR applications, it is useful for the system to respond to external triggering signals. To this end, a custom PCB was designed and built which accepts two transistor-transistor logic (TTL) or low-voltage transistor-transistor logic (LVTTL) inputs on SMA connectors and converts them to the LVPECL standard suitable for connecting to two external trigger inputs available on the SMT381. Ultimately, these two independent input signals can be monitored by the transmitter FPGA. Additional details pertaining to this trigger input buffer PCB can be found in Appendix A.3.

The carrier cards in Fig. 3.2(b) are installed in the computer case along with the LVPECL sample clock distribution, FPGA digital output buffer, and trigger input buffer PCBs. Fig. 3.3 shows the organization of the digital transceiver as seen from the back of the PC. Both SMT310Q carrier cards are labeled, along with the dual sample clock inputs, analog baseband inputs and outputs, external trigger inputs, and high speed digital I/O outputs.

3.2.2 Tunable RF Front End

The SDR employs a frequency-agile RF front end to tune the 500 MHz of instantaneous bandwidth afforded by the digital baseband transceiver to a center frequency in the range of 2 to 18 GHz. Since the SDR system is primarily a short range low power radar testbed, the design of the RF front end is significantly simplified by removing the need for extensive receiver protection and high-power amplifiers and switches. Because of this, the up- and downconverter channels are very similar. Block diagrams

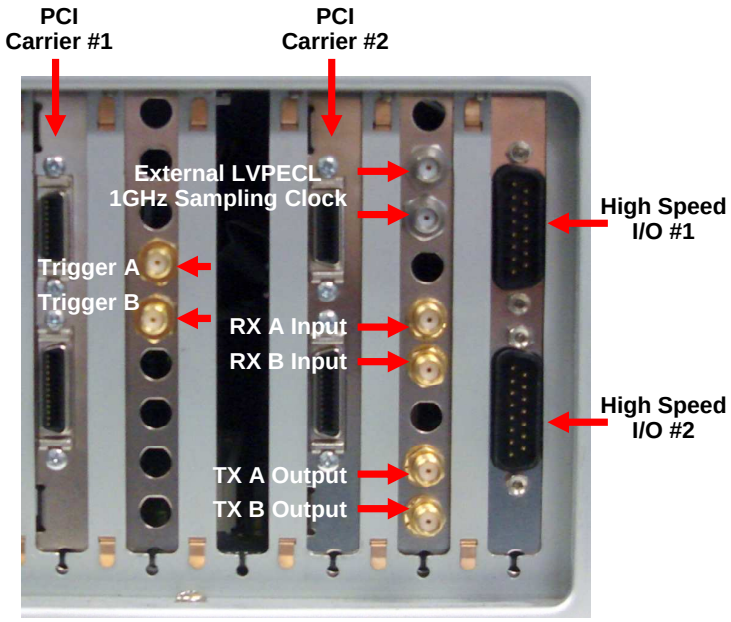

Figure 3.3: Digital transceiver connections present on the back of the PC The connectors on the PCI carriers themselves are unused. All analog connections are standard SMA coaxial connectors, while the high speed I/O connections are standard D-sub-15 cables.

of a single upconverter and downconverter channel are given in Fig. 3.4. Connections to the digital baseband transceiver described in the previous section are on the left hand side of the schematic.

A simplified block diagram of one upconverter channel of the SDR transmitter is illustrated in Fig. 3.4(a), while a single downconverter channel of the receiver is illustrated in Fig. 3.4(b). The complete system utilizes two transmit and two receive channels. The SDR is based on a standard superheterodyne design with two local oscillators (LO). The first LO is fixed at 2 GHz, and the corresponding bandpass filter has a fixed passband from 2-2.5 GHz. This filter is not required to tune, and has sharp transition regions. The second LO is tunable from 500 MHz to 15.5 GHz to place the

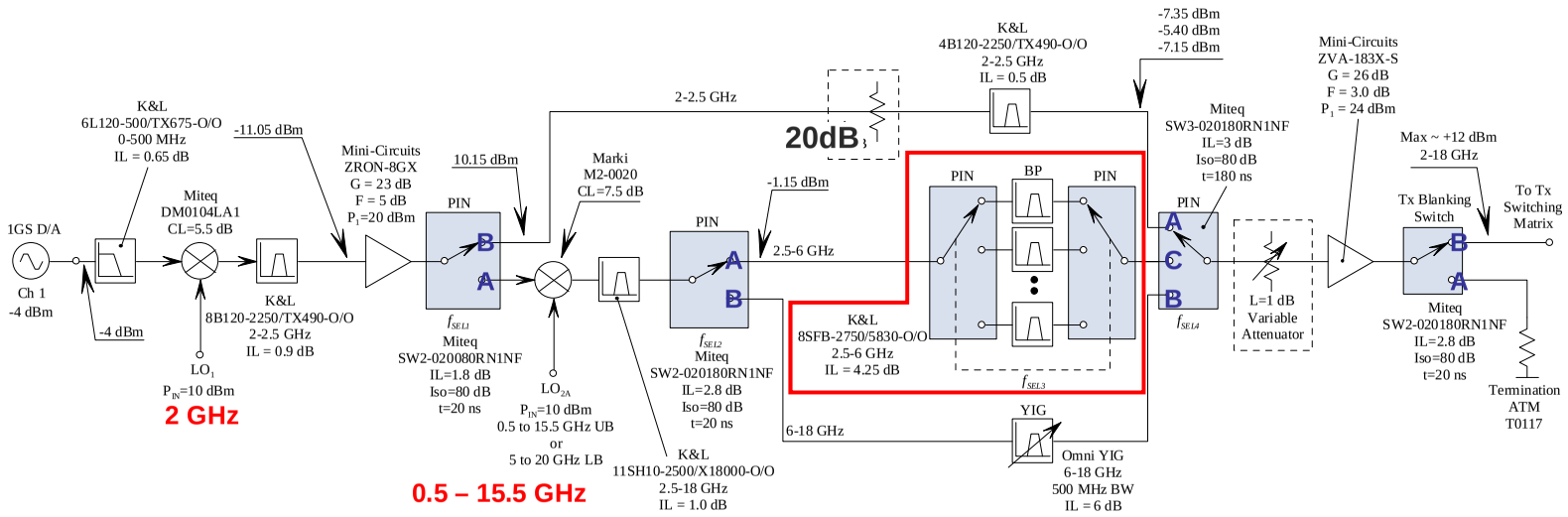

(a) RF Upconverter

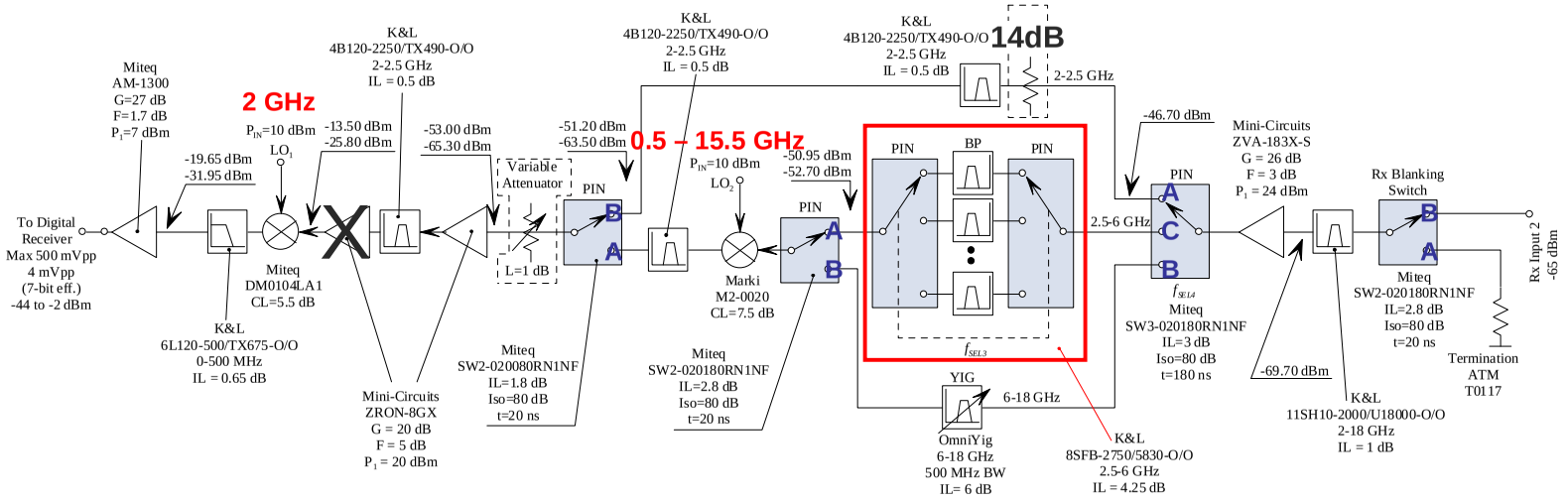

(b) RF Downconverter

Figure 3.4: Schematics of the tunable RF up- and downconverter. While only one channel is shown, the SDR utilizes two independent transmit and receive channels.

center frequency of the radar anywhere from 2-18 GHz. To avoid unwanted images on transmission or aliasing on reception, the second bandpass filter must also be tunable. Current state-of-the-art tunable bandpass yttrium iron garnet (YIG) filters with 500 MHz bandwidth can be tuned from 6-18 GHz and are used to cover that selection of center frequencies. A series of fixed 500 MHz bandpass filters in a self-contained, digitally controllable module (outlined in red in Fig. 3.4) cover the 2.5-6 GHz band in eight discrete steps. Digitally controlled RF switches are used to select one of three paths through the up/downconverters: a direct conversion path which bypasses the second mixing stage (2-2.5 GHz), the discrete bank of filters (2.5-6 GHz), or the tunable YIG filter (6-18 GHz). The selectable bands are described in their entirety in Table 3.1. The final component in each up/downconverter schematic is a high-speed RF switch used for blanking which enables each channel to be selectively enabled or disabled.

Table 3.1: SDR Frequency Bands

RF Path	Center Frequency	Band Edges (3 dB)
Direct Conversion	2.25 GHz	2 - 2.5 GHz
Filterbank #1	2.75 GHz	2.505 - 2.995 GHz
Filterbank #2	3.19 GHz	2.945 - 3.435 GHz
Filterbank #3	3.63 GHz	3.385 - 3.875 GHz
Filterbank #4	4.07 GHz	3.825 - 4.315 GHz
Filterbank #5	4.51 GHz	4.265 - 4.755 GHz
Filterbank #6	4.59 GHz	4.345 - 4.835 GHz
Filterbank #7	5.39 GHz	5.145 - 5.635 GHz
Filterbank #8	5.83 GHz	5.585 - 6.075 GHz
Tunable YIG	6 - 18 GHz (in 10 MHz steps)	$\approx$ 500 MHz bandwidth

To maintain phase coherence across channels, a single 2 GHz source and tunable 500 MHz-to-15.5 GHz source are fed to both upconverter channels and both down-converter channels. The mixers require LO powers of approximately 10 to 11 dBm to operate linearly, so amplifiers are required in addition to four way power splitters. The complete LO distribution system is detailed Fig. 3.5. As mentioned previously, the 10 MHz master sync is provided by the Stanford Research 1 GHz LVPECL sample clock generator. This signal is divided into two and a copy is provided to both the 2 GHz LO, and as an option to sync the external tunable LO. Two tunable RF sources are currently available for use as the second LO: the HP 8350B or the Anritsu 68369ANV. These bench-top sources are tuned, in both frequency and power output, by the software running on the SDR computer using a USB-to-GPIB cable.

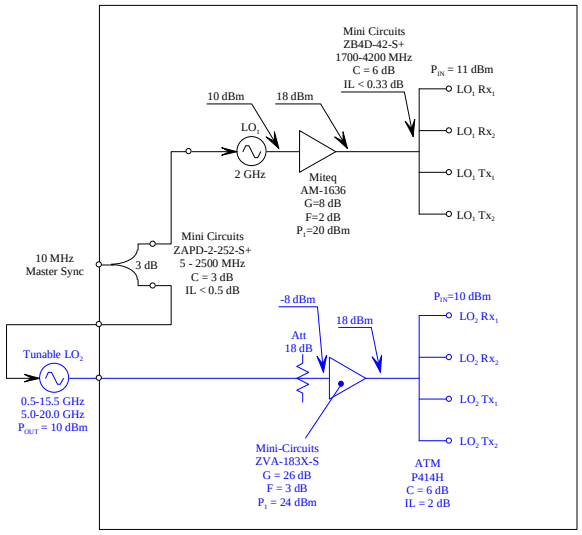

Figure 3.5: SDR LO distribution diagram. The Stanford Research 1GHz LVPECL clock generator provides a low phase noise 10 MHz reference to sync both the internal 2 GHz source for the first LO and the tunable RF bench for the source second LO.

3.2.3 Antenna Switch Matrix

The digital transceiver and up/downconverter described to this point provide two fully independent transmit and receive channels. However, for many applications, more channels would be desirable. To minimize cost and complexity, an antenna switch matrix was designed in lieu of building another complete pair of transmit and receive channels. This antenna switch matrix effectively multiplexes the 2-by-2 transmit and receive channels to 4-by-4 dual-polarized transmit and receive antennas. A hardware schematic is shown in Fig. 3.6.

The two transmitter inputs are on the left hand side of Fig. 3.6, while the two receiver outputs are on the right. Using a series of 4-pol and 2-pol pin diode RF switches, either transmit channel can be connected to any one of four dual-polarized transmit antennas. From the figure, it can be seen that only one transmit channel can be connected to a given dual-polarized antenna at a time. It is also assumed that each dual-polarized antenna and polarization switch (combined in a single module shown later) is connected to the rest of the switch matrix by an RG-8X coaxial cable of up to 50 feet in length. Similarly, the two receive channels can be connected to any of four dual-polarized receive antennas. Again, a coaxial cable up to 50 feet in length can be used to connect the dual-polarized antenna and polarization switch to the rest of the switch matrix. Since the losses in this cable can be quite significant, ranging from 6 dB at 2 GHz to 20 dB at 18 GHz, a low-noise amplifier (LNA) is included as close to the antenna as possible to mitigate the impact of this cable loss on the noise figure of the complete system.

The SDR utilizes eight dual-polarized antenna assemblies. Each of these assemblies includes two linearly polarized antennas, a polarization switch, and possibly

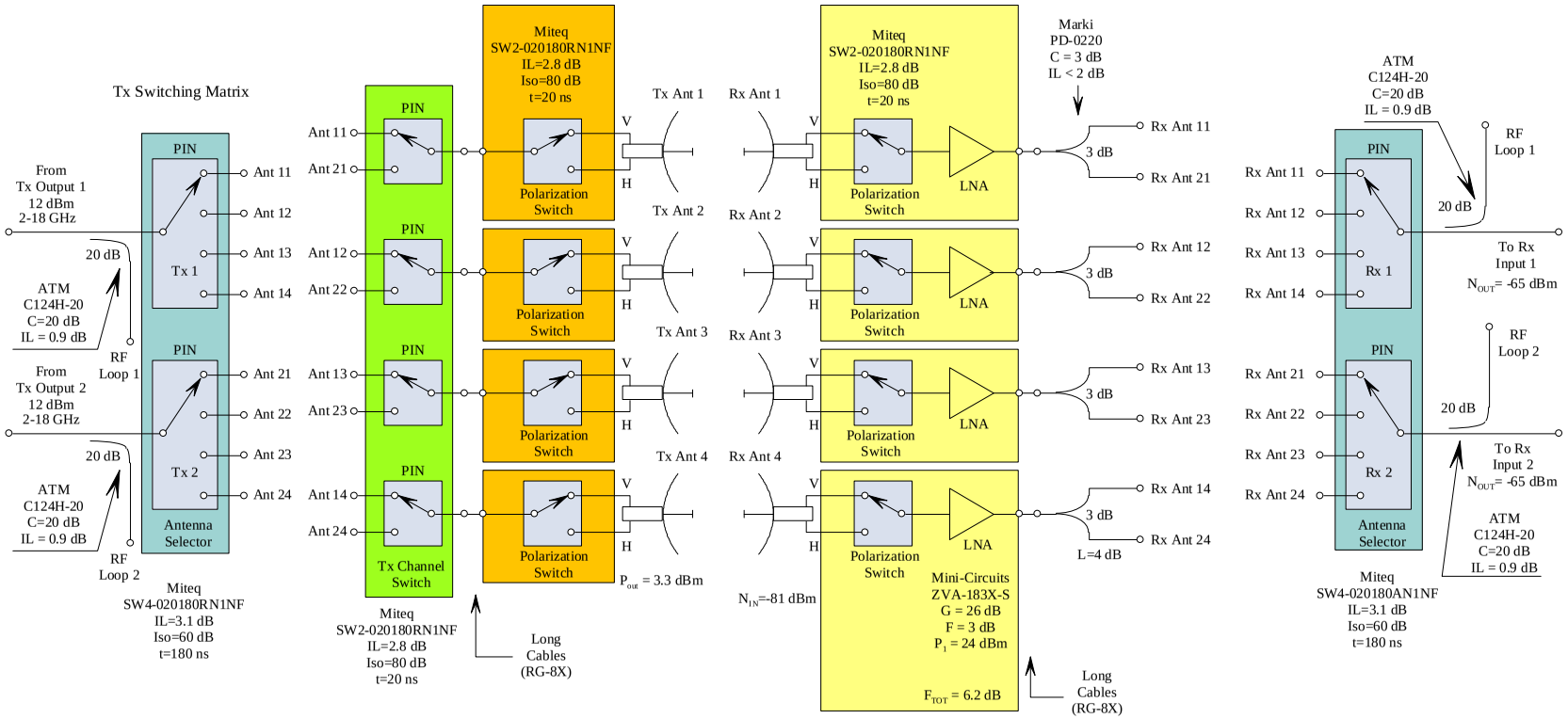

Figure 3.6: The antenna switch matrix provides a way to multiplex 2-by-2 Tx/Rx channels onto 4-by-4 Tx/Rx dual-polarized antennas.

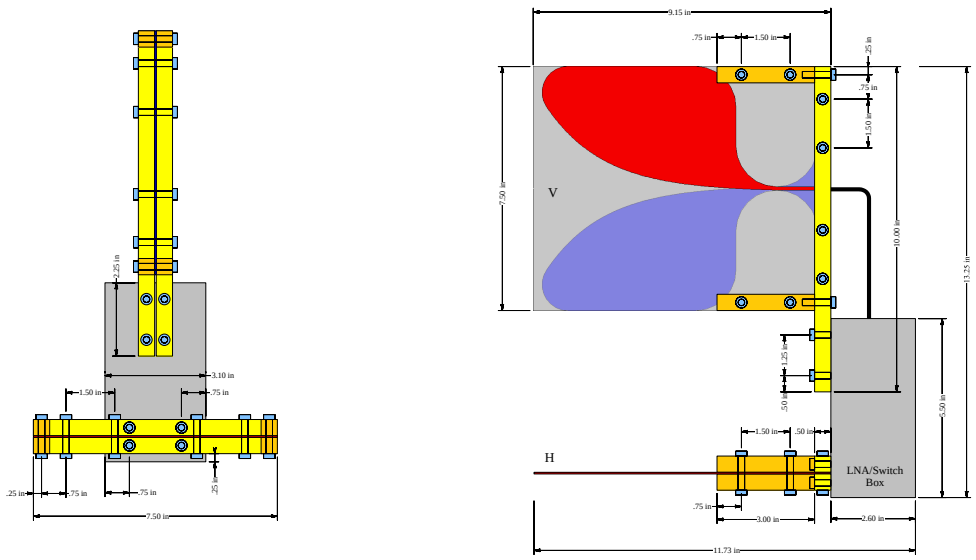

(a) Front View (b) Side View

Figure 3.7: Front and side views of the SDR antenna assembly with horizontally and vertically polarized elements.

an LNA on receive. Mechanical drawings of these assemblies are given in Fig. 3.7. The antennas themselves are antipodal Vivaldi designs as outlined in [32, 33] which provide reasonable gain from 2 to 18 GHz and are inexpensive to manufacture. The measured antenna gain varies from 8.5 to 13.5 dBi over this range. An example of a completed antenna assembly mounted on an adjustable tripod is shown in Fig. 3.8. A coaxial SMA connector provides a simple RF connection, while a standard 8P8C (commonly called RJ-45) connector provides power and control for the polarization switch and optional LNA.

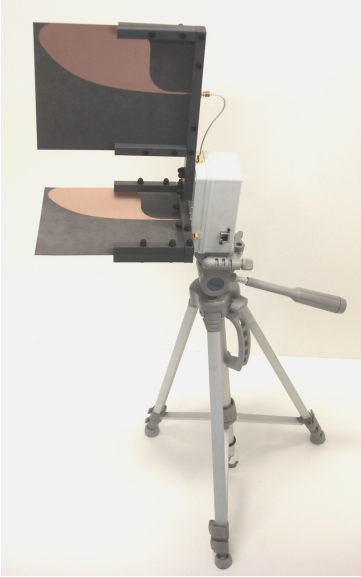

Figure 3.8: Dual-polarized antenna assembly mounted on an adjustable tripod. The coaxial SMA connector for analog RF and 8P8C (commonly called RJ-45) connector for power and control are visible on the side of the gray electrical box.

One final feature in the schematic in Fig. 3.6 are the four directional couplers located on the two RF inputs and two outputs of the switch matrix. The coupled ports on each transmitter channel can be optionally connected to the coupled ports on each receive channel to provide a direct path from transmitter to receiver. This is useful for providing a near-zero-range reference to the radar which is uncorrupted by the antennas and propagation channel.

3.2.4 Final Assembly

Each RF up- or downconverter channel has been assembled in a modular fashion using connectorized components by Ninoslav Majurec, a Senior Research Scientist at the ElectroScience Laboratory - the Ohio State University who was also instrumental in the SDR's RF design. The channels have been organized onto four separate metal

plates for final assembly into a custom instrument enclosure. A fifth metal plate has been used for LO distribution and RF switches pertaining to the antenna switch matrix discussed in the previous section. Photos of each of these plates before assembly into the final enclosure are shown in Fig. 3.9. Each metal plate has two sets of connectors. The up- or downconverter plates utilize standard D-sub-25 connectors with digital control inputs for the tunable YIG filter, the discrete filterbank, and the four RF switches. On the LO distribution plate, this D-sub-25 connector contains digital control inputs for all RF switches in the antenna switch matrix excluding polarization switches. On all five plates, screw-down terminals are used for power distribution. Fig. 3.10 shows the five plates mounted in a vertical fashion in the final instrument enclosure. From top to bottom, the stackup is upconverter A, upconverter B, LO distribution and switching, downconverter A, and downconverter B. In addition to the five stacked plates, the instrumentation enclosure also includes the necessary power supplies for all components mounted in the box.

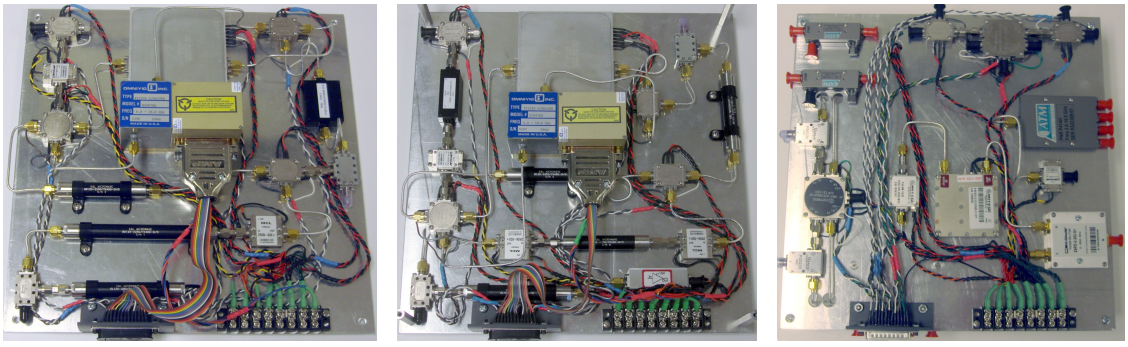

(a) RF Upconverter (b) RF Downconverter (c) LO Distribution

Figure 3.9: Up- and downconverter hardware is separated and mounted on four individual plates, with a fifth used for LO distribution and RF switching.

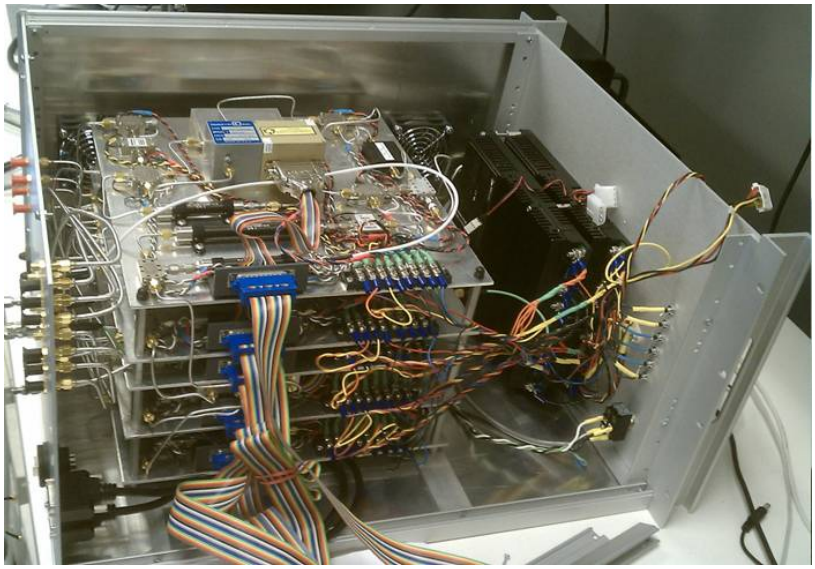

Figure 3.10: The five plates containing the RF hardware are stacked in a custom metal box. From the top, the stackup is Tx channel A, Tx channel B, LO distribution and switching, Rx channel A, and Rx channel B.

The SDR PC is used to control the tunable YIG filter, the discrete filterbank, and the four RF switches on each plate. This is accomplished using a USB-DIO96H/50 device from *Measurement Computing* [34]. This device provides 96 bits of digital I/O which are controllable through a standard USB connection. These digital I/O signals are split across two 50-pin ribbon cables. For convenience, a custom printed circuit board, called the RF front end control PCB, was designed and manufactured which mates with these two 50-pin connectors and breaks the 96 bits out into four separate connectors containing 24 signals each. Four ribbon cables then form the final connection from the PCB to each D-sub-25 connector on the up/downconverter plates. As mentioned in Section 3.2.1, the digital baseband transceiver provides an additional 24 bits of high speed digital control for the antenna switch matrix. Cables from two D-sub-15 connectors on the back of the PC (see Fig. 3.3) connect to the

custom PCB in addition to the two 50-pin cables from the USB-DIO96H/50. An FPGA module on the RF front end control PCB decodes these 24 bits generating the logic levels required to drive RF switches in the antenna switch matrix. Control signals excluding those for the polarization switches are routed to a the fifth ribbon cable connector on the PCB to connect to the LO distribution and switching plate. The polarization switch control signals and power, on the other hand, are routed to a set of eight 8P8C (Ethernet) connectors. Standard Cat-5E Ethernet cables are then used to route these signals to each of the eight antenna assemblies. Fig. 3.11 shows how the USB-DIO96H/50 device and the RF front end control PCB are connected together inside the RF instrument enclosure. Additional details on the RF front end control PCB can be found in Appendix A.4.

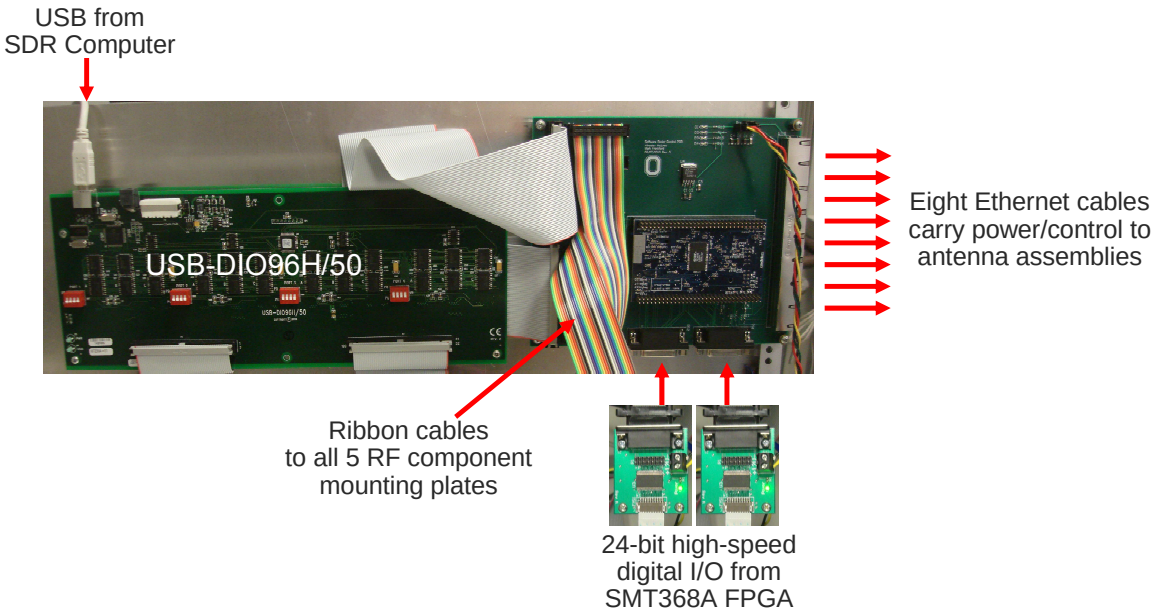

Figure 3.11: The RF hardware is controlled using a combination of slower control signals from the PC and higher speed control signals from the transmitter FPGA.

With the RF instrument enclosure complete, access to all analog and digital I/O are available on the back panel. The locations for each are shown in Fig. 3.12. RF and digital connections to each of the eight antenna assemblies are located in a row in the upper right corner. USB and high speed digital control inputs from the SDR PC and digital baseband transceiver are located in the lower right, while analog connections to the digital baseband transceiver are located just right of center.

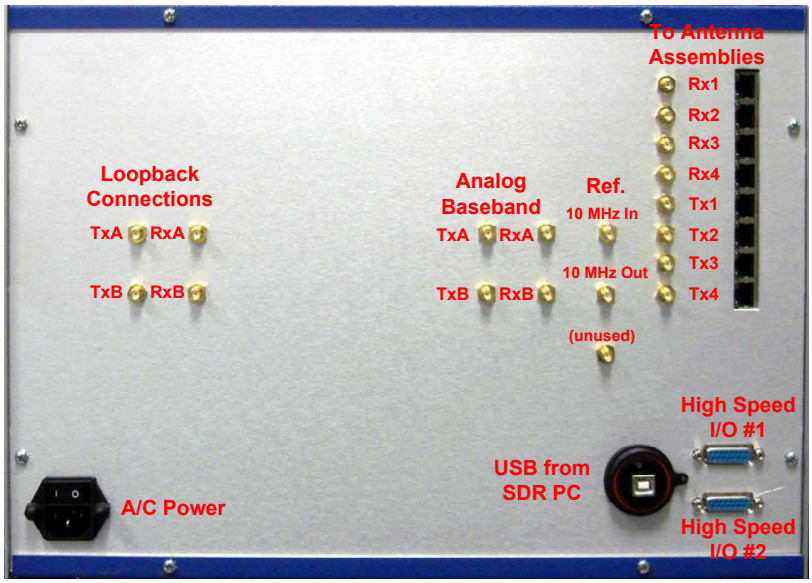

Figure 3.12: Diagram of connections on the back of the custom RF instrumentation enclosure. The tunable LO input is located on the front of the enclosure.

Fig. 3.13(a) shows how the components discussed in the previous sections are integrated together into the complete SDR system. The complete system consists of four major components: the Standford Research LVPECL clock generator, the tunable RF source (either the HP 8350B or Anritsu 68369ANV), the SDR PC, and the custom RF instrument enclosure. Both the SDR PC containing the PCI-based digital

baseband transceiver and the custom RF instrument enclosure were constructed to be rack-mountable. In the final rack-mounted system in Fig. 3.13(b), the tunable RF source is on the bottom, followed by the custom RF enclosure. The SDR PC is the black box mounted above the RF enclosure with space left between them to open the RF enclosure if necessary. The LVPECL clock generator sits on a shelf just above the PC. Long (up to 50 ft.) RF coaxial cables and Cat-5E Ethernet cables connect the eight antenna assemblies (not shown here) to the RF enclosure.

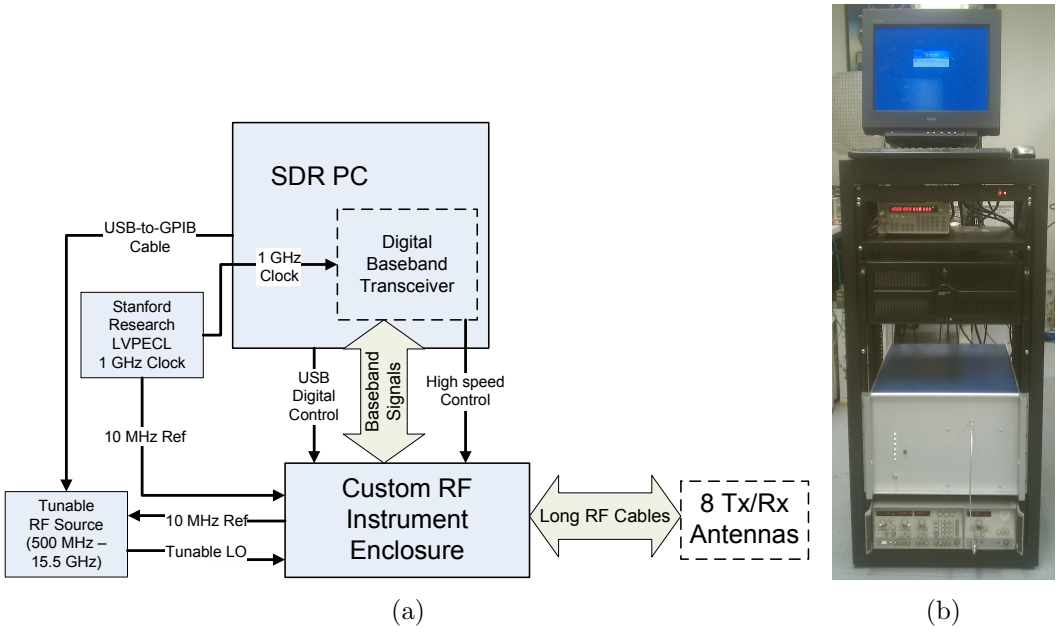

Figure 3.13: Schematic and photo of assembled SDR system in rack.

3.3 Software

The previously described SDR platform is very flexible and capable of operating in a variety of different sensing scenarios. To realize the full potential of the hardware,

an equally flexible software framework has been developed which allows the researcher to quickly reconfigure the radar for a given task, often with little or no changes to the source code. In addition, should some changes be required, the code has been written in a modular way which is easily modified and extended.

The SDR software framework can be separated into two distinct domains: software which runs on the SDR PC, and software which runs on the digital transceiver. Furthermore, each portion of the code can be further divided as illustrated in Fig. 3.14. The SDR PC boots into a standard installation of *Microsoft Windows XP* (Service Pack 3) and includes a graphical user interface (GUI) and a dynamic-link library (DLL) called a cluster. These will be discussed in depth in Section 3.3.2. The digital transceiver utilizes a real-time operation system (RTOS) from 3L called *Diamond* to run software both on the network of eight Texas Instruments (TI) DSPs and the two Xilinx Virtex-4 SX35 FPGAs. The DSP and FPGA software will be discussed in depth in Sections 3.3.3 and 3.3.4 respectively. Before discussing the software in earnest, however, it is first useful to first outline the development tools used to program the system including the 3L *Diamond* RTOS and associated utilities.

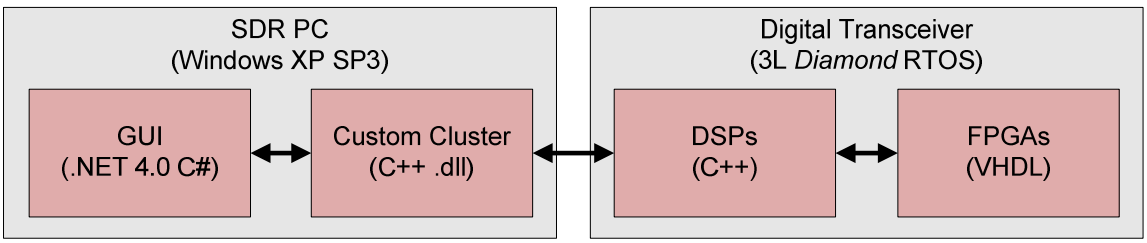

Figure 3.14: The SDR software framework can be divided into four distinct parts: the graphical user interface, custom cluster, DSP code, and FPGA code.

3.3.1 RTOS and Development Environment

The SDR baseband transceiver is a complicated digital system with a network of eight TI DSPs and four Xilinx FPGAs. Writing software from scratch which is both computationally efficient and utilizes all of the resources available in the network would be a monumental task. Even simply loading a program into each of these devices would be difficult and time-consuming if done manually. Therefore, to speed development, the *Diamond* system from 3L [35] is utilized which effectively extrapolates most of the hardware specifics away from the programmer, allowing focus to be placed on signal processing and not the nuances of the underlying hardware. In addition, the system combines the programming operations for all processors in the system into one simple step. The *Diamond* system, as implemented for the SDR, consists of essentially two parts: a light-weight RTOS with programming library, and an integrated development environment (IDE).

Before beginning to program using the *Diamond* system, a few simple steps must be performed to set up a project in the IDE for the specific set of *Sundance* modules present in the digital transceiver. The first step is to add each processor to the project in the IDE by choosing them from a list of pre-defined selections of available *Sundance* hardware. In this case, eight SMT395Q DSPs, two SMT395Q FPGAs, an SMT368 FPGA, and an SMT368A FPGA are defined which correspond to the modules in the SDR system outlined in Fig. 3.2(a). Next, the programmer uses the IDE to tell *Diamond* how these processors are physically connected using comports and SHBs. Fig. 3.15 expands on Fig. 3.2(a) by showing the actual physical connections between modules in the SDR. These connections are labeled input:output, with the CP- and SHB- prefixes referring to comports and SHBs respectively. Once this is finished, the

Diamond system has a complete description of the layout of the physical hardware and its processing and communications capabilities and can properly build code for this system.

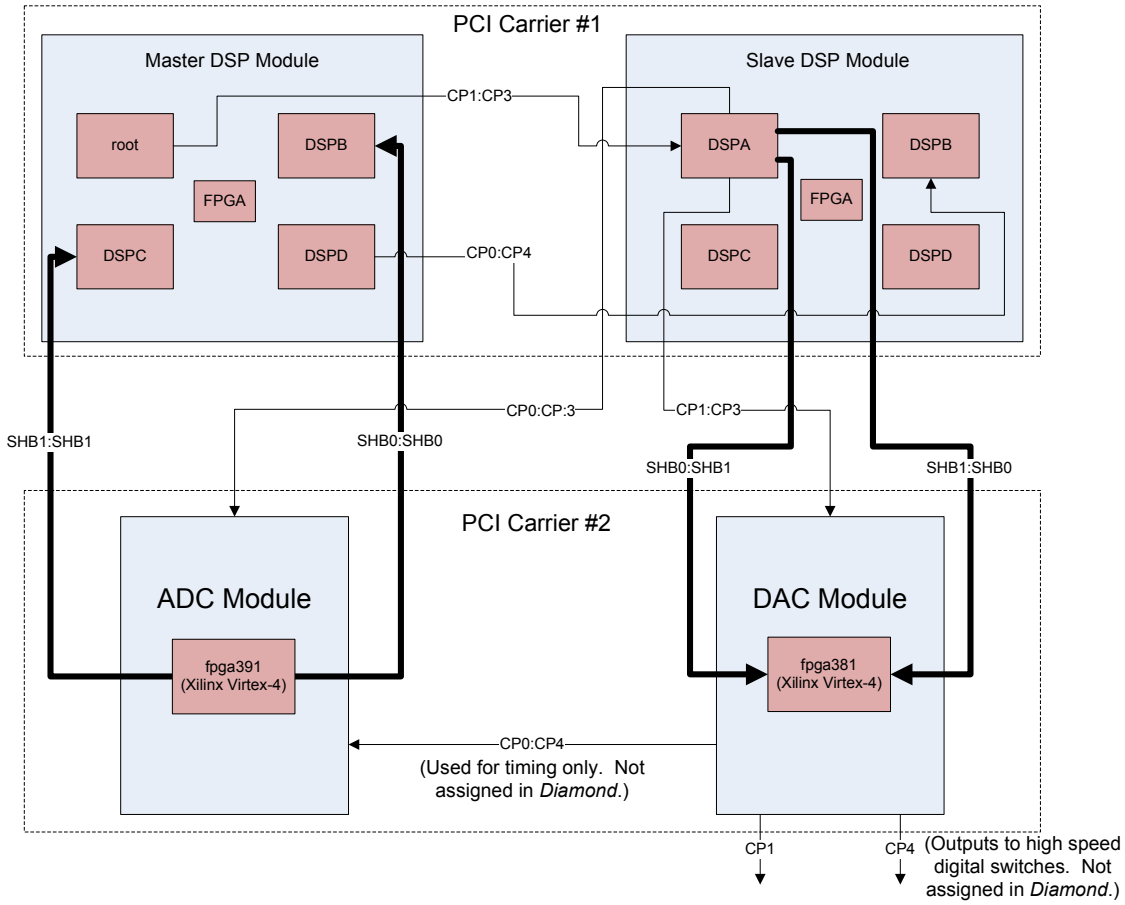

Figure 3.15: Diagram of physical comport and SHB connections between processors in the SDR digital transceiver.

Once the network of processors and communications buses have been defined in the *Diamond* IDE, the programmer can then assign tasks to each processor in the network. For DSPs, a task is essentially a single processing thread which has it's

own block of memory and user-defined input and output ports. An example of a task might be one that implements a simple filtering operation with a single input port and a single output port. The code in this basic filtering task would perform three steps: read data from the input port, perform the actual filtering operation on the data, and write the data to the output port. Using this organizational strategy, it is easy to compartmentalize complex signal processing systems into smaller, more manageable functions encapsulated in tasks. Once the tasks have been written, the programmer uses the IDE to tell *Diamond* which input and output ports are connected together. It is important to note that tasks don't need to reside on the same processor or even the same module to be connected together. If two tasks are connected together but reside on different processors, the *Diamond* RTOS will automatically figure out at run time how to transfer the data from one processor in the network to another when required. This makes distributing tasks across the network of processors a trivial problem. In addition, should the programmer decide later that tasks need to be shifted to different processors, it is a simple matter dragging and dropping with no changes to the underlying code.

The first DSP on the SMT395Q in the first TIM site on the first PCI carrier card is special, and is designated as the *root* processor. This is the only processor in the system which has direct access to the PCI bus, and ultimately software running on the host computer. The *Diamond* system includes an application called the 3L Server which is used to load a program on the network of processors over the PCI bus, starting first with the root processor. The root processor then loads all processors which are directly connected to it using comports. By default, all processors listen on comport 3 for programming at startup. Each subsequent processor then loads the

processors which are directly accessible and so on. All processors then wait for a signal from the Server to begin execution.

The *Diamond* RTOS allows each processor in the network to access the standard streams (standard in (STDIN), standard out (STDOUT), and standard error (STDERR) typically available to a Unix or windows console program) provided by the Server. For example, the ubiquitous "*printf*" function typically writes text to STDOUT. When a task running on any processor in the digital transceiver calls the "*printf*" function, the RTOS automatically routes that text through the network to the root processor. The root processor then communicates with the Server over the PCI bus to ultimately write the text to the Server's console where it is visible to the user. This entire process is completely transparent to the programmer. In addition to supporting the standard streams, the 3L Server application also supports custom interface functions defined in external DLLs called clusters. These clusters are loaded by the Server whenever the the root DSP attempts to interact with a function defined in the cluster. In this way, the Server can be customized to support more complex messaging schemes to transfer data back and forth between processes running on the host computer and tasks in the root DSP. The cluster developed specifically for the SDR system is discussed in more detail in Section 3.3.2.

Fig. 3.16 outlines the complete development system, including the 3L *Diamond* IDE and 3L Server discussed previously. As noted in the figure, the IDE calls both the *TI Code Composer Studio 3.3* and *Xilinx ISE 10.1* development tools to build the DSP and FPGA code respectively. The *Diamond* system combines the compiled outputs for each of these tools for all processors in the system into a single **.app* file. Opening this file with the 3L Server programs all processors in the digital transceiver

and begins execution. The software executing on the DSPs can be debugged using the *Parallel Debug Manager* for *Code Composer Studio 3.3*, while the FPGA logic can be monitored using the *Xilinx ChipScope 10.1* tool. Monitoring of the logic in a specific FPGA requires the connection of an external *Xilinx Platform Cable USB II* to the FPGA's JTAG port. *Microsoft Visual Studio Professional 2010* is used to develop both the custom cluster and the SDR graphical user interface.

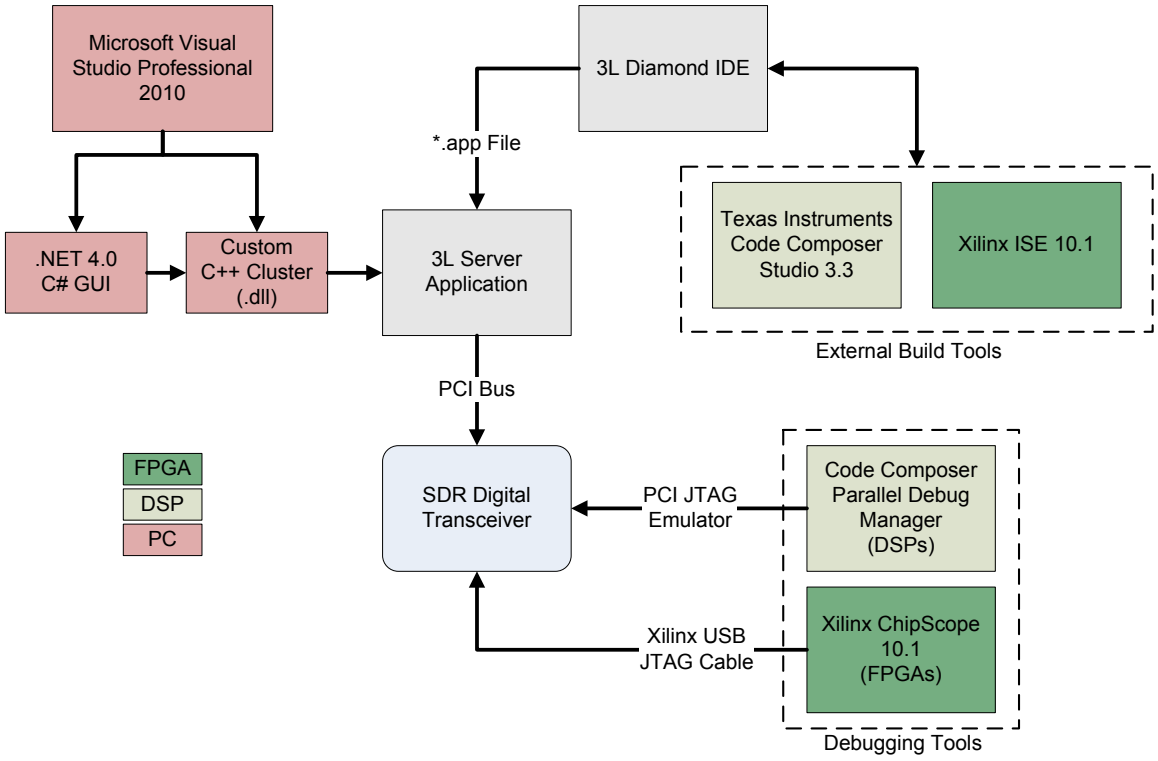

Figure 3.16: SDR software development environment for both the PC and digital transceiver.

3.3.2 Graphical User Interface

The SDR's graphical user interface (GUI) provides a simple way for the user to configure the radar's operating parameters and view radar returns in real time. It was built using Microsoft's *.NET 4.0* framework and is written in C#. A screen capture of the GUI is shown in Fig. 3.17 with some of the important features labeled. Buttons to connect and disconnect the GUI from the digital transceiver (using the cluster discussed later) are located in the upper right corner of the GUI. Specific radar operating parameters are entered in text boxes located in the upper right region which define the timing of the coherent pulse train described earlier in Fig. 3.1. The radar's center frequency of operation, including selection of one of the three RF paths (direct conversion, discrete filterbank, or tunable YIG filter) in the up/downconverters, can be modified directly below the text boxes. Additionally, drop-down boxes are provided to define which polarized antenna each transmit and receive channel is connected to. Clicking the update button propagates all changes made in the GUI to the different sections of radar hardware.

In addition to allowing the user to modify the radar's operating parameters, the GUI also displays real-time range and doppler information in the form of range/doppler maps. These maps, formed from pulse compressing and doppler processing 128 coherent range returns, are two-dimensional (2D) color images for which the horizontal axis represents range and the vertical axis represents doppler. Stationary targets appear along the horizontal centerline, while targets moving away from the radar appear above the centerline and targets moving towards radar appear below. The GUI generates these range/doppler maps from complex-valued 2D range/doppler matrices

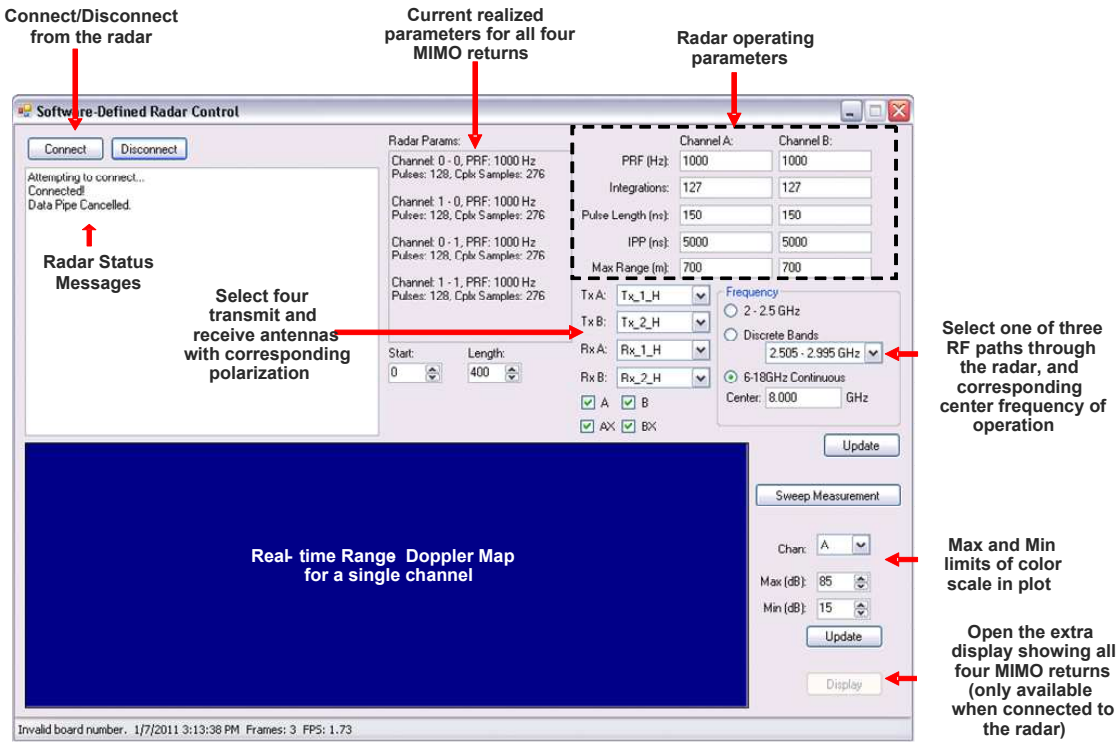

Figure 3.17: SDR primary graphical user interface.

generated by the digital transceiver. The digital transceiver generates and transfers four of these matrices at a time since the range return from each receiver is pulse compressed using matched filters corresponding to both transmitted waveforms (range return A with transmitted waveform A, range return A with transmitted waveform B, range return B with transmitted waveform A, and range return B with transmitted waveform B). The GUI can selectively display one of the four at any given time in the blue rectangle in Fig. 3.17. Additionally, two optional external displays are available which can present all four sets of data simultaneously. The first display, as illustrated in Fig. 3.18(a), shows all four range/doppler maps in a grid. In some situations, it is more useful to display the magnitudes of only the stationary returns. Fig. 3.18(b) shows a screenshot of the second external display which simply plots all four stationary returns on a single line graph. These correspond to the magnitudes along the centerlines of each range/doppler map.

The GUI and digital transceiver communicate with one another by way of a custom cluster loaded by the 3L Server. This relationship is outlined in Fig. 3.19. A task running on the root DSP in the digital transceiver called *SDR_Interface* makes calls to functions defined in the custom cluster. The *Diamond* RTOS routes these calls over the PCI bus to the Server which subsequently loads the DLL corresponding to the appropriate cluster. Specifically, the *SDR_Interface* task calls a function in the cluster to create a *named pipe* interface on the PC and wait for a client to connect to it. A named pipe is a standard programming technique for bidirectional inter-process communication which can be thought of in simplest terms as one process writing to a file while another reads from it. More information on named pipes can be found in [36]. When the user clicks the 'Connect' button on the GUI, the GUI creates a

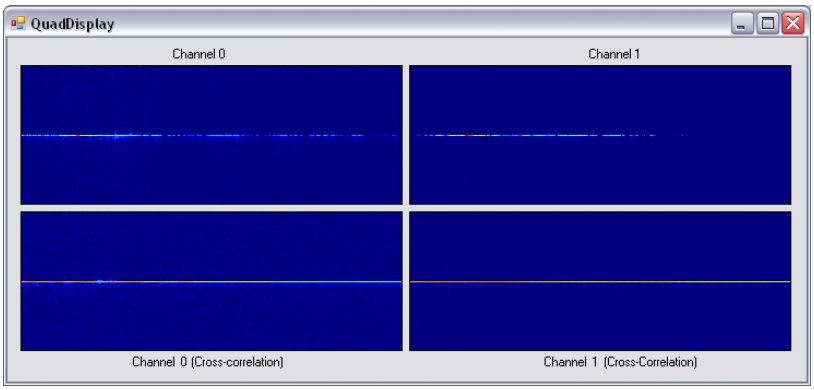

(a) Full Range/Doppler Images Display

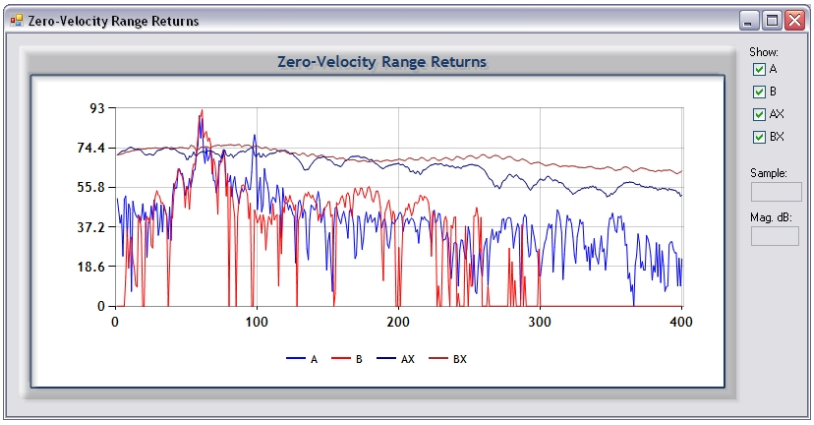

(b) Zero-Doppler Range Profiles Display

Figure 3.18: Optional external real-time displays for range/doppler data.

special process on a background thread to connect to the named pipe in the cluster. At this point, the *SDR_Interface* task calls another function in the cluster which simply waits for new radar operational parameters to be written to the named pipe by the GUI. The GUI incorporates all the pertinent settings entered by the user into a single data structure which is written to the named pipe. The waiting cluster function then reads this data from the named pipe and returns it to the *SDR_Interface* task running on the root DSP. The radar then generates range/doppler matrices using these settings, and the *SDR_Interface* task calls one final cluster function to write all four range/doppler matrices to the named pipe where they are read by the GUI and displayed. It should be noted that all data transfers over the PCI bus between the DSP task and the cluster are handled within the framework of the *Diamond* system and are transparent to the programmer.

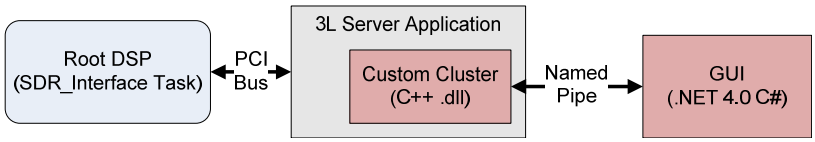

Figure 3.19: Bidirectional data path from the *SDR_Interface* task on the root DSP to the the GUI.

The GUI is written using standard object-oriented programming practices which allows the code to be compartmentalized into classes, the most important of which are outlined in Fig. 3.20. The *MainForm* class is the entry point of the program and handles all user interaction with the graphical form shown previously in Fig. 3.17. Pressing the *Connect* button on the form creates an instance of the *NamedPipeConsumer* class on a background thread which handles all interaction with the named

pipe interface to the cluster as alluded to earlier, leaving the main GUI thread free to respond to user inputs. The radar operating parameters entered into the GUI by the user are interpreted and written to an instance of the *LockedParams* class when the user clicks the *Update* button. This class acts as a thread-safe data transfer device between the main GUI thread and the background thread. The *NamedPipeDataWorker* class reads this data and communicates it to the cluster as outlined previously over the named pipe and reads the resulting range/doppler data generated by the digital transceiver. This data is optionally displayed on the two available external interfaces or the main form. Aside from writing certain radar parameters to the *LockedParams* class, the *MainForm* class is also responsible for interacting with the *RFcontrol* class which models all of the switches in the RF up- and downconverters and interfaces with the USB-DIO96H/50 device (in Fig. 3.11). The *RFcontrol* class in turn utilizes the *RFSourceControl* class to adjust the frequency and output power of the SDR's external tunable RF source (either the HP 8350B or Anritsu 68369ANV) using a USB-to-GPIB cable. The *Parker6k4_com6srvr* class is not currently used, but enables the SDR to control a variety of stepper motor positioners such as linear slides or rotator tables.

3.3.3 DSP Software

The software in the digital transceiver is divided into two sections: software on the network of DSPs and software on the FPGAs. Some functions such as the high speed interfaces to the dual-channel ADC and DAC devices must be performed by the FPGAs. Other functions such as the interface to the cluster on the SDR PC must be performed by a DSP. However, some types of signal processing, such as pulse

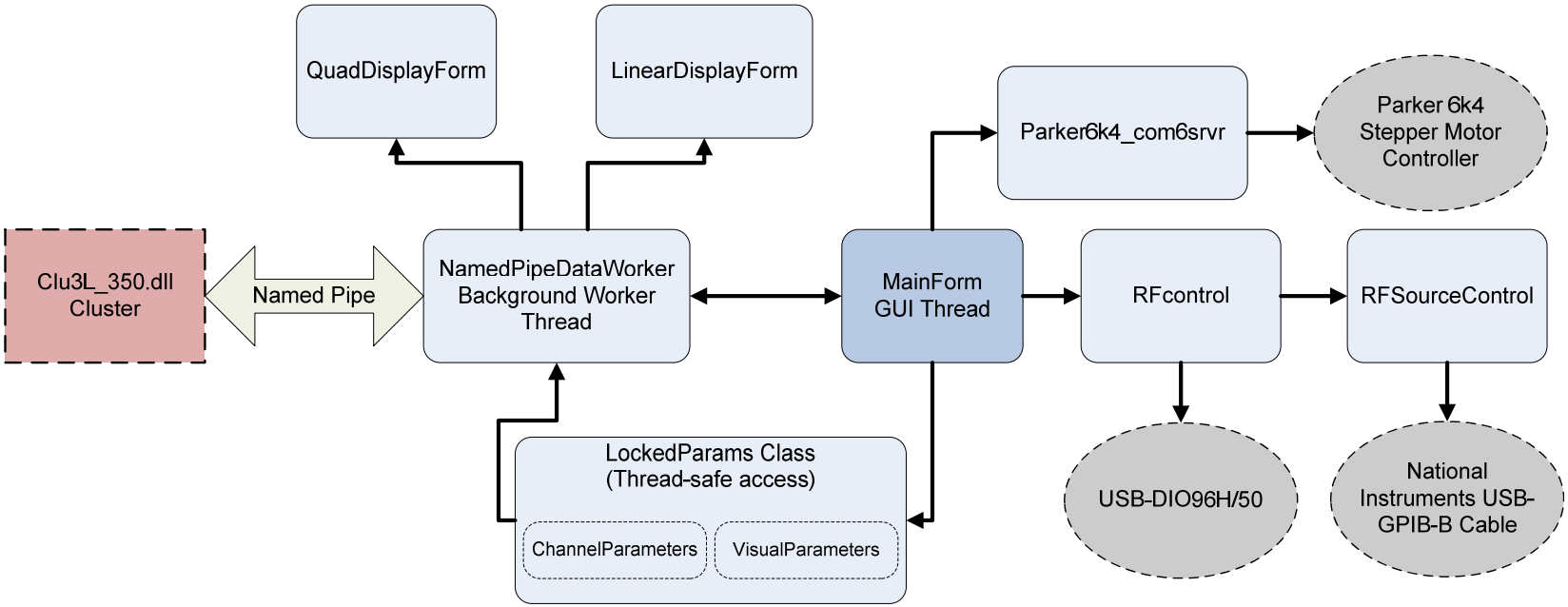

Figure 3.20: Block diagram of classes in C# which comprise the SDR graphical user interface.

compression for example, could be performed by either a DSP or an FPGA. Since one of the primary design goals of the SDR system is flexibility, most of the signal processing tasks are performed on the easily programmable network of DSPs leaving only those tasks which require precise timing to be performed by the FPGAs. Only six of the available DSPs are currently utilized in the basic SDR software framework, leaving two DSPs available for future expansion.

As discussed previously, software on the network of DSPs utilizes the *Diamond* RTOS, with six of the available eight SMT395Q processors having been defined in the *Diamond* IDE. All signal processing functions have been divided into tasks and assigned to the appropriate processor in the network. Fig. 3.21 provides an overview how these tasks are connected together, with the color of the task denoting to which processor the task is assigned. Black dotted lines in the figure delineate the separation between the two SMT395Q modules.

The *SDR_Interface* task, as mentioned previously, is responsible for communicating with the cluster and ultimately the GUI. It establishes a named pipe connection with the GUI from which it receives the radar's core operating parameters. These parameters are forwarded on to the *Synchronizer* task, which is responsible for ensuring that the signal processing tasks in the radar occur in the right order. To achieve this, the *Synchronizer* first instructs the *WaveformGen (A and B)* tasks to create real-valued samples of the transmit waveforms and write them to the transmitter FPGA. Then the *Smt381Control* and *Smt391Control* tasks are instructed to write the appropriate operating parameters to the transmitter and receiver FPGAs respectively. When this is complete, the *Smt381Control* task triggers the transmitter FPGA to begin transmitting a coherent pulse train. At this point, the receiver FPGA begins

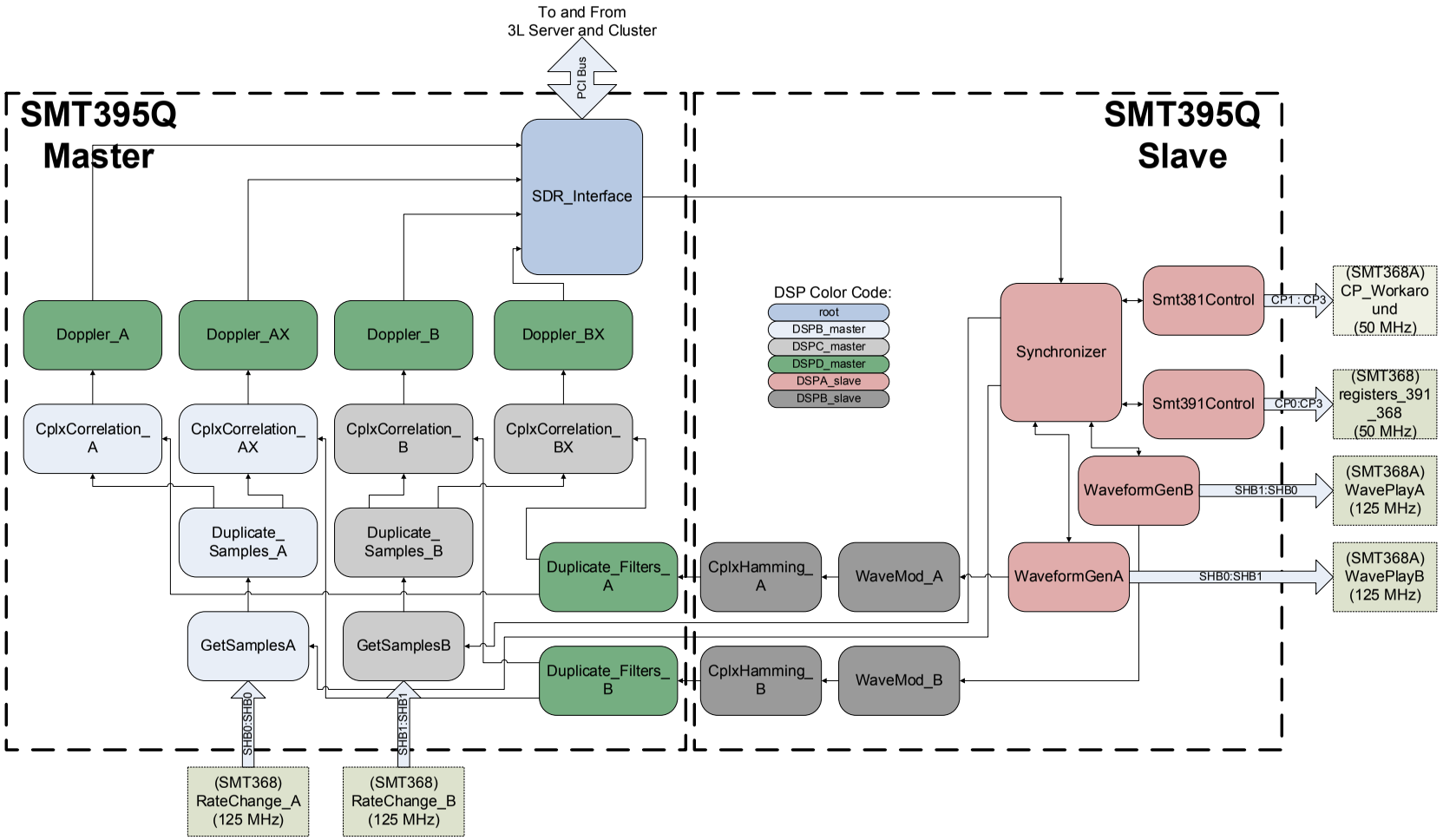

Figure 3.21: Block diagram of signal processing tasks utilizing six of the eight available DSPs in the digital transceiver.

sampling the received signal and generating complex-valued range returns, which are read into the DSPs by the *GetSamples (A and B)* tasks. The transmitter and receiver FPGA functionality are discussed in the next section.

In addition to writing the real-valued transmit waveforms to the transmitter FPGA, the *WaveformGen (A and B)* tasks also forward these waveforms on to the *WaveMod (A and B)* tasks. Here, complex-valued versions of the transmit waveforms are created using a quadrature demodulation process. The complex-valued waveforms are then time-reversed and a complex conjugate operation is applied, with the net result being that the output of the *WaveMod (A and B)* tasks are the matched filters of the transmitted waveforms. The *CplxHamming (A and B)* tasks then apply Hamming windows to the matched filters. This improves sidelobe performance in the subsequent pulse compression operations.

Once the *GetSamples (A and B)* tasks have finished reading the complex-valued range returns for all pulses in the coherent pulse train, the samples are sent to the *Duplicate_Samples (A and B)* tasks which essentially make two copies of each channel to forward on to two of the *CplxCorrelation (A, B, AX, and BX)* tasks. In a similar manner, the complex-valued matched filters are duplicated in the *Duplicate_Filters (A and B)* tasks. Each *CplxCorrelation* takes in the range returns from one receiver channel and the matched filter from one transmitter channel and performs the matched filtering operation for all range returns in the coherent pulse train. In this manner, all four combinations of transmitter and receiver pairs are processed in parallel for every coherent pulse train. Once this is complete, the pulse-compressed samples are sent to the *Doppler (A, B, AX, and BX)* tasks. Here, fast Fourier transforms (FFT) are computed across every range bin of the coherent pulse train to analyze the phase for

doppler information. This final pulse-compressed and doppler-processed data is sent to the *SDR_Interface* task where it is forwarded to the GUI for display. At this point, the GUI responds with new core operating parameters and the process is repeated.

3.3.4 FPGA Software

While the higher order signal processing tasks such as waveform generation, matched filter, and doppler processing have been reserved for the DSPs in the digital transceiver, tasks which require high speed with finely controlled timing are reserved for the FPGAs. The transmitter FPGA on the SMT368A module will be discussed first, followed by the receiver FPGA on the SMT368 module.

Transmitter FPGA

Similar to the DSPs, the FPGA software is divided into tasks. As discussed previously, tasks in the DSPs write real-valued waveforms to the transmitter FPGA. The *WavePlay (A and B)* tasks read in these waveforms and store them in memory to be played back in the form of a coherent pulse train as outlined in Fig. 3.1. Parameters which define the length of the transmit pulse, the length of the inter-pulse period (IPP) which in combination with the pulse length determines the fast PRF, the number of pulses to be coherently integrated, and the overall PRF of the system are written to registers in the *registers_381* task. High speed switch settings for the antenna switch matrix are also written to these registers and forwarded to the *Digital_IO* task which provides the 24-bit output to the RF front end control PCB.

When signaled by a DSP write to a specific register, the *PRF_CTL (A and B)* tasks begin sending triggers to the *WavePlay* tasks with very finely controlled timing. This is done at the rate of the overall PRF of the system. For every trigger, the *WavePlay*

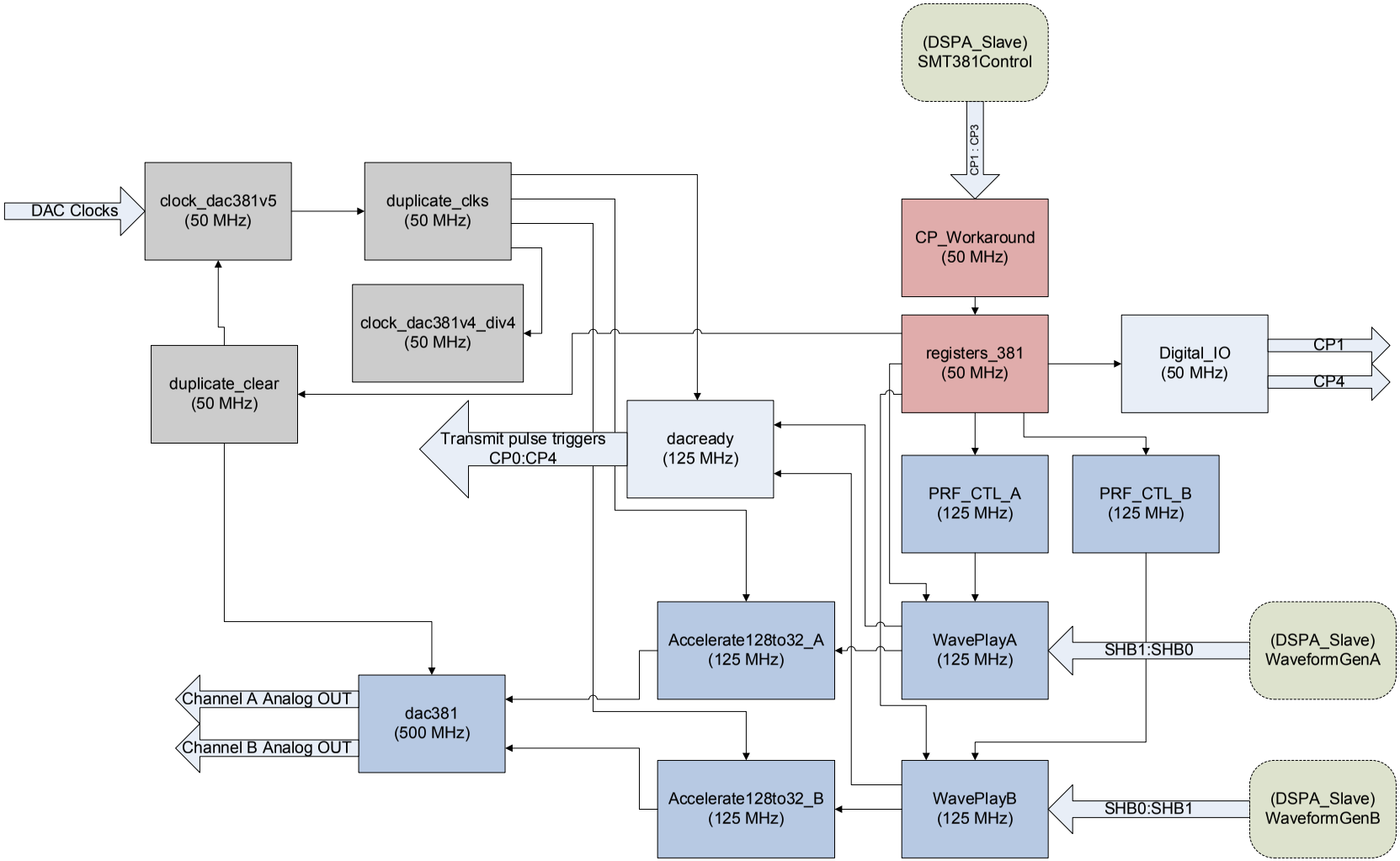

Figure 3.22: SMT368A transmitter FPGA block diagram of tasks.

task generates all the pulses to be coherently integrated with the appropriate pulse length and IPP. The *WavePlay* tasks then wait to be triggered again by the *PRF_CTL* tasks until the complete coherent pulse train has been generated. Since the FPGA's memory is not fast enough to be read from at the same rate as the 1 GHz DAC, samples of the transmitted waveform are actually stored in sets of eight samples in parallel. Each sample is stored as a 16-bit number (only the lower 14 bits are used for the 14-bit DAC) for a total of 128 bits in parallel. The *WavePlay* tasks read out eight samples at a time (one 128-bit number) and send them to the *Accelerate128to32 (A and B)* tasks where they are converted from 128 bits in parallel to four words in series, each containing 32 bits of data, or two samples in parallel. These 32-bit words, or two parallel samples, are written to the DAC by the *dac381* task at a rate of 500 MHz. In this manner, real-valued waveform samples are transferred to the DAC at a rate of 1 GSPS.

At the beginning of every transmitted pulse, the *WavePlay (A and B)* tasks generate a control signal which is forwarded to the *dacready* task. The *dacready* task outputs these control signals using some I/O pins which, using an FMS cable, are connected to I/O pins on the receiver FPGA. In this manner, the transmitter FPGA is able to trigger the receiver FPGA whenever a pulse is transmitted to maintain synchronization. Other tasks, denoted in gray, utilize a digital clock provided by the DAC to generate global clocks used throughout the FPGA.

Receiver FPGA

The operations which take place in the SMT368 receiver FPGA are relatively more complex than the those in the transmitter FPGA. While the transmitter FPGA is only responsible for generating a finely timed coherent pulse train, the receiver

FPGA is responsible for recording range samples when triggered, coherently integrating complete range returns, and performing quadrature demodulation on the samples before transferring them to tasks on the DSPs for further processing. Similarly to the transmitter FPGA, the high data rate of the 1 GSPS ADC necessitates the parallelization of these tasks. The quadrature demodulation process will be discussed first, followed by a high level overview how this process can be implemented in parallel along with coherent integration. Finally, a task level block diagram of the complete receiver FPGA implementation will be shown.

The SDR RF hardware is designed such that the analog input to the ADC is restricted to the frequency range of 0 to 500 MHz. The ADC creates real-valued samples of this analog signal at a rate of 1 GSPS for each channel. Quadrature demodulation, as outlined in [37] is a method to convert this real-valued signal to a complex-valued signal with half the sample rate. The complex-valued signal has a non-symmetric Fourier transform and provides both amplitude and phase information. The demodulation process involves mixing the incoming real-valued signal with a sine and cosine whose frequency is one fourth that of the sampling frequency, as illustrated in Fig. 3.23. Here, this frequency is 250 MHz. After the mixing operation, the signals are sent through low pass filters whose cutoff frequencies are 250 MHz. These filters remove the high frequency components which have been introduced by the mixing operation. Since the complex-valued signal is now band-limited to ± 250 MHz instead of ± 500 MHz, it is appropriate to decimate the signals by a factor of two. It should be noted that no information has been lost since both the positive and negative frequencies of the complex-valued signal contain information, whereas the negative frequencies for the real-valued signal contribute no additional information.

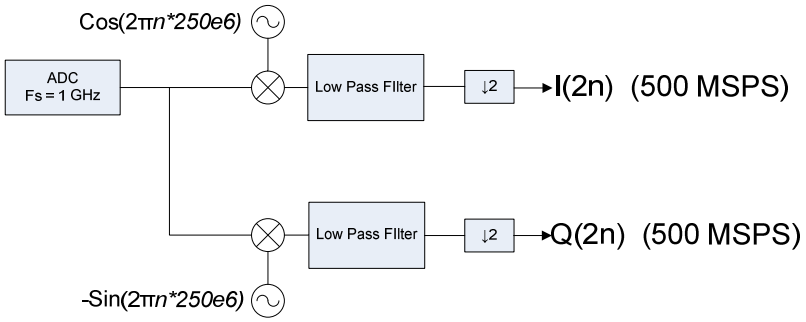

Figure 3.23: Quadrature demodulation operation resulting in complex samples of the real-valued waveform.

An important simplification arises in quadrature demodulation when the demodulation rate is chosen to be one fourth of the sample rate. That is, the values of the sine and cosine signals used for mixing simplify to the series [0 1 0 -1 0 1 ...] and [1 0 -1 0 1 0 ...] respectively. As shown in [37], the decimation operation can be performed before the mixing and filtering operations, simplifying the mixing operations even further to multiplications by the series [1 -1 1 -1 ...]. Downsampled versions of the low pass filters are also required, decreasing the amount of resources required to implement these filters in the FPGA.

Fig. 3.24 illustrates how the quadrature demodulation operation can be parallelized in combination with coherent integration. Only one channel is shown in the figure. Similar to how the DAC receives two digital waveform samples in parallel at a clock rate of 500 MHz for an effective rate of 1 GSPS, the ADC transfers four 8-bit samples in parallel to the receiver FPGA at 250 MHz for an effective rate of 1 GSPS. The analog input to the ADC ranges from -0.25V to 0.25V, which is mapped to the 8-bit codes 0 to 255. These parallel samples are labeled 1, 2, 3, and 4 in the figure according to their order in time, 1 being the earliest sample. It is desirable for

further processing to represent the digital signal in signed two's complement format, so a simple unsigned-to-signed conversion is used. This conversion is illustrated in Fig. 3.25 and involves negating the most significant bit of every sample.

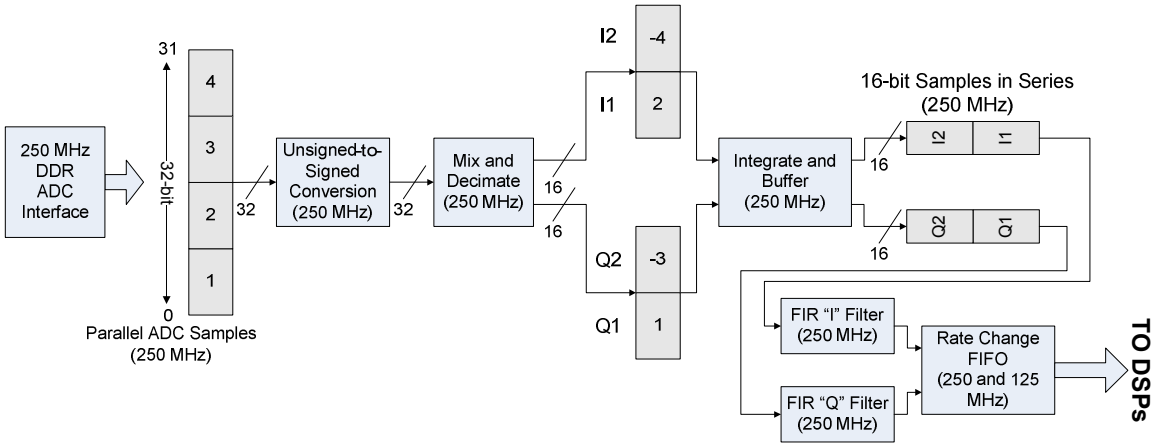

Figure 3.24: Implementation of the quadrature demodulation and coherent integration operations on four samples in parallel.

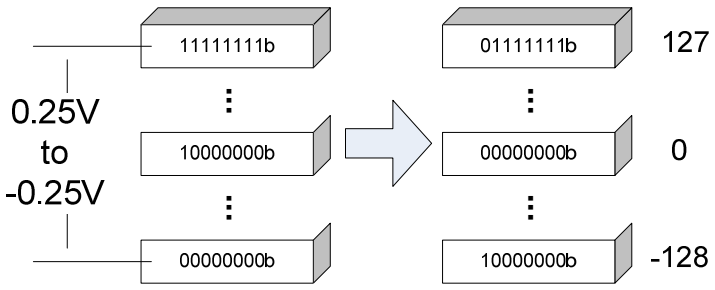

Figure 3.25: Unsigned to signed conversion of ADC data is achieved by negating the most significant bit.

Next, the mixing and decimation operation is performed. In this simplified version, this is achieved by splitting the parallel samples into two sets, one for I and one for Q, and multiplying every other sample by -1 as illustrated in the figure. Up to this point, all of the operations have been performed on the four consecutive samples in parallel at full speed (250 MHz), and no information has been lost. When triggered by the transmit FPGA, the signed, mixed, and decimated signals are recorded into memory for the required number of range samples for coherent integration. If no coherent integration is requested by the user, this data is played out of the memory in series, as shown, through the appropriately downsampled I and Q low pass filters. It is buffered in a first-in first-out memory (FIFO) from which it is eventually read by the *GetSamples* task in the DSPs. However, if coherent integration is requested, the data is read out of the memories and added sample by sample to the incoming range return when triggered again by the transmitter FPGA, with the result being written back into memory. This process continues for each pulse return to be coherently integrated. On the last coherently intregrated pulse return, the final result is read out of memory in series through the low pass filters. To prevent numerical overflow when integrating pulse returns, the width of the data is expanded from 8 to 16 bits for each I and Q sample. This provides sufficient overhead for the integration of up to 255 range returns.

The complete diagram of all tasks in the receiver FPGA is given in Fig. 3.26. The *Smt391Control* task in the DSPs writes parameters to the *registers_391_368* task in the FPGA which control how many range samples are recorded for each range return and how many returns should be coherently integrated. The *adc_391_368* task implements the physical interface to the ADC and receives two sets of 4 samples in

parallel at 250MHz, one set for each channel, A and B. The remaining tasks in blue implement the functions discussed previously, namely unsigned to signed conversion, mixing and decimation, integration and buffering, and finally filtering. The final *RateChange (A and B)* task implements the FIFO which the DSPs read from over the high speed SHB connections. The syncdatapath task senses trigger inputs from the transmitter FPGA and forwards them to the *IntegrateBuffer (A and B)* tasks, thereby maintaining synchronization and coherence between the transmit and receive operations.

3.4 Selection of Core Operating Parameters

Selection of the core operating parameters of the SDR is a complex process which often involves trading off performance in one area for performance in another. Therefore, it is difficult to outline a basic procedure for selecting these parameters for any given situation. However, the ease with which the SDR's operating parameters can be tuned allows the user to iteratively select those which best accomplish a given task. A rule of thumb is to start by selecting the center frequency of operation and the effective slower PRF such that the PRF is at least twice the maximum expected doppler velocity. Often, the center frequency of operation is determined by the frequency-dependent scattering behavior of a target of interest. For slow-moving targets such as people walking, a low PRF on the order of 500 Hz to 1 KHz is desirable . Next, the length of the pulse should be selected along with the IPP. For many applications, a 1 microsecond pulse and an IPP of 5 microseconds is sufficient, yielding a fast PRF of 166 KHz. The maximum number of coherent integrations which can be performed is limited by the slow and fast PRFs already selected. However, a value in the range

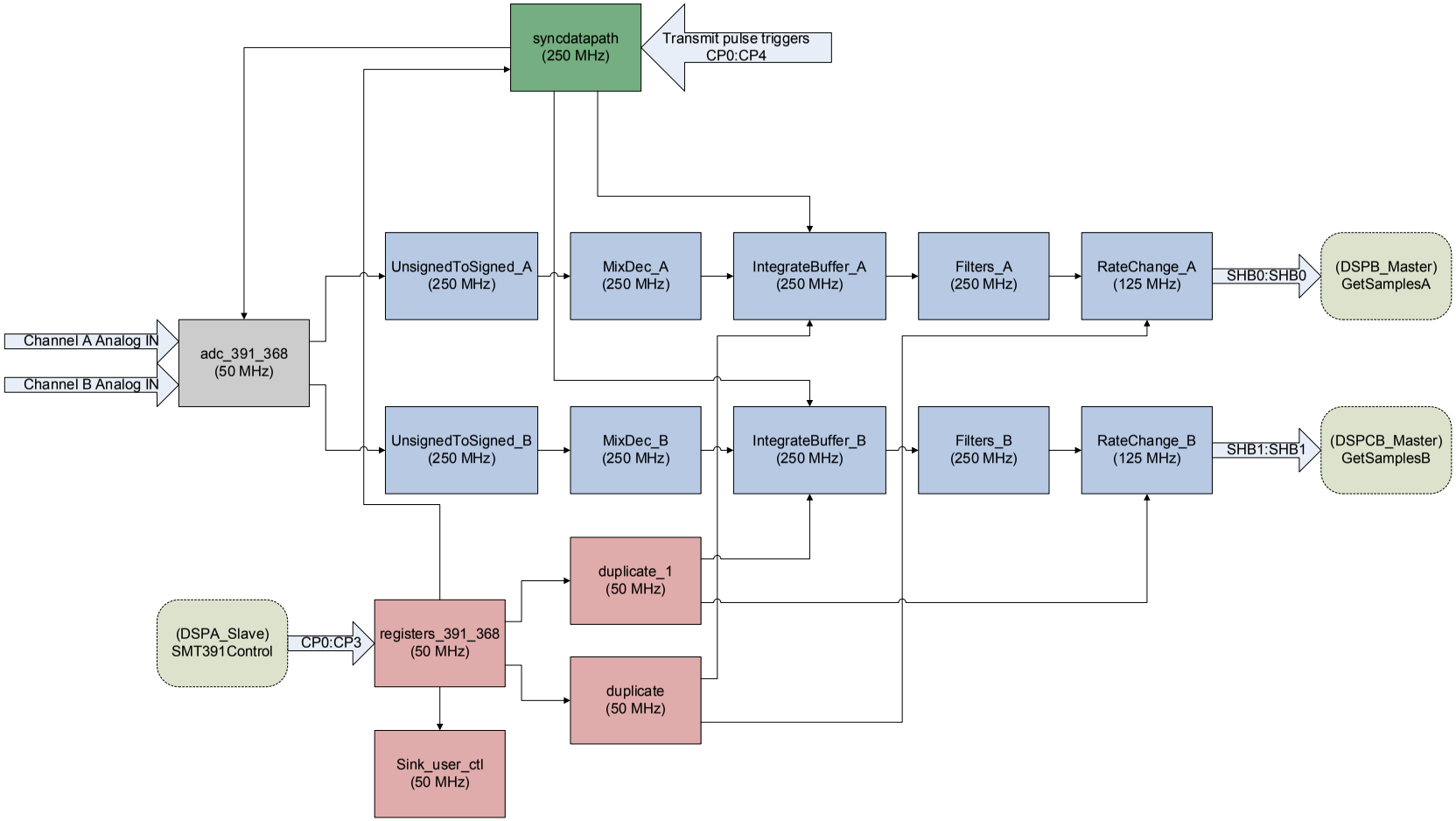

Figure 3.26: SMT368 receiver FPGA block diagram of tasks.

of 16 to 32 integrations typically yields acceptable results. Again, it should be noted that all of these parameters are easily tunable, and it is often necessarily to iteratively optimize the selected values for a given measurement task.

3.5 Summary

This chapter has outline the hardware and software required to implement the SDR, a flexible radar platform which enables researchers to explore new radar techniques. As was shown, the SDR is based on a power digital transceiver which is capable of generating, receiving, and processing signals with bandwidths up to 500 MHz in real time. Designed with flexibility in mind, the SDR with its low power, fully tunable RF front end and digital signal processing has many research applications, as will be demonstrated in the coming chapters. The performance of the SDR must first be verified, however, and various system tests are discussed in the next chapter.

CHAPTER 4

RADAR TESTING AND VALIDATION

This chapter will address testing and validation of the SDR conducted during various stages of its development. Issues addressed here include:

- ADC testing
- Waveform generation using the DAC
- Coherent integration and matched filter testing in a static environment
- Verification of Doppler processing using moving targets
- Loopback testing in the RF up/downconverter sections and mitigation of leakage between the RF transmitter and receiver sections
- Monostatic sphere calibration tests
- Demonstration of adaptive sensing of a moving target

4.1 ADC Testing and Waveform Generation Using the DAC

The ADC module in the SDR digital baseband transceiver operates at 1 GSPS to effectively sample 500 MHz of instantaneous bandwidth. Typically, higher sample

clock rates correspond to a smaller spurious-free dynamic range (SFDR). The SFDR is the ratio of the power in a single tone to the power in the largest spurious signal in the sampled data, and the maximum possible SFDR in dB is a function of the number of bits in the converter, B.

$$SFDR_{dB} = 6.02B + 1.76 \tag{4.1}$$

For an 8-bit ADC as is utilized in the SDR, the maximum SFDR is approximately 50 dB. However, the SFDR is typically less than the theoretical maximum and is a function of the analog input power and frequency of the tone.

The SFDR of the ADC module was experimentally measured by applying a single frequency tone directly to the analog input of one channel of the ADC and capturing 2048 consecutive samples. A Blackman window was applied to these samples to minimize sidelobes in the frequency domain, and a Fourier transform was taken. This process was repeated for two different input frequencies (200 MHz and 430 MHz), and the time-domain samples before windowing are shown in Figs. 4.1(a) and 4.1(c). The full-scale input to the ADC corresponds to codes -127 to 127. The corresponding Fourier transforms are given in Figs. 4.1(b) and 4.1(d) and have been normalized such that the largest signal is 0 dB. Only the results for one channel are shown here, as the results for the second channel are similar.

The largest spurious signal in the frequency domain is labeled in each plot. In the 200 MHz case, the second largest signal is the second harmonic of the input signal at 400 MHz. The presence of this signal is expected, so the largest spurious signal is also labeled and is of more interest. For the two input tones tested, the SFDR is 46.4 dB and 42.6 dB respectively, less than the theoretical 50 dB limit for an 8-bit ADC. We can substitute these numbers into (4.1) and solve for B which is then referred

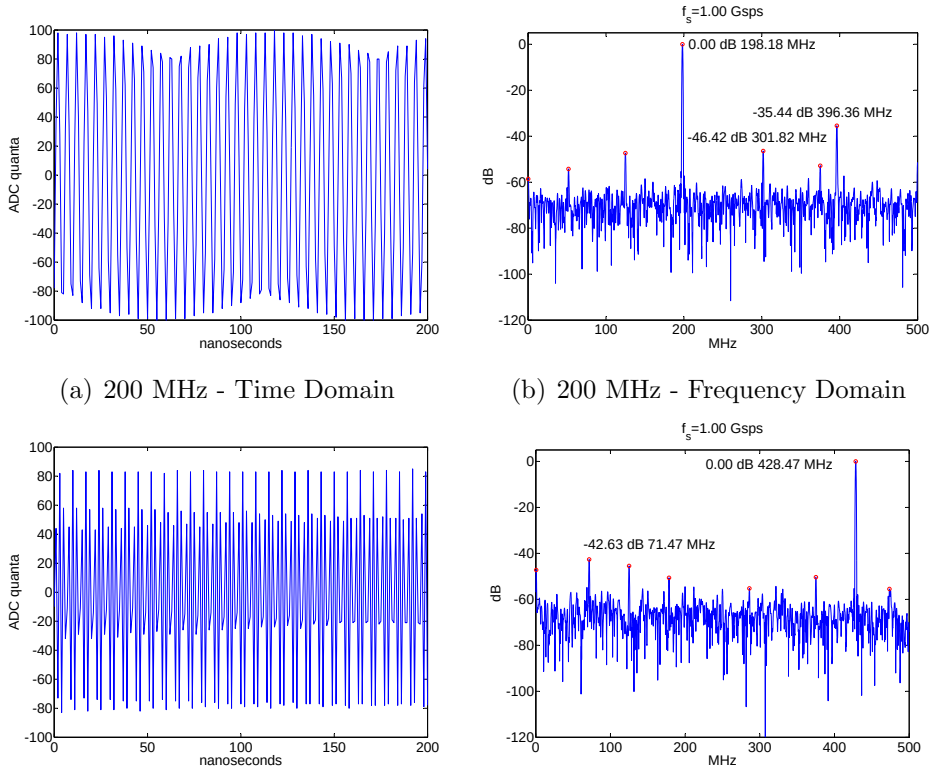

(a) 200 MHz - Time Domain

(b) 200 MHz - Frequency Domain

(c) 430 MHz - Time Domain

(d) 430 MHz - Frequency Domain

Figure 4.1: ADC captures of length 2048 samples for single input tones of various frequencies. The data is shown in both the time and frequency domains. The magnitude in dB of largest spur is labeled in the frequency domain.

to as an *effective* number of bits (ENOB). For the two input frequencies measured, the ENOB is 7.4 and 6.8. This agrees well with the ADC datasheet which quotes 6.8 ENOB [38].

Next, the ability to generate pulses using the DAC was tested. The transmitted test pulse is an upward chirping linear frequency modulated (LFM) waveform which is described in more detail in Appendix B.3. The pulse is 1 microsecond long and linearly sweeps from 10 MHz to 500 MHz over the pulse duration. Samples of the chirp are generated in the DSPs, transferred to the transmitter FPGA, and played back in a pulse train as described in Chapter 3. The output of a single channel of the DAC was connected to an oscilloscope to record time-domain samples of the pulse. Fig. 4.2(a) shows the complete captured pulse, while Fig. 4.2(b) shows only the beginning of the waveform to better illustrate the linearly increasing frequency within the pulse.

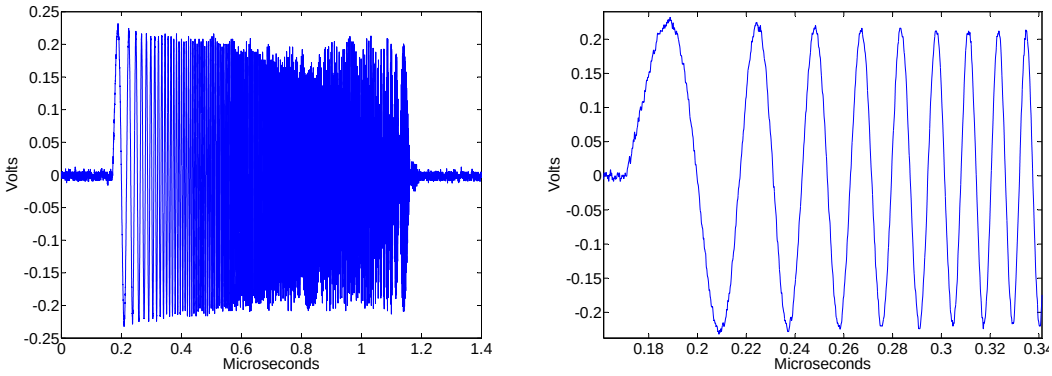

(a) 1 Microsecond Chirp

(b) Zoomed Start of Chirp

Figure 4.2: Samples of a LFM waveform generated with the DAC and captured with an oscilloscope. The pulse chirps from 10 MHz up to 500 MHz in 1 microsecond.

The single pulse is part of a coherent pulse train with both a fast and slow PRF as illustrated previously in Fig. 3.1. The SDR was configured using the GUI to coherently integrate four pulses at a time and to operate with a slow PRF of 10 KHz and a fast PRF of 167 KHz. The oscilloscope was again connected to the output of the DAC, but this time was set to capture a larger time span to illustrate the formation of the coherent pulse train. A portion of that pulse train is shown in Fig. 4.3. Three groups of four pulses each are shown in the figure. Each pulse to be coherently integrated is separated by 6 microseconds corresponding to the fast PRF, while start of each group of pulses is separated by 100 microseconds corresponding to the slow PRF. Furthermore, because the formation of the pulses is finely controlled by the transmit FPGA, the pulses and timing are precise and identical every time.

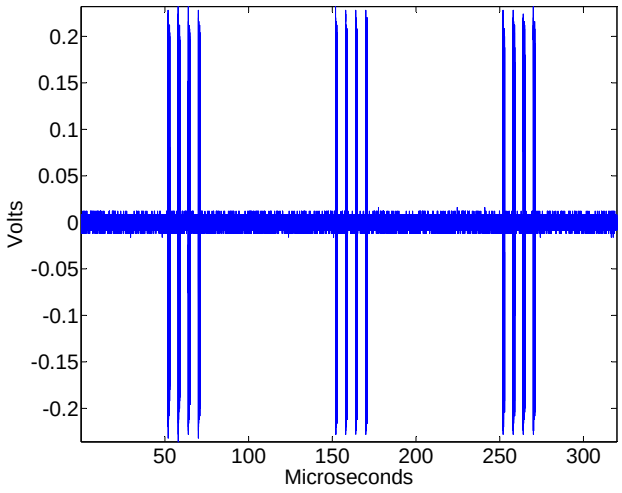

Figure 4.3: Oscilloscope capture of a portion of a transmitted pulse train with an overall PRF of 10 KHz, and a fast PRF of 167 KHz. The SDR was configured to perform four integrations. The separation between each pulse to be integrated is 6 microseconds, while the separation between each set of pulses is 100 microseconds.

4.2 Verification of Matched Filter and Doppler Processing

To test the SDR digital baseband transceiver before the RF portion of the system was complete, a temporary C-band prototype front end was constructed with a 6 GHz center frequency and 450 MHz of bandwidth. This simple front end was used to conduct two separate experiments. The first experiment tested the matched filtering operation in a static environment, while the second experiment tested the doppler processing with a moving target.

The first experiment consisted of a simple measurement of a corner reflector placed in a field at three different ranges (45.4 m, 34.7 m, and 28.3 m) from a monostatic pair of antennas. The radar was set to transmit a 500 MHz linear FM chirp which was limited to 450 MHz by the analog filter in the front end. The chirp had a pulse length of 800 ns, and 128 range returns were coherently integrated. Matched filtering was performed in the digital transceiver and the results were recorded. The pulse-compressed range profiles are shown in Fig. 4.4. The results show a range resolution of approximately a third of a meter which is consistent with the bandwidth of the system. As predicted by the radar range equation [26], the received power falls off as $1/R^4$. The targets present at the at shorter ranges are reflections from real objects which could not be moved for the experiment.

A second experiment was performed using a moving target in a parking lot. The target in this case was a Chevrolet S-10 pickup truck with a total length of approximately 4 m. The SDR was configured to use the same 500 MHz linear FM chirp as in the first experiment. The pulse length was 800 ns and 90 coherent integrations were performed. 128 total pulses were recorded with a PRF of 1.5 KHz. A range-doppler image was formed from these measurements and is shown in Fig. 4.5. Since the radar

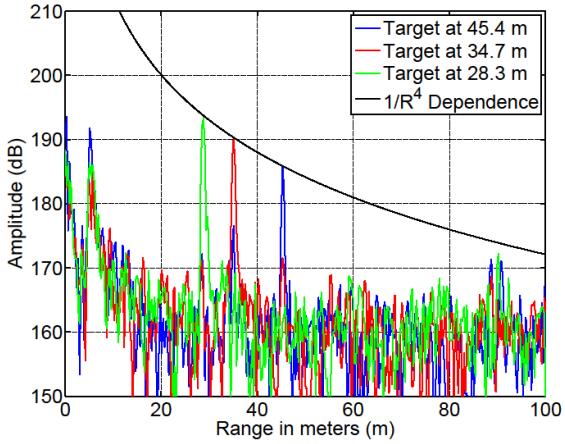

Figure 4.4: Three range profiles with a corner reflector located a three different ranges. Received power falls off at a rate of $1/R^4$, consistent with the radar range equation. The magnitude of the responses are uncalibrated.

was stationary when the measurement was made, other stationary targets such as parked cars and other clutter appear in a vertical line with zero velocity (center). The truck, moving away from the radar at approximately 8 m/s, appears as a distinct target with negative velocity (left of center). The truck also appears as a small target with a positive velocity (right of center), which is primarily due to inadequate image rejection in the prototype RF front end.

The previous two experiments demonstrate the basic functionality of the SDR digital baseband transceiver. The static tests show qualitatively that the radar can coherently integrate pulses, perform quadrature demodulation, and correctly match filter the incoming range returns. Furthermore, the moving target test shows that the doppler processing is being performed correctly. The target is distinctly separated from stationary clutter and appears with the proper doppler shift according to (3.1).

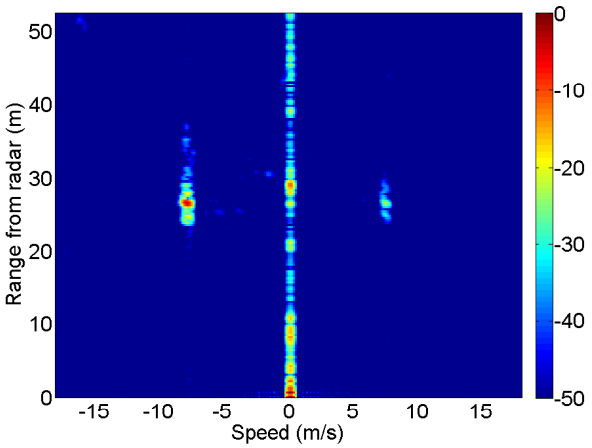

Figure 4.5: Range-Doppler map of a small pickup truck moving away from the radar at approximately 8 m/s. The x-axis represents velocity, with positive numbers indicating closing velocities and negative numbers indicating opening velocities. The y-axis indicates range from the radar.

4.3 Loopback and Leakage Mitigation in the RF Front End

The SDR's tunable RF front end consists of two independent transmit and receive channels, each of which contains three possible RF paths: a direct conversion path which bypasses the second mixing stage (2-2.5 GHz), the path through the discrete bank of filters (2.5-6 GHz), and the path through the tunable YIG filter (6-18 GHz). It is often desirable to connect the transmitters directly to the receivers using the loopback connections provided by the four directional couplers in Fig. 3.6. This is accomplished using a short length of cable and a 30 dB attenuator for each pair of loopback connectors in Fig. 3.12. However, it was found that the power variation through this loopback path as the center frequency of the radar was tuned from 2.5 to 18 GHz was actually larger than the dynamic range of the ADC causing the ADC

to saturate at the lowest frequencies. The tunable YIG filter has more loss than the switched filterbank, and it was found that the loopback path did not saturate at the lowest 6 GHz center frequency. Therefore, it was decided that it was necessary to place additional 10 dB attenuators directly before switched filterbank in the two transmit channels such that the loopback power at the lowest filterbank frequency (2.5 GHz) was less than the loopback power at the lowest tunable YIG frequency (6 GHz). This guarantees that the loopback power will not saturate the ADC.

Even when the loopback path and antenna modules are disconnected, some leakage occurs between the RF up- and downconverter sections. Because the SDR has 500 MHz of bandwidth, it can distinguish the arrival of different signals in time which are separated by only a few nanoseconds. This feature was used to help isolate the location of the source of the leakage signal within the system in real-time by disconnecting components one by one in the system starting with those closest to the antennas and working back towards the baseband transceivers until the leakage component disappeared. In this manner, it was found that the largest leakage path was the tunable LO distribution network. The RF signal coming from port A of the first IF switch in the transmitter in Fig. 3.4(a) would leak from the IF to the LO port of the mixer, across the output ports of the power divider in Fig. 3.5, and then into the receiver by leaking from the LO to IF ports of the corresponding mixer in Fig. 3.4(b). This leakage was mitigated by decreasing the amount of attenuation before the amplifier preceding the power divider in Fig. 3.5 and placing a 5 dB attenuator on the output of each port of the power divider. Since the leakage path actually passes through two of these attenuators, its power was decreased by an additional 10 dB. This attenuation

is adequate to decrease the magnitude of the internal leakage path to a level which is sufficiently lower than that provided by the external loopback path.

4.4 Monostatic Sphere Calibration Testing

Once the fully tunable RF front end was complete and integrated with the digital baseband transceiver, a monostatic calibration measurement was performed in the ElectroScience Laboratory's anechoic chamber. A pair of transmit and receive antenna assemblies was set up in a monostatic configuration approximately 6 m from the center of the anechoic chamber. The SDR was configured to transmit 1 microsecond pulses with a PRF of 1 KHz. Both transmit channels were configured to use LFM waveforms with 500 MHz of bandwidth and to coherently integrate 32 pulses.

First, a metal sphere with a diameter of 3.185" was placed on a foam column at the center for the anechoic chamber. Using the antenna switch matrix, the vertical elements of the monostatic pair of antenna assemblies were connected to transmit and receive channel A. The range return including the sphere was measured for varying center frequencies stepping from 6 to 18 GHz in 1 GHz increments, effectively covering those frequencies which utilize the tunable YIG filter in the RF front end. The antenna switch matrix was then reconfigured to connect the vertical antenna elements to channel B, and the measurement was repeated. This whole procedure was performed a second time for a metal sphere with a diameter of 6", and finally a third time with no sphere present referred to as the background measurement.

For each frequency and channel, the corresponding background measurement was coherently subtracted from the two sphere measurements to remove some environmental effects. The response of the larger 6" sphere was then compared to the analytical

solution for the scattered fields from a perfect electrically conducting (PEC) sphere of the same diameter, and a set of calibration coefficients were calculated. The calibration coefficients were applied to the measured response of the smaller 3.185" sphere. This process is described in greater detail later in Section 5.1.

The calibrated RCS in dBsm (dB square meters) for the 3.185" diameter sphere versus center frequency is given in Fig. 4.6. Fig. 4.6(a) shows the results for transmitter and receiver A, while Fig. 4.6(b) shows the results for transmitter and receiver B. The red markers denote the calibrated measured RCS of the 3.185" diameter sphere, while the solid blue curve in the figures is the analytic solution for scattering from a PEC sphere of the same diameter.

It is difficult to separate the small radar return of the 3.185" sphere from the clutter without background subtraction even though the measurement was performed in an anechoic chamber designed to minimize clutter. Even with background subtraction, the resulting SNR of the measurement is less than desirable. This is in part due to the fact that the background measurement and sphere measurements were separated in time by over an hour. This decreases the ability to coherently subtract the background which introduces errors in both the sphere measurement used for calibration and the sphere measurement to be calibrated. In addition, the antenna assemblies were connected to the SDR using long cables whose loss increases monotonically with the center frequency, thereby decreasing the SNR further as the frequency increases. However, after subtracting the background measurement from both the 3.185" and 6" diameter sphere responses, the calibration can be performed adequately.

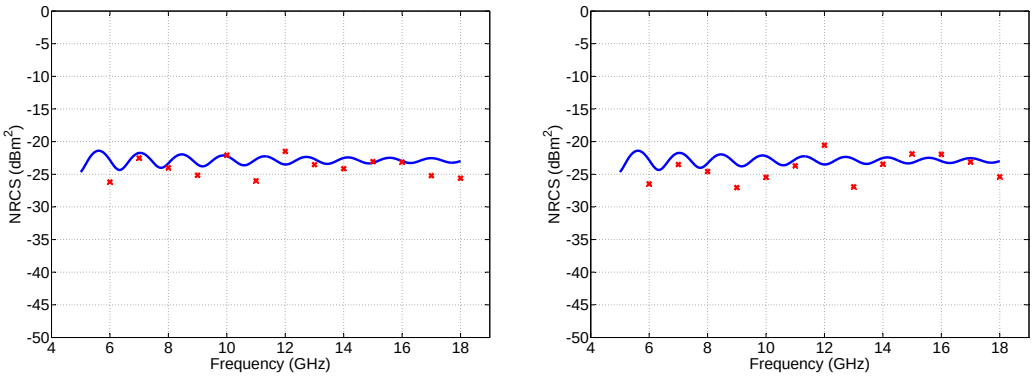

(a) Channel A (b) Channel B

Figure 4.6: Calibrated RCS (dBsm) for a sphere of diameter 3.185" versus center frequency. The solid blue curve is the theoretical response for the sphere.

4.5 Adaptive PRF Demonstration

An important feature of the SDR is its inherent reconfigurability. The user has the ability to modify many of the radar's core operating parameters in real-time simply by changing settings on the GUI. This can be taken one step further by allowing the system to adapt itself automatically to achieve some sensing goal. A simple example of this is to allow the radar to automatically minimize the PRF to maximize the doppler resolution of a moving target while simultaneously ensuring that the PRF is high enough to prevent aliasing. For a fixed number of N range returns processed for doppler information, the size of a doppler bin in Hz (ΔB) is directly proportional to the PRF.

$$\Delta B = \frac{PRF}{N} \tag{4.2}$$

Therefore, to minimize the size of a doppler bin, the PRF must also be minimized. However, to sample the doppler shift of a moving target without aliasing, the PRF

must be at least twice the doppler shift defined in (3.1). Special code has been added to the GUI to perform this trade-off automatically, and the basic procedure is discussed here.

The following procedure assumes that only a single moving target is present in the scene and that the target is not initially aliased in doppler. This is accomplished by generating an initial range/doppler map using a high PRF. The largest point in the map which both exceeds a simple threshold and is at least two doppler bins away from the zero doppler bin is taken to be the target of interest. If the moving target is closer to the zero doppler bin than some minimum allowable doppler shift, then the PRF is decreased to increase the doppler resolution and further separate the target from the stationary clutter. However, if the target is located in a doppler bin which is greater than some maximum allowable doppler shift, then the PRF is increased to prevent aliasing.

A screenshot of the GUI during this process is shown in Fig. 4.7. Only transmit and receive channel A is utilized here with a single pair of vertically polarized antennas in a monostatic configuration. As was mentioned before, the zero-doppler returns fall along a horizontal center line in the range/doppler map. Additional constant-doppler lines corresponding to ± 75 Hz are also drawn on the map to help visualize how the doppler space changes with the PRF. The target is denoted by a purple square in the range/doppler map. Every time the target is detected, a status message is written to the GUI with its magnitude, doppler shift in Hz, and velocity in miles-per-hour (MPH) for the given center frequency of the radar. When the target is either too close to the zero doppler bin or too close to aliasing, a new PRF is automatically calculated which will place the target back within an acceptable doppler bin. A status message

is written to the GUI with the current PRF and the new adjusted PRF which will be used to form the next range/doppler map.

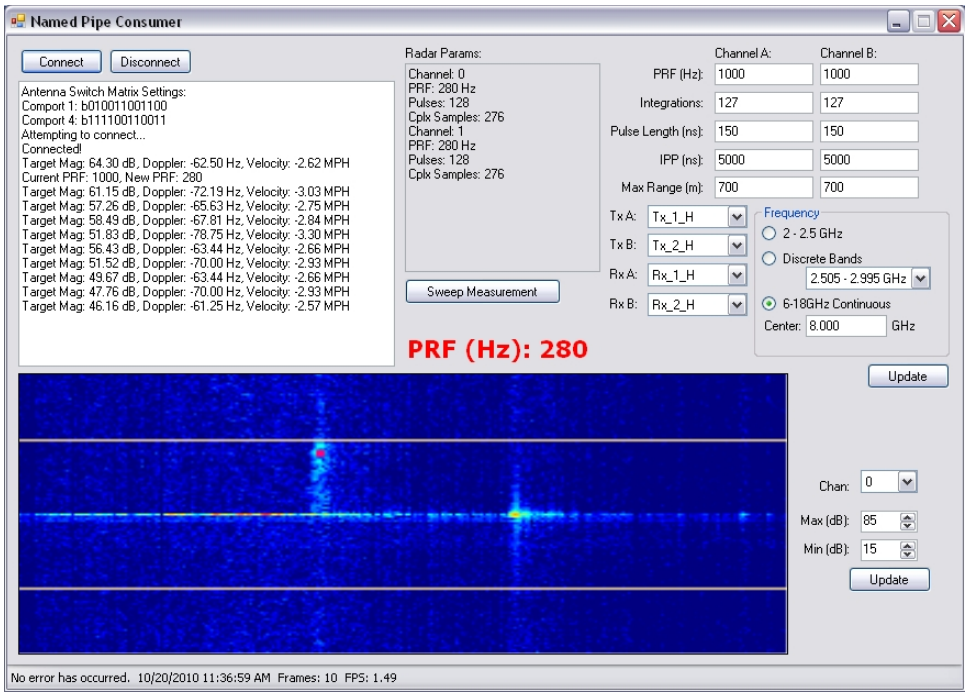

Figure 4.7: Screenshot of the GUI showing the radar actively adapting the PRF to maximize the doppler resolution of a target. The target is a purple square in the range/doppler map. The current PRF of the radar which is being actively adjusted in real-time is shown in red.

A simple test was performed in which a person standing close to the monostatic pair of antennas began walking away from the radar, accelerated to some maximum velocity and then decelerated to a complete stop before turning around. The person then accelerated and decelerated towards the radar, returning to the original starting location. The target was tracked throughout this process in range and doppler. The PRF was initially continually increased to prevent aliasing until the target reached

some maximum velocity. As the target decelerated, the PRF was continually decreased to maximize the doppler resolution. This process was then repeated as the target returned to its starting location, all without any user intervention.

The method presented here to automatically adjust the PRF needs to be expanded before it can be applied to a real-world sensing application. It has been assumed that only one target is present, the target is not already aliased, and that the PRF can be adjusted quickly enough to compensate for any acceleration or deceleration of the target. More complicated algorithms are needed to track multiple targets and potentially unwrap aliased targets. However, this simple demonstration illustrates the flexibility, functionality, and utility of the SDR.

CHAPTER 5

MIMO TARGET MODEL EXPERIMENTAL EVALUATION

Chapter 2 explored methods of modeling the fields scattered from a complex target observed with spatially diverse transmitters and receivers. The complex target was modeled as a finite rectangular region containing an infinite number of random scatterers. The expected value of the scattered fields for a large number of realizations of the target was used to calculate a covariance matrix. If the fields are zero-mean complex Gaussian random variables, then the covariance matrix is all that is needed to completely describe the average scattering behavior of the target.

The original target model presented by *Fishler et. al.* stated that the scattered fields have equal average power in all transmit/receive pairs as long as the transmit and receive antennas are sufficiently separated, and the scattered fields are uncorrelated with another. This results in a covariance matrix which is a scaled identity matrix. As alluded to previously, this is not representative of many classes of real-world targets that don't scatter equally in all directions. An enhanced target model which could be tuned to scatter more in the forward direction in particular was proposed in Section 2.1.2, and resulted in a covariance matrix that was no longer constant along the diagonal and had increased off-diagonal covariance coefficients. It is hoped

that this model might more accurately predict the scattering behavior of real world targets. However, to this point, no attempt has been made to fit either model to the scattered fields from a realistic target.

In an attempt to evaluate the accuracy of the models' ability to predict the scattering behavior of a realistic target, the SDR system was utilized to measure returns from a small unmanned aerial vehicle (UAV) in the ElectroScience Laboratory's anechoic chamber. $M = 2$ transmitter and $N = 4$ receiver antenna assemblies were utilized to form a spatially diverse MIMO array. The fields scattered from the UAV were measured as the target was rotated through 360° in azimuth. After calibration and processing, the measurements in azimuth can be potentially considered as independent trials of a complex target. An estimate of the covariance matrix can then be calculated from these independent trials to see if the correlated target model can be fitted to produce a similar covariance matrix. The probability of detection curves calculated using the measured and estimated covariance matrices can also be compared. The measurement setup and calibration is discussed in Section 5.1 followed by the experimental results in Section 5.2.

5.1 Measurement Setup and Calibration

The SDR system was placed in the anechoic chamber with two transmit and four receive assemblies placed about the available space so as to form a spatially diverse array. The vertically polarized elements are utilized in this experiment. A foam column mounted on a digitally-controlled motorized rotator table is located at the center of the anechoic chamber, and this was used to position the target and rotate it in azimuth as needed. Fig. 5.1 shows photographs of the antenna assemblies

directed toward the UAV mounted on the foam column. The UAV itself is a small airplane manufactured by *The MLB Company* with a wingspan of approximately six feet [39]. Dimensions and photographs of the UAV are given in Fig. 5.2. While the wings of the UAV are mostly lightweight wood and plastic, the fuselage is packed tightly with electronics, a camera on gimbals, antennas, a fuel tank, and an engine ensuring a diverse set of complex scattering centers. Fig. 5.3 shows the measured three-dimensional locations (in meters) of the transmitters and receivers, with the base of the foam column located at the origin with the coordinates summarized in Table 5.1. Table 5.2 lists the direct distance between pairs and round-trip distances from each transmitter to the target ending at the receiver.

Table 5.1: Target and antenna coordinates in meters. The base of the column on which to target is placed is the origin. The z-axis is measured vertically from the floor, and transmitter $m = 1$ defines the positive x-axis.

Antenna Element	Coordinates in meters (x, y, z)
Target	(0, 0, 2.39)
Transmitters (M = 2):	
$m = 1$	(5.35, 0, 1.47)
$m = 2$	(3.27, 4.07, 1.48)
Receivers (N = 4):	
$n = 1$	(1.10, -6.87, 1.48)
$n = 2$	(4.21, -1.63, 1.49)
$n = 3$	(4.85, 2.19, 1.45)
$n = 4$	(1.68, 4.95, 1.47)

The SDR system was configured to measure the scattered fields for all $MN = 8$ combinations of vertically polarized elements at two different center frequencies: 2.75 GHz and 4.51 GHz. These frequencies correspond to filterbanks #1 and #5 in

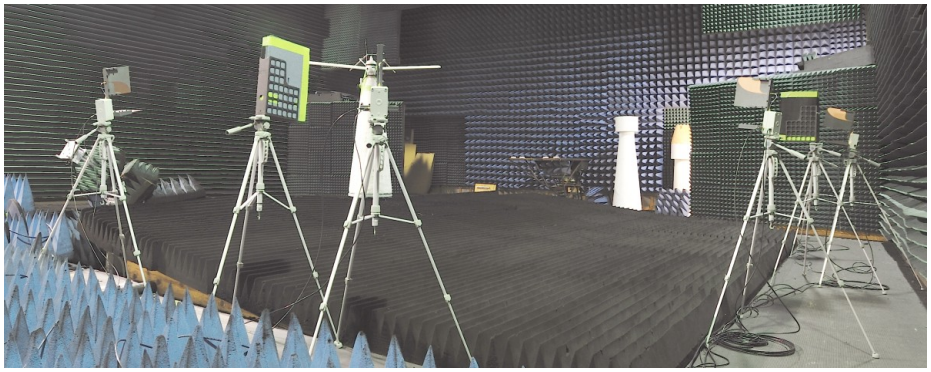

(a) Front View

(b) Side View

Figure 5.1: Photographs of the UAV mounted on the foam column with spatially diverse SDR transmit and receive antenna assemblies.

Table 5.2: Direct distance between elements and total round-trip distance to the target for each transmit/receive element pair.

Element Pair	Direct Distance	Total Distance
$m = 1$, $n = 1$	8.08 m	12.44 m
$m = 2$, $n = 1$	11.15 m	12.32 m
$m = 1$, $n = 2$	1.99 m	10.03 m
$m = 2$, $n = 2$	5.78 m	9.91 m
$m = 1$, $n = 3$	2.25 m	10.83 m
$m = 2$, $n = 3$	2.45 m	10.71 m
$m = 1$, $n = 4$	6.16 m	10.73 m
$m = 2$, $n = 4$	1.81 m	10.61 m

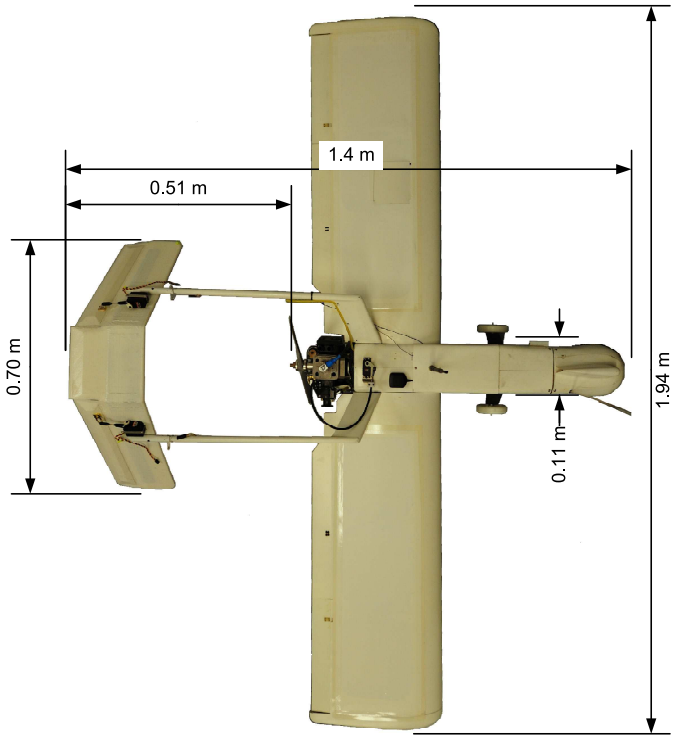

(a) Dimensions

(b) Front View

(c) Side View

(d) Back View

Figure 5.2: General dimensions and photographs of the UAV.

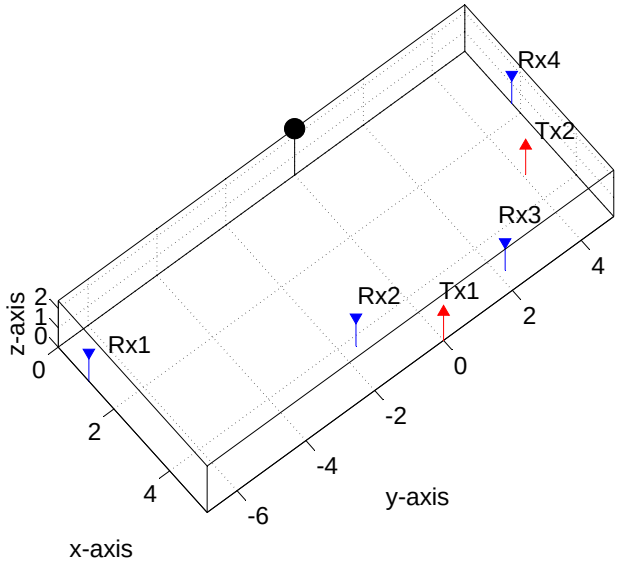

Figure 5.3: Locations in meters of transmit and receive elements with respect to the target.

the SDR (see Table 3.1). To accomplish this, an upward chirping linear frequency modulated (LFM) chirp waveform was assigned to transmitter channel A, connected to the vertically polarized element of transmit assembly 1. A downward chirping LFM waveform was assigned to transmitter channel B, connected to the vertically polarized element of transmit assembly 2. Both waveforms utilize 500 MHz of bandwidth and have a 1 microsecond pulse length. The maximum cross-correlation of these two waveforms is small, as illustrated in Appendix B.3.2 (Fig. B.11), allowing the waveforms to be separated by the matched filtering operation on receive. For each center frequency, both transmitters are active, but the two receive channels can only be connected to two of the four receive elements at a time. Therefore, the SDR first measured transmitter/receiver element combinations $1-1$, $1-2$, $2-1$, and $2-2$ with

the receiver channels connected to the first pair of receive elements. After switching the receive channels to the second pair of receive elements, the combinations $1-3$, $1-4$, $2-3$, and $2-4$ were measured. This process was repeated for both frequencies as the target was rotated every 0.25° in azimuth over 360°, for a total of 1440 azimuth measurements. Once this was complete, the UAV was removed from the column, and a measurement of the background was recorded for a single azimuth angle. Finally, a metal 6" sphere was placed on the column in the same location as the UAV's center of mass and was also measured for a single azimuth angle.

To remove environmental and non-target effects, the background measurement is coherently subtracted from the measurements of the UAV and the sphere. The resulting range returns for the UAV for a given azimuth angle and the sphere are denoted $r_{mn,t}[p]$ and $r_{mn,s}[p]$ respectively, where p is the discrete range sample index. Fig. 5.4 shows a sample uncalibrated return for one azimuth angle of the UAV, the background, and the coherent subtraction of the two for $m = 2, n = 4$, and $f_c = 2.75$ GHz. Both the target return and the large direct path term are evident in the figure. Coherent subtraction decreases the magnitude of the direct path return, but its magnitude is still on the same order as the target return even after subtraction. The MN measurements of the sphere are compared to analytical solutions of the scattered fields from the sphere to derive frequency dependent calibration coefficients $C_{mn}(\omega)$, where ω is the angular frequency in radians-per-second at baseband (corresponding to -250 to 250 MHz). The bandpass complex-valued scattered field of a perfectly conducting sphere is calculated using the Mie series to yield the bistatic response versus frequency for each vertically polarized pair of transmit and receive antennas, denoted $W_{mn}(\omega + 2\pi f_c)$ where f_c is the center frequency of the measurement [40]. A

simple multiplication by a complex exponential in the frequency domain shifts the sphere response to the proper location in range for each pair of antennas, resulting in $A_{mn}(\omega)$ defined as:

$$A_{mn}(\omega) = W_{mn}(\omega + 2\pi f_c)e^{-j\frac{(\omega+2\pi f_c)}{c}(|\overrightarrow{r_m}|+|\overrightarrow{r_n}|)} \tag{5.1}$$

The vectors $\overrightarrow{r_m}$ and $\overrightarrow{r_n}$ denote the measured physical distance and direction from the transmitter to the small sphere, and from the small sphere to the receiver respectively. The baseband calibration coefficients are then found according to

$$C_{mn}(\omega) = \frac{A_{mn}(\omega)}{R_{mn,s}(\omega)} \tag{5.2}$$

where $R_{mn,s}(\omega)$ is the DTFT of the background-subtracted range response of the small sphere. The fully calibrated response of the UAV is then found through simple multiplication of the DTFT of the measured range response ($R_{mn,t}(\omega)$) by the calibration coefficients, and then taking an the inverse DTFT:

$$f_{mn,t}[p] = DTFT^{-1}\left\{C_{mn}(\omega)R_{mn,t}(\omega)\right\} \tag{5.3}$$

Fig. 5.5 shows range response after the applying the calibration to the raw return in Fig. 5.4. The x-axis of the plot is the calibrated total round trip propagation distance from transmitter $m = 2$ to the UAV to receiver $n = 4$. The target is located at a range of approximately 11 meters which agrees well with the physical locations of the transmitters and receivers with respect to the target. A second large peak visible in the figure at a round trip distance of 1-2 m corresponds to the direct path from transmitter to receiver.

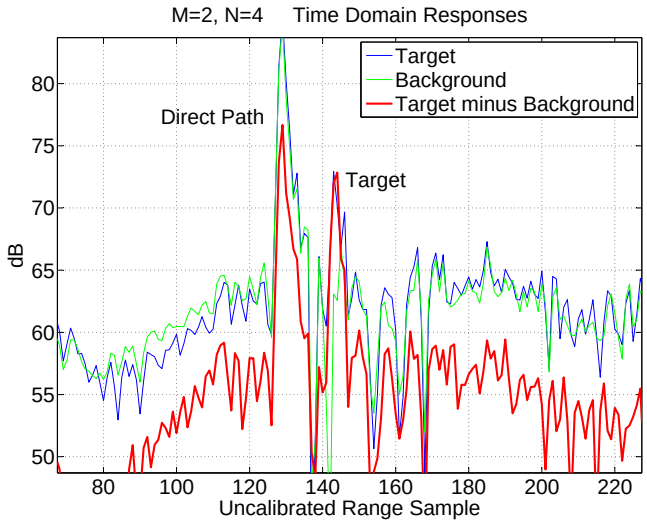

Figure 5.4: Uncalibrated time domain responses of the UAV, background, and result of subtracting the background from the UAV for a given azimuth angle and element pair $m = 2, n = 4$.

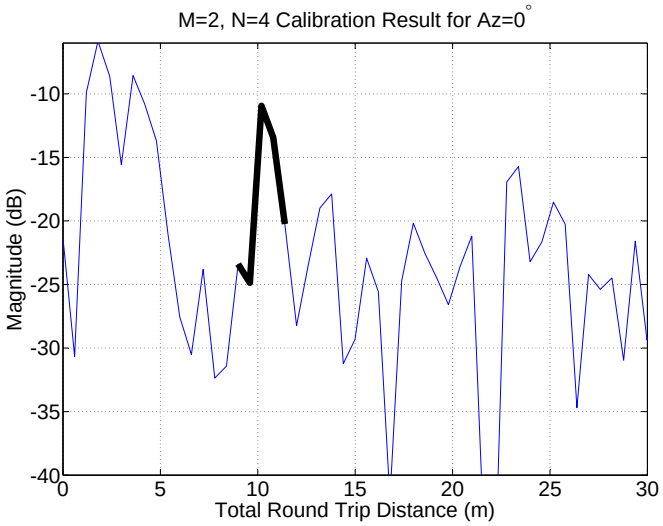

Figure 5.5: Example calibrated range response of the UAV for a given azimuth angle and element pair $m = 2, n = 4$. The target is assumed to occupy the extents illustrated by the dark line.

5.2 Processing and Results

The models in Chapter 2 assume that the return from the target is restricted to a single range bin. A single value α_{pq} was used to represent the scattered field measured by the p^{th} receiver resulting from the q^{th} transmitter for a given frequency. However, the downrange resolution of the SDR with 500 MHz of bandwidth and LFM chirp waveforms is approximately 1/3 m. Therefore, the UAV's 2 m fuselage could occupy up to six range bins depending on the azimuth angle. To measure one complex target return at the given center frequency, a time-domain window which is 7 samples long is applied to the calibrated range response of the target to gate out the range returns not directly attributable to the target. The target range returns that are left are shown as a dark black line in Fig. 5.5. A Fourier transform of the complete time-gated target response is then calculated to analyze the frequency-domain response of the target. For every azimuth angle measurement a, the frequency point in the Fourier domain corresponding to the center frequency of the measurement is recorded to represent the narrowband complex target response. In performing this procedure, it was found that the direct path could not be sufficiently removed by time-gating the target return for pairs of elements with large bistatic angles. Therefore, only the responses measured by receivers n =2, 3, and 4 will be analyzed further, limiting the system to $M = 2$, $N = 3$.

These measurements are "trials" of the scattered fields from the UAV, and can be written in the form $\zeta_{mn}[a]$. These trials are shown on polar plots in Figs. 5.6 and 5.7 for 2.75 and 4.51 GHz center frequencies respectively. The monostatic RCS of real complex targets such as airplanes have been known to vary by over 40 dB versus azimuth angle and up to 15 dB for changes in aspect as small as 1/3° [26]. However,

the total variation in the trials shown here is limited by the dynamic range of the SDR and is therefore approximately 37 dB at most, but is likely somewhat less. Table 5.3 lists the average RCS for each center frequency along with the corresponding bistatic scattering angle between transmitter and receiver.

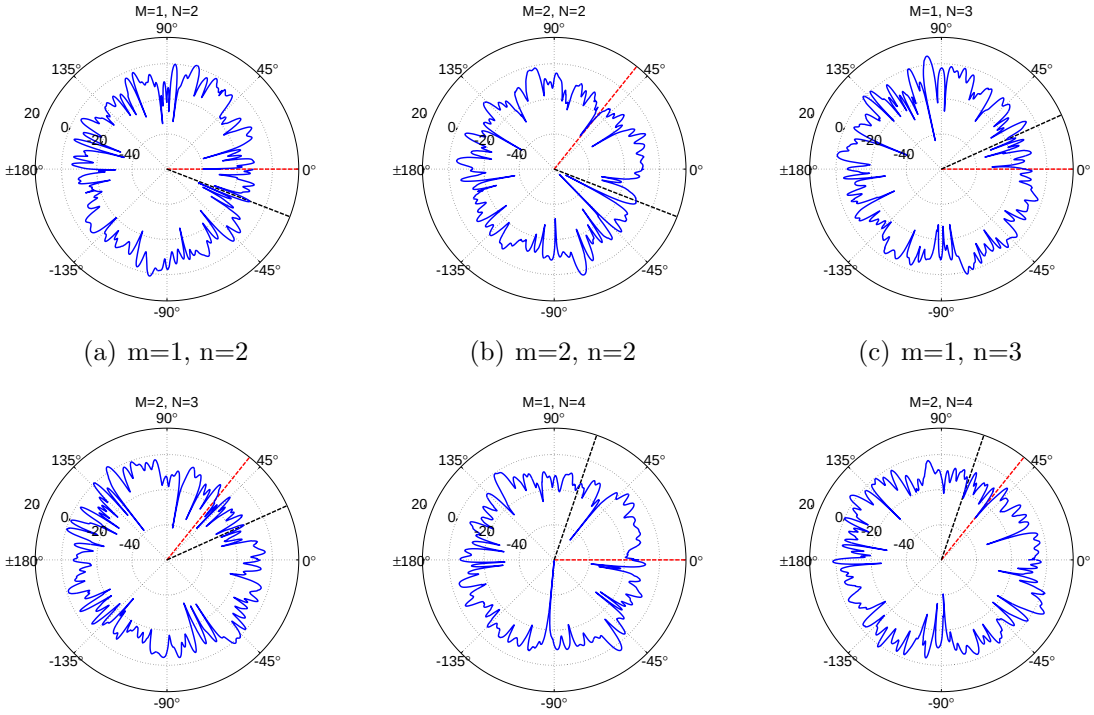

(a) m=1, n=2 (b) m=2, n=2 (c) m=1, n=3

(d) m=2, n=3 (e) m=1, n=4 (f) m=2, n=4

Figure 5.6: Measured and calibrated trials $\zeta_{mn}[a]$ in dBsm of the UAV for a 2.75 GHz center frequency.

5.2.1 Covariance Matrix Formulation

Through examination of the figures showing the magnitude of the trials versus azimuth, it is obvious that the trials for a given element pair are not entirely independent, as the magnitude of $\zeta_{mn}[a]$ varies smoothly over small ranges in angle.

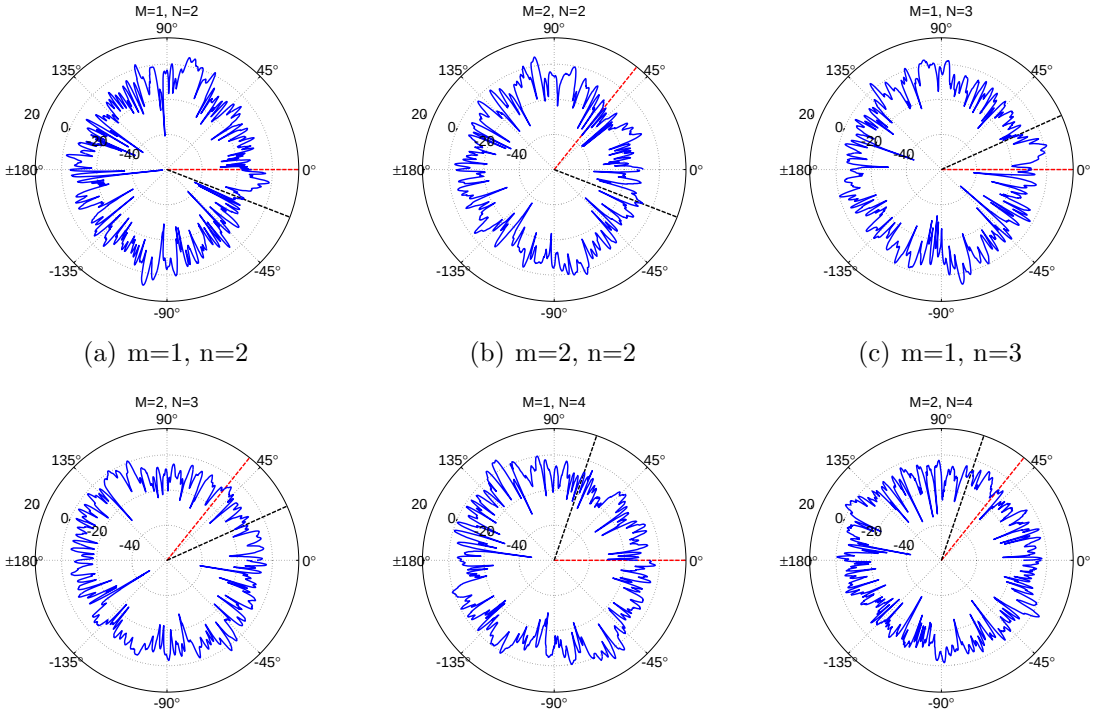

(a) m=1, n=2 (b) m=2, n=2 (c) m=1, n=3

(d) m=2, n=3 (e) m=1, n=4 (f) m=2, n=4

Figure 5.7: Measured and calibrated trials $\zeta_{mn}[a]$ in dBsm of the UAV for a 4.51 GHz center frequency.

Table 5.3: Bistatic angles and average RCS for each pair of transmit/receive elements, not including receiver $n = 1$.

Element. Pair	Bistatic Angle	Avg. RCS (2.75 GHz)	Avg. RCS (4.51 GHz)
$m = 1, n = 2$	20.4°	-8.06 dBsm	-6.54 dBsm
$m = 2, n = 2$	68.7°	-9.75 dBsm	-7.78 dBsm
$m = 1, n = 3$	23.4°	-6.36 dBsm	-5.91 dBsm
$m = 2, n = 3$	25.9°	-7.21 dBsm	-7.38 dBsm
$m = 1, n = 4$	68.2°	-8.82 dBsm	-4.97 dBsm
$m = 2, n = 4$	19.3°	-5.33 dBsm	-7.1 dBsm

Since the previously derived models assume independent realizations of the target, it is necessary to downsample $\zeta_{mn}[a]$ such that the trials which are left are sufficiently separated in angle, decreasing the correlation between them. Therefore, the trials vector $\zeta_{mn}[a]$ was downsampled by a factor of 12 resulting in $\zeta'_{mn}[d]$. The downsampled trials correspond to measurements in azimuth that are separated by 3°.

The independence of these trials can be verified by calculating their autocorrelations defined as $R_{mn}[k] = E\left\{\zeta'_{mn}[j+k]\ \zeta'^{*}_{mn}[j]\right\}/\sigma^2$ where σ^2 is the measured variance of $\zeta'_{mn}[d]$. The magnitudes of these autocorrelations are shown in Figs. 5.8 and 5.9 for f_c = 2.75 and 4.51 GHz respectively. Ideally, they should resemble a Kronecker delta if the samples are uncorrelated, and this is true to varying degrees.

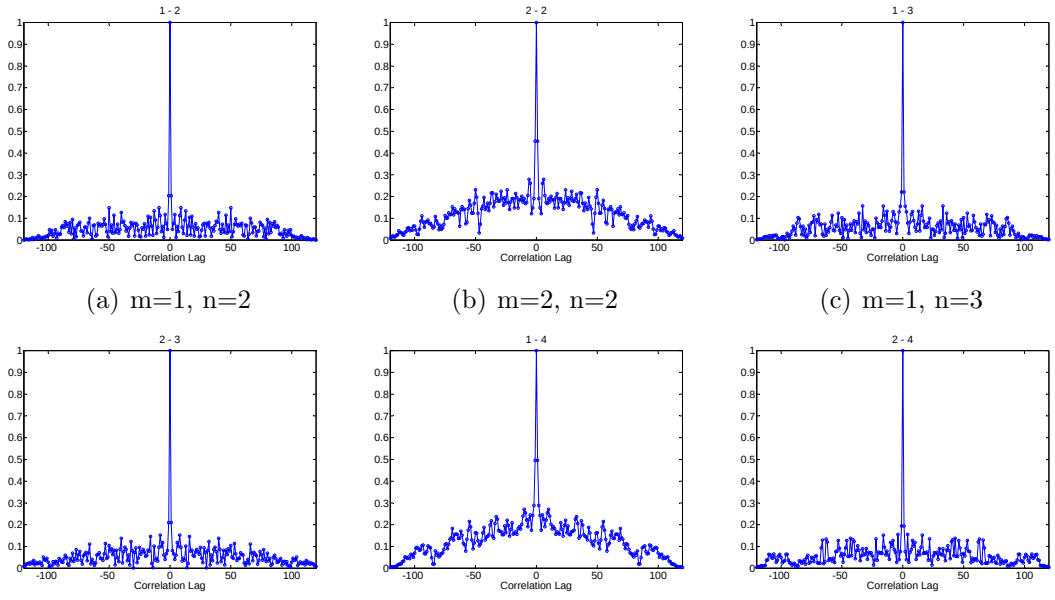

(a) m=1, n=2 (b) m=2, n=2 (c) m=1, n=3

(d) m=2, n=3 (e) m=1, n=4 (f) m=2, n=4

Figure 5.8: Autocorrelations of $\zeta'_{mn}[d]$ for $f_c = 2.75$ GHz.

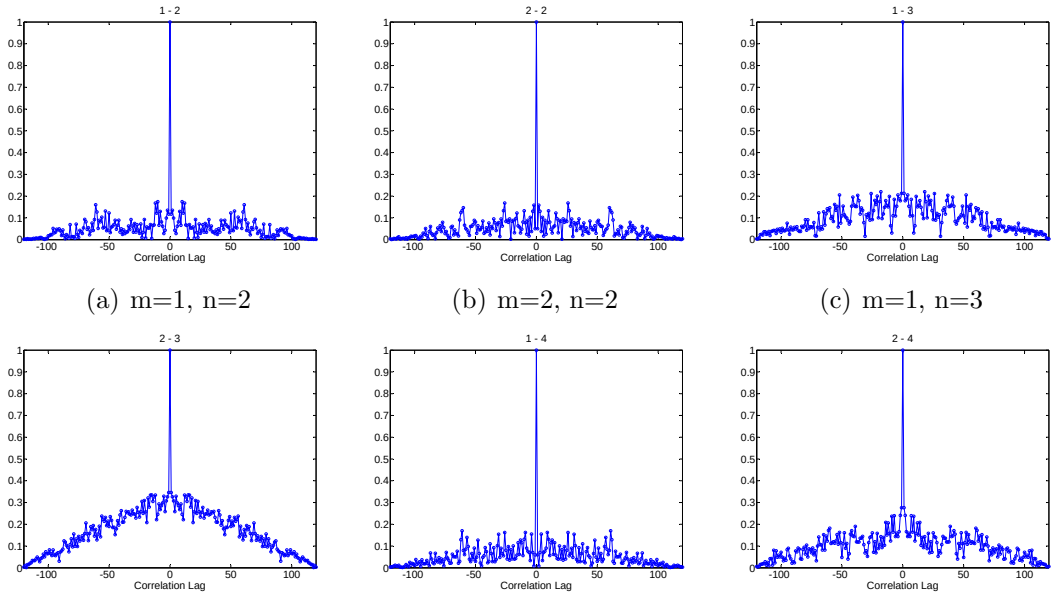

(a) m=1, n=2 (b) m=2, n=2 (c) m=1, n=3

(d) m=2, n=3 (e) m=1, n=4 (f) m=2, n=4

Figure 5.9: Autocorrelations of $\zeta'_{mn}[d]$ for $f_c = 4.51$ GHz.

An important assumption of both the uncorrelated and correlated scatterers models is that the complex amplitudes of the scattered fields from the target are drawn from zero-mean, complex Gaussian distributions. Histograms of the real and imaginary parts of $\zeta'_{mn}[d]$ were calculated and scaled appropriately to compare to the Gaussian PDF calculated from the sample means and variances. These are shown in Fig. 5.10 and Fig. 5.11 for the two different center frequencies. It is difficult to judge whether the fields are drawn from a Gaussian distribution given only 121 measurements, but an argument can be made that the fields are indeed zero-mean Gaussian. This implies that the covariance matrix estimated from these fields is all that is required to statistically describe them completely.

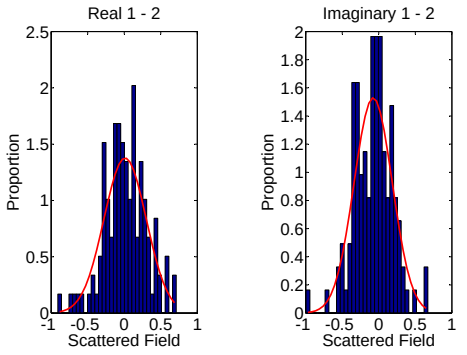

(a) m=1, n=2

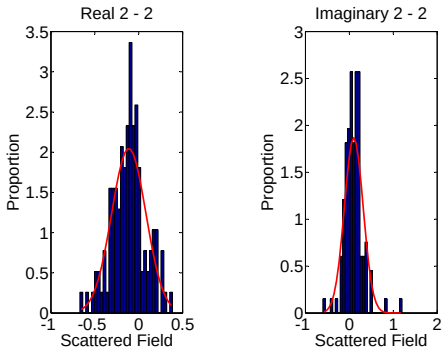

(b) m=2, n=2

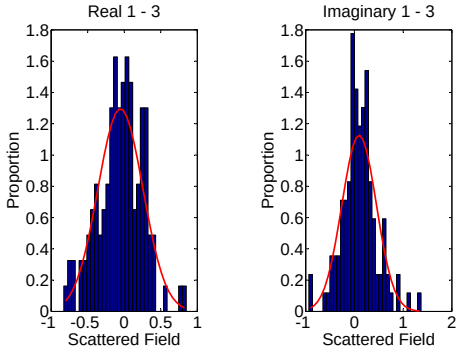

(c) m=1, n=3

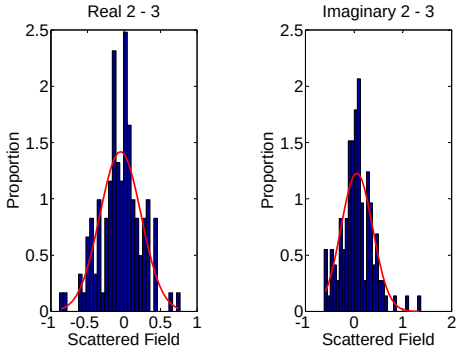

(d) m=2, n=3

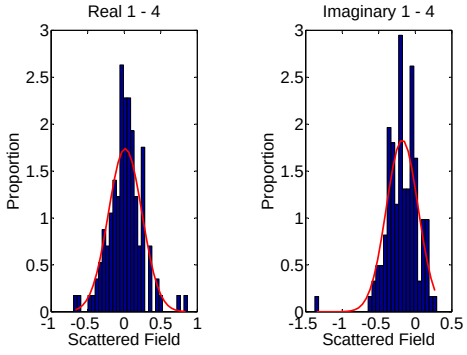

(e) m=1, n=4

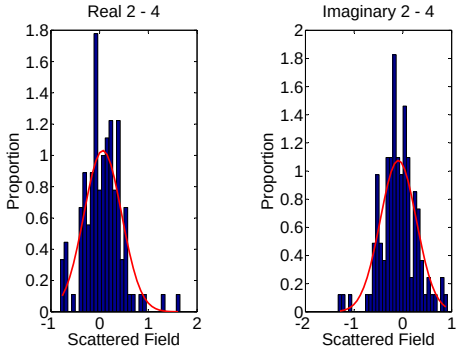

(f) m=2, n=4

Figure 5.10: Histograms of $\zeta'_{mn}[d]$ for $f_c = 2.75$ GHz in blue with Gaussian probability density functions corresponding to the sample mean and variance in red.

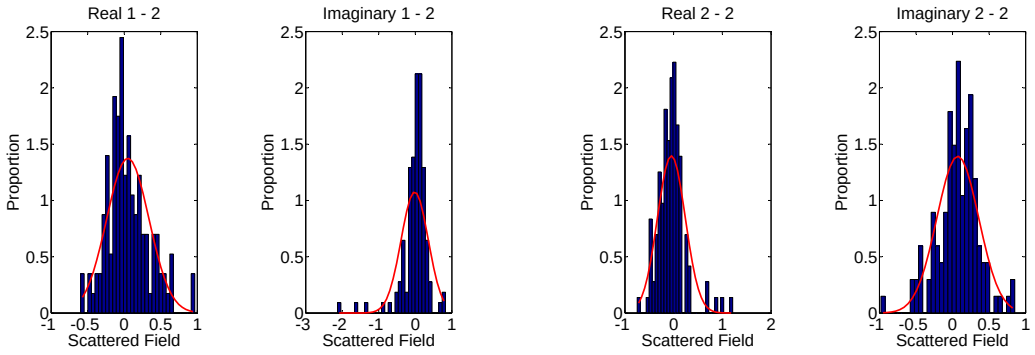

(a) m=1, n=2

(b) m=2, n=2

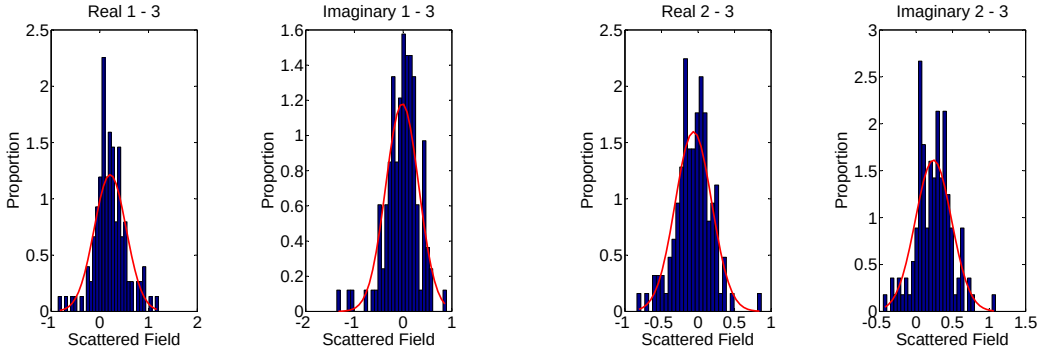

(c) m=1, n=3

(d) m=2, n=3

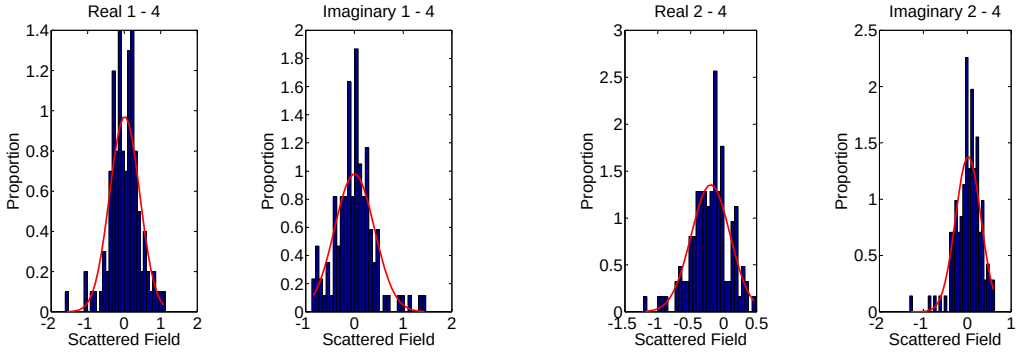

(e) m=1, n=4

(f) m=2, n=4

Figure 5.11: Histograms of $\zeta'_{mn}[d]$ for $f_c = 4.51$ GHz in blue with Gaussian probability density functions corresponding to the sample mean and variance in red.

The trials $\zeta'_{mn}[d]$ are used to estimate the covariance matrix $\boldsymbol{C}$ (size $MN \times MN$) of the received fields. Each entry in the covariance matrix is calculated according to $E\left\{\zeta'_{pq}[d]\zeta'^{*}_{st}[d]\right\}$. However, the trials $\zeta'_{mn}[d]$ were measured in the presence of receiver noise which increases the variance of the received fields slightly. It is assumed here that this noise is complex white Gaussian noise and is independent of the target measurement. This noise variance, σ^2_{mn}, can be estimated from the calibrated range returns of the target versus azimuth angle by simply recording a single sample from each return in azimuth and calculating the sample variance. The location of this point in range was chosen such that it was far enough away from the transmit and receive elements that it could not be attributable to any real targets and would only contain power due to noise. Once σ^2_{mn} is known, it can be subtracted from the corresponding diagonal entry in the covariance matrix ($E\left\{|\zeta'_{mn}|^2\right\}$) resulting in a corrected covariance matrix $\boldsymbol{D}$. In practice, the variance of the noise with respect to the variance of the received fields from the target is very small but is accounted for regardless. To make comparisons to the the models easier, $\boldsymbol{D}$ has also been scaled by a constant such that the trace of $\boldsymbol{D}$ equals one. That is, the total energy scattered from the UAV is unity. Figs. 5.12 and 5.13 show the final covariance matrix $\boldsymbol{D}$ for both $f_c = 2.75$ and 4.51 GHz on both linear and logarithmic scales.

5.2.2 Measured and Modeled Covariance Comparison

The correlated scatterers model of the covariance matrix derived in Chapter 2 has three parameters which can be tuned: the width ΔX and length ΔY of the target, and the correlation length C_d. If the target is constrained to be a square ($\Delta X = \Delta Y$), then only two parameters can be tuned. In addition, it was shown in Section 2.4.1 that

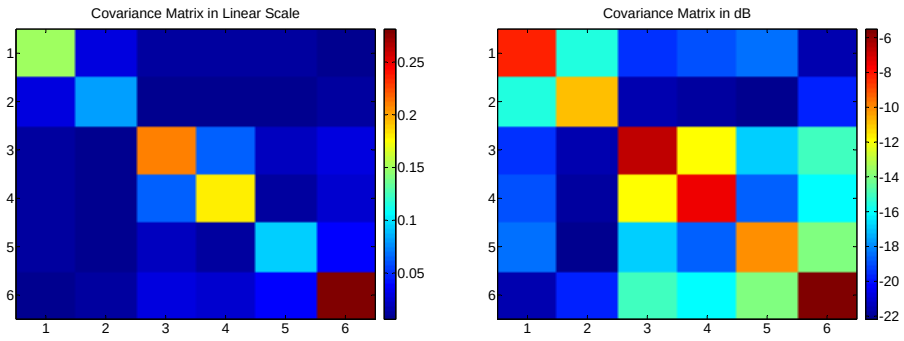

(a) Linear Scale (b) dB Scale

Figure 5.12: Magnitude of estimated covariance matrix $\boldsymbol{D}$ of the scattered fields from the UAV for f_c =2.75 GHz. The axis limits 1 through 6 correspond to transmit/receive pairs (1: 1-2), (2: 2-2), (3: 1-3), (4: 2-3), (5: 1-4), and (6: 2-4).

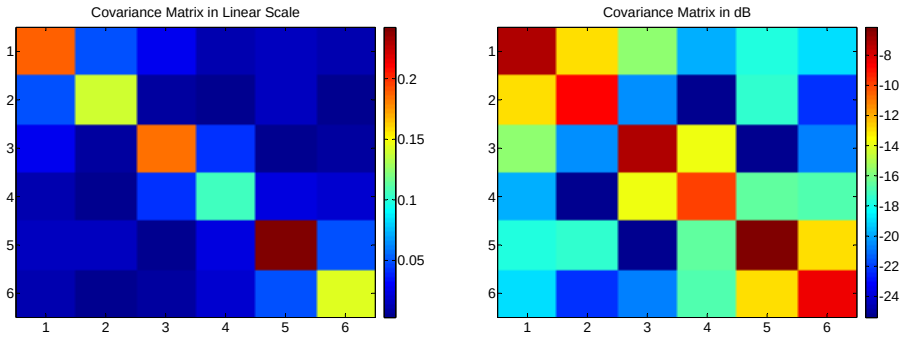

(a) Linear Scale (b) dB Scale

Figure 5.13: Magnitude of estimated covariance matrix $\boldsymbol{D}$ of the scattered fields from the UAV for f_c =4.51 GHz. The axis limits 1 through 6 correspond to transmit/receive pairs (1: 1-2), (2: 2-2), (3: 1-3), (4: 2-3), (5: 1-4), and (6: 2-4).

detection performance of the correlated scatterers model for a specific set of antenna locations is dependent on the rotation angle of the rectangular target. Therefore, for a given set of parameters $\Delta X = \Delta Y$ and C_d, the resulting covariance matrix should be averaged over realizations of varying azimuth angles.

An attempt was made to fit the covariance matrix predicted by the correlated scatterers model, averaged over 360° in azimuth, to the measured covariance matrix $\boldsymbol{D}$. A simple two-dimensional search was performed to discover the values of ΔX and C_d that minimize the mean squared error (MSE) between the predicted matrix and the measured matrix. If $\boldsymbol{A}$ is the predicted covariance matrix averaged over azimuth, the MSE between the two matrices is

$$\text{MSE} = \frac{||\boldsymbol{D} - \boldsymbol{A}||^2}{(MN)^2} \tag{5.4}$$

Figs. 5.14 and 5.15 show the magnitude of the MSE in dB of the two-dimensional search space for the two center frequencies. A red marker has been placed at the location where the magnitude is smallest. For the 2.75 GHz center frequency, the best match is achieved for the parameters $(\Delta X = \Delta Y = 7.46\lambda, C_d = 0.001\lambda)$, while the parameters $(\Delta X = \Delta Y = 10.94\lambda, C_d = 0.078\lambda)$ minimize the error for the 4.51 GHz center frequency. Converting to meters using the center frequencies measured, the model parameters are $(\Delta X = \Delta Y = 0.81m, C_d = 0.001m)$ and $(\Delta X = \Delta Y = 0.72m, C_d = 0.005m)$ respectively. The quality of the fit can be measured by analyzing the minimum MSE as a percentage of the mean square of the original covariance matrix calculated according to

$$\%\ \text{error} = \frac{||\boldsymbol{D} - \boldsymbol{A}_{fit}||^2}{||\boldsymbol{D}||^2} * 100 \tag{5.5}$$

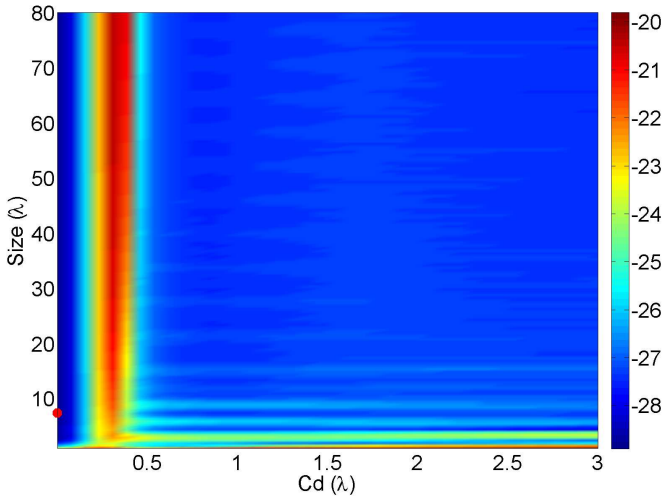

Figure 5.14: MSE for every point in the two dimensional search over size and correlation length to find the best fit $\boldsymbol{A}$ to the measured covariance matrix $\boldsymbol{D}$ for f_c =2.75 GHz. Both the size and C_d are shown in wavelengths. The MSE is in dB. The red marker corresponds to the best fit.

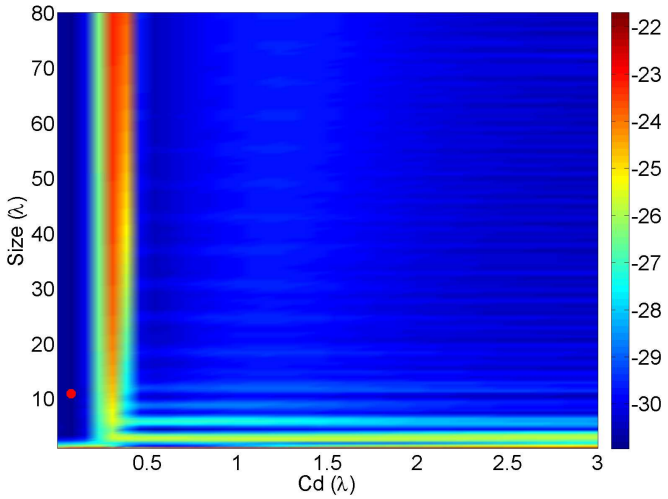

Figure 5.15: MSE for every point in the two dimensional search over size and correlation length to find the best fit $\boldsymbol{A}$ to the measured covariance matrix $\boldsymbol{D}$ for f_c =4.51 GHz. Both the size and C_d are shown in wavelengths. The MSE is in dB. The red marker corresponds to the best fit.

Performing this calculation, the percent error is 22.8% and 13.6% for 2.75 GHz and 4.51 GHz respectively. It should be noted that since the matrices being fitted have large terms along the diagonal, these will tend to dominate the MSE. However, one could place more emphasis on the smaller off-diagonal terms by taking a logarithm of the difference in (5.4).

The covariance matrices of the fitted model for the two different frequencies are shown in Figs. 5.16 and 5.18 in dB. These can be compared directly to the measured covariance matrices for the same frequencies in Figs. 5.12(b) and 5.13(b). In both the measured and fitted covariance matrices, the off-diagonal entries are small, although the fitted covariances tend to underestimate these. Comparisons of the diagonal entries alone, which represent the average received power for each transmit/receive element pair are shown in Figs. 5.17 and 5.19. The diagonal entries in these figures have been reordered by increasing bistatic angle between the transmitter/receiver pairs according to Table 5.2. The best match for both center frequencies corresponds to a very small value for C_d, so the best matched covariance matrix is essentially constant along the diagonal.

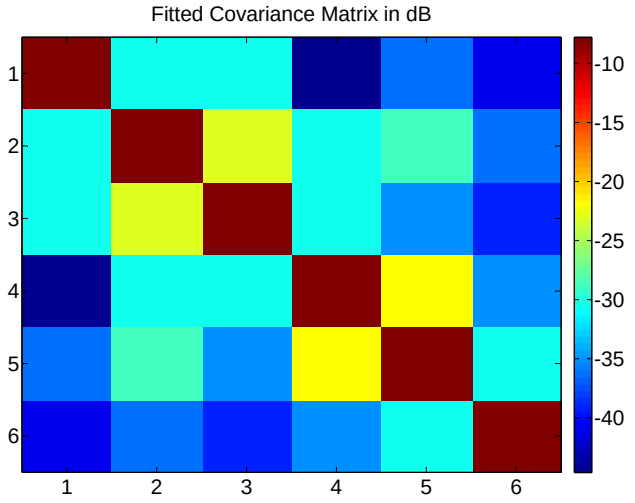

Figure 5.16: Fitted covariance matrix $\boldsymbol{A}$ in dB for f_c =2.75 GHz calculated using the parameters ($\Delta X = \Delta Y = 7.46\lambda = 0.81m, C_d = 0.001\lambda$).

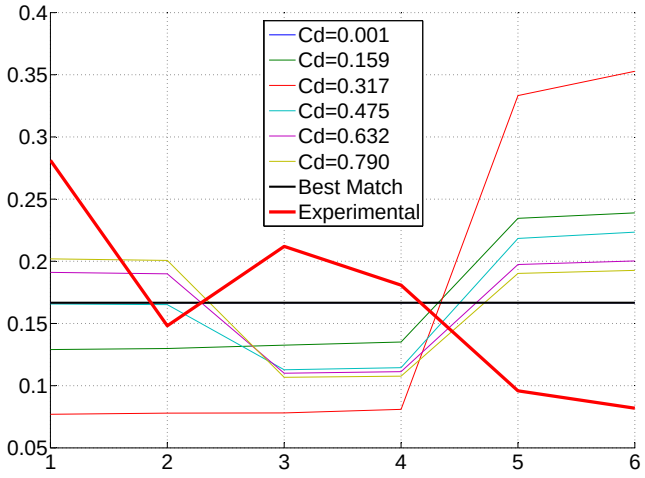

Figure 5.17: Comparison of the diagonals of the measured covariance matrix and the correlated scatterers model covariance matrix for f_c =2.75 GHz. Here, the diagonal entries have been reordered by increasing bistatic scattering angle. The axis limits 1 through 6 correspond to transmit/receive pairs (1: 2-4), (2: 1-2), (3: 1-3), (4: 2-3), (5: 1-4), (6: 2-2).

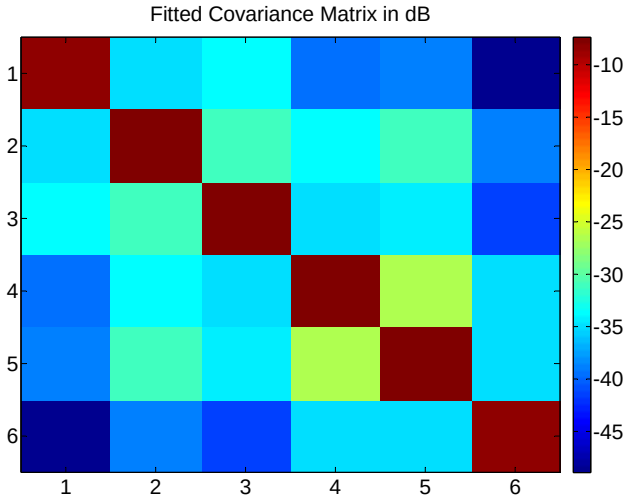

Figure 5.18: Fitted covariance matrix $\boldsymbol{A}$ in dB for f_c =4.51 GHz calculated using the parameters ($\Delta X = \Delta Y = 7.46\lambda = 0.81m, C_d = 0.001\lambda$).

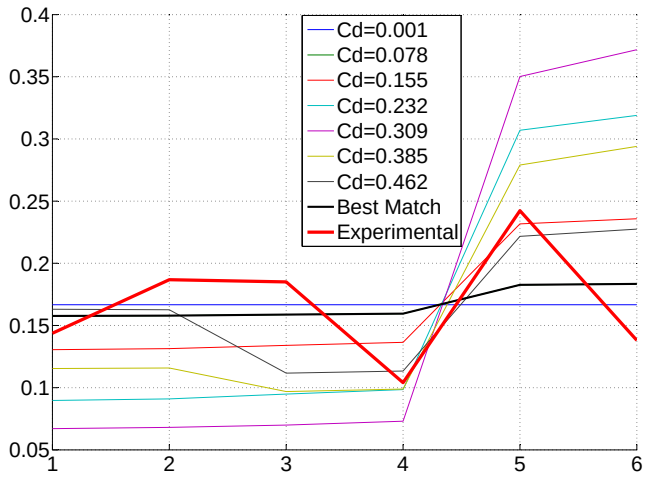

Figure 5.19: Comparison of the diagonals of the measured covariance matrix and the correlated scatterers model covariance matrix for f_c =4.51 GHz. Here, the diagonal entries have been reordered by increasing bistatic scattering angle. The axis limits 1 through 6 correspond to transmit/receive pairs (1: 2-4), (2: 1-2), (3: 1-3), (4: 2-3), (5: 1-4), (6: 2-2).

The final step in the evaluation of the correlated and uncorrelated scatterers model is to compare the probability of detection predicted by the statistical model to that of the actual measured data. Using (2.22), the probability of missed detection ($P_{MD} = 1 - P_D$) is calculated for the measured and fitted covariance matrices for $P_{FA} = 10^{-4}$. The P_{MD} is also calculated directly from the experimental data by adding complex white Gaussian noise to the measurements and applying a threshold which satisfies the desired P_{FA}. The three P_{MD} curves for the two center frequencies are shown in Figs. 5.20 and 5.21. For additional points of reference, the P_{MD} curves for the uncorrelated scatterers model and the traditional phased array as derived by *Fishler et. al.* are included as well.

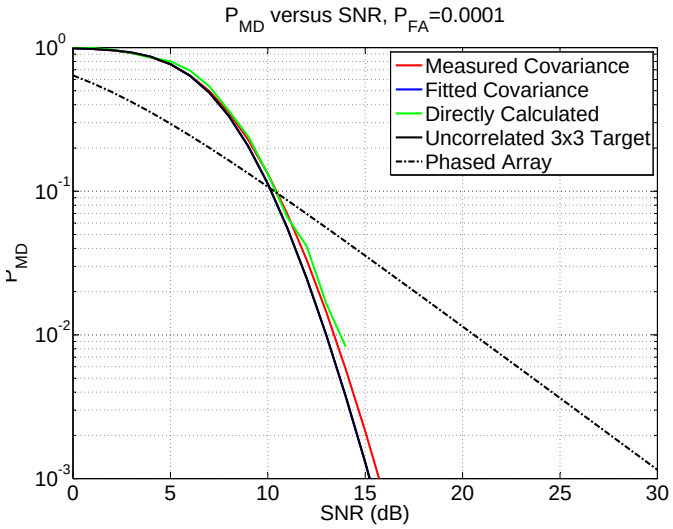

Figure 5.20: Probability of missed detection versus SNR for the measured and fitted covariance matrices as well as the actual measured data. The center frequency is f_c =2.75 GHz.

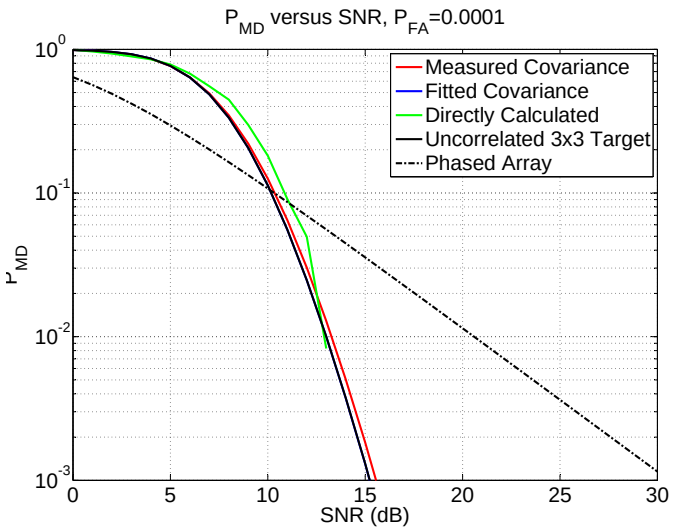

Figure 5.21: Probability of missed detection versus SNR for the measured and fitted covariance matrices as well as the actual measured data. The center frequency is f_c =4.51 GHz.

5.3 Discussion

The purpose of the work outlined in this chapter is to evaluate the validity of the uncorrelated and correlated scatterers models described in Chapter 2 using real-world measurements of a complex radar target. A small scale UAV was placed in the anechoic chamber and measured using $M = 2$ vertically polarized transmitters and $N = 4$ vertically polarized receivers as it was rotated 360° in azimuth. The scattered fields from the UAV from each transmitter were separated in the receivers using matched filtering, relying on the low cross-correlations of the LFM waveforms assigned to each transmitter. The scattered fields were calibrated using separate measurements of a metal sphere which were compared to the analytical solution of the scattered fields from a sphere. A time-domain gate was applied to the calibrated range returns to

isolate the target, and the frequency-domain response of the target alone was calculated. A single point in the Fourier domain corresponding to the center frequency of the measurement was recorded for each azimuth angle and pair of antennas to represent the scattered fields from the target. As the samples for a given transmit/receive element pair are correlated over small rotations in azimuth, the azimuth measurements were downsampled to decrease the amount of correlation. A covariance matrix describing these calibrated and downsampled scattered fields was calculated under the assumption that the fields are drawn from a Gaussian distribution. An attempt was made to fit the correlated scatterers model to this measured covariance matrix by searching a two-dimensional space to find a target size and C_d which resulted in the smallest mean-squared error between the measured covariance matrix and the correlated scatterers model. P_{MD} curves were then calculated to study how accurately the models predict the actual detection performance of the MIMO system for the UAV under test.

The first step in evaluating the correlated scatterers model is to analyze the results of the fit procedure which attempted to find the model parameters which most accurately predicted the covariance of the scattered fields. The fitted size of the random target ($\Delta X = \Delta Y$) was 0.81 m and 0.72 m for each center frequency respectively. The calibrated range returns for a given transmitter receiver pair ($m = 2$, $n = 4$) versus azimuth angle can be utilized to generate an inverse synthetic aperture radar (ISAR) image of the UAV using a synthetic aperture which subtends 45° of a circle about the target and the near-field imaging function described later in Chapter 6. While this procedure is not detailed here, the result is given in Fig. 5.22 which compares a photo of the UAV to the ISAR image. The largest scattering centers are visible in

the image in red, and the region which bounds these scatterers is roughly similar in size to the $\Delta X - by - \Delta Y$ target size corresponding to fitted statistical model. This lends credibility to the statistical target size which best fits the measured data.

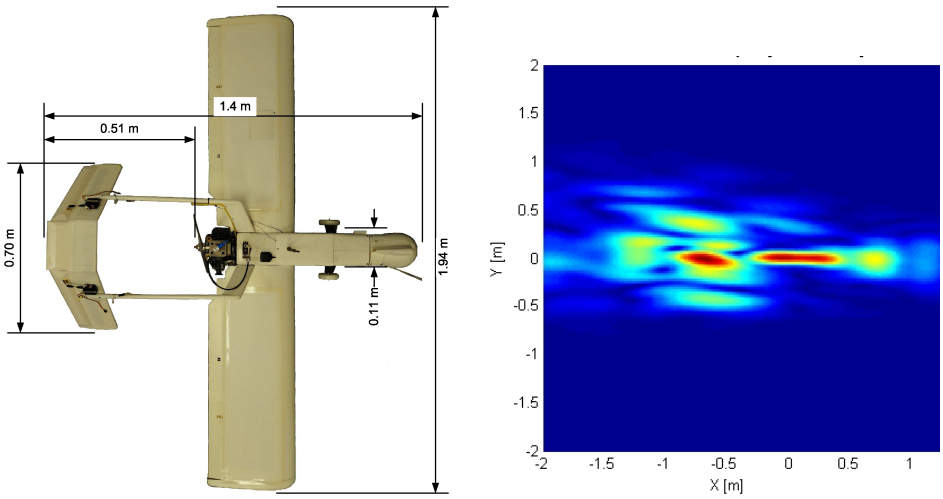

(a) UAV (b) ISAR Image

Figure 5.22: Comparison of the UAV to an ISAR image generated by Ninoslav Majurec using the 2.75 GHz measurements versus azimuth. The largest scattering centers are visible in red.

The correlation length C_d which best fits the measured covariance matrix is quite small in both cases, such that the fitted covariance matrix is almost diagonal. This would suggest that the target scattering is not dependent on the bistatic angle between transmitters and receivers. The average RCS values listed in Table 5.3 support this conclusion in that the average RCS varies only a few dB as the bistatic angle varies from 20.4° to 68.7°. This would suggest that the target consists of many independent scattering centers at the frequencies of interest.

The final point of evaluation for the statistical target models is their ability to predict the detection statistics for the UAV. The P_{MD} curves for the measured covariance matrix and the fitted covariance matrix are very similar to that predicted by the original uncorrelated scatterers model as can be seen in Figs. 5.20 and 5.21. Furthermore, all three of these curves estimate the performance of the system very well when compared to the P_{MD} calculated by simply thresholding the real data in the presence of noise. This is an important point as it is experimentally shown here that slope of the P_{MD} curve for the MIMO system falls off as sharply as originally predicted by *Fishler et. al.* with respect to the phased array system, confirming the SNR cutoff point at which the MIMO system with spatially diverse transmitters and receivers outperforms the phased array in target detection.

CHAPTER 6

MIMO RADAR IMAGING RESULTS

Urban surveillance and earth remote sensing applications typically require wide swath coverage and fine azimuth resolution. These two parameters cannot be maximized independently in a traditional single antenna oblique-looking synthetic aperture radar (SAR) system because of constraints on the physical antenna size, transmit power, and pulse repetition frequency (PRF) [41]. Techniques such as displaced phase center (DPC) sampling have been proposed to resolve azimuth ambiguities for low PRFs by sampling multiple points in the synthetic aperture simultaneously for a single pulse [41, 42]. Spaceborne SAR systems with analog beamforming arrays can trade off wide swath width for azimuth resolution or vice versa by operating in two modes, typically referred to as *Spotlight mode* or *ScanSAR mode*. In *Spotlight mode*, the transmit and receive beams are steered to dwell on a single spot on the ground, thereby increasing the length of the synthetic array and improving azimuth resolution [43, 44]. *ScanSAR mode*, on the other hand, requires steering of the beam in elevation to consecutively image multiple ranges [45]. A single transmit antenna coupled with digital beamforming on receive can be utilized to image multiple ranges simultaneously thereby improving both azimuth resolution and swath width [46], at the expense of higher transmit power due to lower transmit antenna gain. Instead

of using a single transmit antenna, more complex SAR systems have been proposed which use a transmit array with analog beamsteering and multidimensional waveform encoding in conjunction with digital beamforming on receive to improve the SNR and resolve azimuth ambiguities [47].

MIMO systems with co-located antennas are being studied as a logical progression beyond phased arrays for SAR imaging systems. The ARTINO airborne radar for UAVs, for example, utilizes a co-located sparse MIMO array to form 3D images [1–3]. The sparse array is located on the wings of the UAV and points in the nadir direction. Resolutions in the three imaging dimensions are generated by range compression in the nadir dimension, digital beamforming in the across-track dimension, and synthetic aperture processing in the along-track direction. For acceptable resolution for this application in the across-track dimension, a standard phased array would require approximately 1120 elements. However, the ARTINO principle uses a sparse array with a far fewer number of transmitters and receivers by forming a "virtual array" with the required element spacing to avoid grating lobes. The virtual array elements are located at the center of mass between a given transmitter and receiver pair, and can only be formed if there is a method by which the fields due to each transmitter can be separated unambiguously at every receiver. Some techniques mentioned to enable the transmitted signals to be separated by the receivers include time division multiplexing, frequency diversity, and waveform diversity [1].

While the ARTINO concept uses a MIMO virtual array to provide a third dimension to traditional 2D SAR imaging, the MIMO virtual array may be applicable to SAR in other ways as well. For instance, if waveform diversity is used, not time division multiplexing as is suggested for use in the ARTINO literature, a sparse linear

MIMO array of transmitters and receivers can be used in the along-track direction. These transmitters and receivers, all broadcasting and receiving simultaneously, could form a filled virtual array in the along-track direction which could potentially be used with the DPC technique. This would relax the requirements on the PRF of the system in long range *ScanSAR* considerably. Also, MIMO virtual array processing also allows for beam steering on both transmit and receive in post-processing, thereby increasing the SNR at longer ranges.

In this chapter, the applicability of MIMO to imaging is explored by first studying the virtual array concept through simple simulation. In Section 6.1, the imaging formulation will be reviewed followed by a comparison of the imaging results obtained using both a virtual array and a filled array. The virtual array results will also be analyzed in the case where the elements are formed using waveform diversity versus time division multiplexing. This is of particular interest when imaging complex or distributed targets as difficulty separating the transmitted waveforms unambiguously at the receivers may occur. Therefore, simulations are presented to analyze this case as well. Finally, results of imaging a sphere using real data captured with the SDR system will be presented in Section 6.2 where the data was generated using time division multiplexing and also simultaneous measurements utilizing waveform orthogonality.

6.1 MIMO Virtual Arrays

It is well known that a uniformly spaced array of antennas can be used to cohere a beam in a given direction using appropriate phase shifts across the elements [48]. The beam can be used to scan across some scene of interest, and the resulting range

and angle information can be used to generate an image of the scene. The down range resolution of the resulting image is a function of the bandwidth of the system (B), and is defined as $\Delta R \cong c/2B$ where c is the speed of light. If a uniformly spaced linear array of real elements is used, the cross range resolution at range R is $\Delta = \lambda R/2D$. D in this case is the size of the real array of elements. The spacing of the elements in the real array must be less than or equal to $\lambda/2$ to avoid grating lobes in the array pattern at all scan angles, which translate to spatial ambiguities in the image.

SAR imaging utilizes the inherent motion of the imaging platform, or the motion of the scene with respect to the platform, to sample the fields at each point in the array using only a single element. The sampled array can be made significantly larger, depending on the antenna pattern of the element, thereby providing much increased cross range resolution. After consideration of the maximum synthetic aperture size that can be achieved for a given element size, the cross range resolution of the synthetic array simplifies to $D/2$, where D in this case is the size of the real antenna element, not the array. It has been shown elsewhere that the one-way patterns of the real and synthetic arrays are the same. However, while the two-way response of a real array is simply the square of its one-way response, the two-way response of the synthetic array is formed through a coherent summation of the received fields measured at every point in the array. This coherent summation results in a beamwidth which is half that of the two-way response of a real array [49]. In addition, to avoid ambiguities in the two-way synthetic pattern, the spacing between synthetic elements must be $\lambda/4$ (ignoring element pattern effects).

Imaging with an array of transmitters and receivers which utilize independent transmit waveforms follows the same rules as imaging with a synthetic array. If it

is assumed that a method exists for a given receiver to separate unambiguously the range returns resulting from every transmitter, a system with M transmitters and N receivers creates MN synthetic elements. The real M transmitters and N receivers here will be referred to as the MIMO array, whereas the the MN resulting synthetic elements will be referred to as the virtual array. For a standard SAR array, the synthetic elements are formed through a series of monostatic measurements, that is, the transmitter and receiver are in the same location for each individual synthetic element. However, in the MIMO case, each transmitter and receiver pair is separated by some distance with a non-zero bistatic scattering angle. The virtual array elements are located halfway between each transmitter and receiver.

At least three monostatic-to-bistatic equivalence theorems (MBET) have been derived by various authors to show that the bistatic radar cross section (RCS) of a target is approximately equivalent to the monostatic RCS measured at the virtual element location for small bistatic scattering angles [50–52]. In addition, other authors have shown that the bistatic phase propagation to and from a point in the scene can be approximated as the monostatic phase propagation from the corresponding virtual element as long as the point of interest is far enough from the virtual element location [53]. Therefore, if the point to be imaged is sufficiently far away, the MN radar returns captured with real MIMO array elements can be treated as if they were recorded separately using synthetic elements located at the MN virtual element locations. A simulated example will show that this procedure is valid.

Images in this chapter are generated using the standard near-field back-projection imaging function described in [54]. Each transmitter m utilizes an independent transmit waveform $s_m[p]$ (p is discrete where $p = f_s t$, f_s is the sampling frequency) which

scatterers from the scene to be imaged. The superposition of these scattered fields is measured by each receiver n as $y_n[p]$. $y_n[p]$ is then passed through matched filters corresponding to each transmitted waveform, where the matched filter is defined as $h_m[p] = s_m^*[\tau - p]$, resulting in $f_{mn}[p]$. If it is assumed for a moment that the transmitted waveforms have zero cross-correlation, then the scattered fields can be separated perfectly at each transmitter and $f_{mn}[p]$ is recovered as if the MN received fields had been measured separately as in a synthetic array. Using a combination of results in [54] and [55] and adapting for this notation, the 2D near-field imaging function in the x-y plane can be written as

$$I_{nf}(x,y) = \left| \sum_{m=1}^{M} \sum_{n=1}^{N} \int_{\omega} F_{mn}(\omega) e^{j\frac{\omega+2\pi f_c}{c}\left(\left|\overrightarrow{r_m}(x,y)\right|+\left|\overrightarrow{r_n}(x,y)\right|\right)} d\omega \right|^2 \tag{6.1}$$

where $F_{mn}(\omega)$ is the discrete-time Fourier transform (DTFT) of $f_{mn}[p]$ at baseband, $\overrightarrow{r_m}(x,y)$ and $\overrightarrow{r_n}(x,y)$ are vectors which point from transmitter m or receiver n respectively to the point to be imaged, and f_c is the center frequency of the radar. If the point to be imaged is far enough from each real transmitter and receiver antenna pair, the argument of the exponential in (6.1) can be rewritten using the virtual element approximation

$$\left|\overrightarrow{r_m}(x,y)\right| + \left|\overrightarrow{r_n}(x,y)\right| \approx 2\left|\overrightarrow{r_{mn}}(x,y)\right| \tag{6.2}$$

where $\overrightarrow{r_{mn}}(x,y)$ is the vector pointing from the virtual element, located at the center of mass between transmitter m and receiver n, to the point (x,y). Under this approximation, the exponential in (6.1) can be thought of as a beamformer on both transmit and receive using the virtual array locations. In the following, this simplification will be excluded and the full near-field imaging function will be used to qualitatively illustrate the validity of the virtual array assumption.

For a system with $M = 4$ transmitters and $N = 4$ receivers, Fig. 6.1 illustrates two example MIMO element geometries and the resulting virtual arrays. In Fig. 6.1(a), the transmitters and receivers have been arranged linearly such that the resulting $MN = 16$ virtual elements form a uniform linear array. In this case, the spacing between transmitter elements is four times larger than the spacing between receiver elements. If the receiver elements have $\lambda/2$ spacing, then the virtual array elements will have $\lambda/4$ spacing, thereby eliminating grating lobes in the synthetic two-way pattern. Fig. 6.1(b) illustrates how this same process can be used to form a 4x4 rectangular virtual array. Since this array has two dimensions, it could potentially be used in 3D imaging applications as in [53].

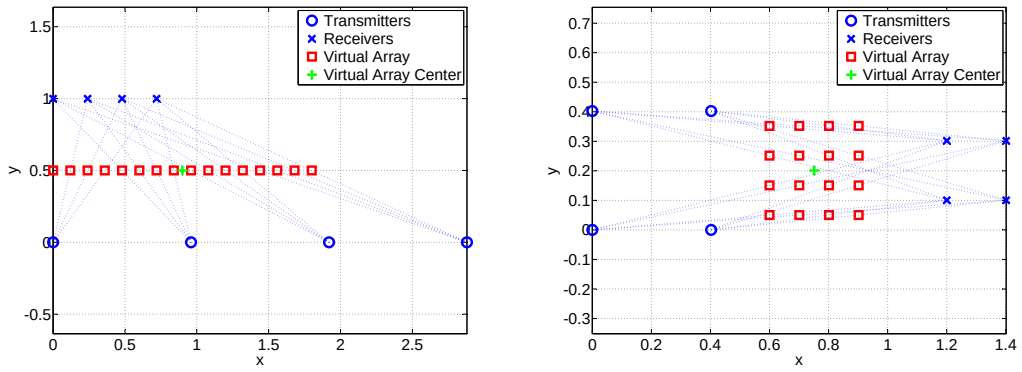

(a) Linear Virtual Array

(b) Square Virtual Array

Figure 6.1: Arrangements of real antenna elements and corresponding virtual arrays.

6.1.1 MIMO Imaging Simulation

In this section, a simulation is presented to compare imaging results using the MIMO array with M transmitters and N receivers to a synthetic array with MN

elements at the virtual array locations. For simplicity in simulation and the ability to verify the simulations using the SDR, a simple 2x2 MIMO geometry is proposed as illustrated in Fig. 6.2. The simulated system has a center frequency of 2.75 GHz, and

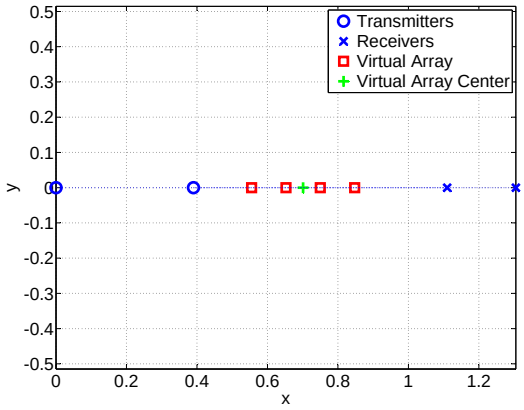

Figure 6.2: Arrangement of 2x2 real MIMO elements and corresponding virtual array elements.

a bandwidth $B = 500MHz$. The down range resolution of the system is therefore 1/3 m. To avoid spatial ambiguities in the resulting image, the virtual array elements or synthetic array elements should be separated by no more than the wavelength at the highest frequency divided by four, or 2.5 cm. However, the results of the simulation will be compared to measurements taken with the SDR system described previously. The physical size of the antenna assemblies restricts how closely the receive elements can be placed together, and the closest two elements can be placed is 19.5 cm resulting in a virtual element spacing of 9.75 cm. This is the spacing illustrated in Fig. 6.2 and is that which will be utilized here. The existence of spatial ambiguities is less than desirable in a real-world imaging system, but for the sake of exploring the MIMO

virtual array with simulated and measured results, their presence is acceptable in this instance.

Appendix B outlines the process of simulating the scattering of multiple transmit waveforms from some complex target and separating the returns in the receiver. This is done in the appendix for a rectangular target consisting of many random scatterers. For simplicity, a single point target is studied first in this section, and it is assumed that the received fields $f_{mn}[p]$ can be recovered perfectly. Under these conditions, the near-field imaging function defined in (6.1) is used to compute the image of a point target at location (x, y) =(0.44 m, 4.94 m) first using the real MIMO element locations and then using synthetic elements at the virtual element locations. This geometry is shown in Fig. 6.3. The results for these two cases are shown in Fig. 6.4.

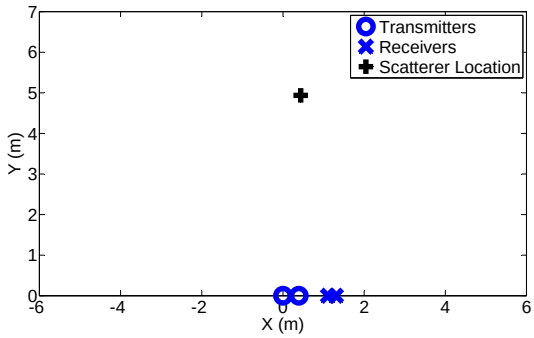

Figure 6.3: Simulation setup with point target located at (x, y) =(0.44 m, 4.94 m) and 2x2 real MIMO elements.

Fig. 6.4 shows the imaging results on both a linear and dB scale. It is clear from the linear scale plots in Figs. 6.4(a) and 6.4(c) that the images formed with the MIMO and virtual arrays are quite similar. The location and magnitude of the point

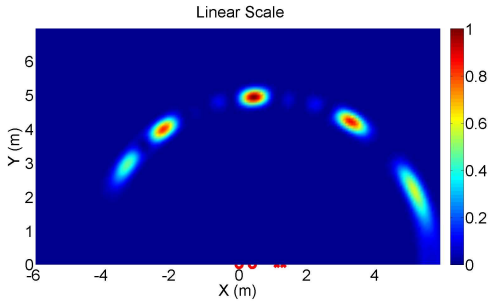

(a) MIMO Array - Linear Scale

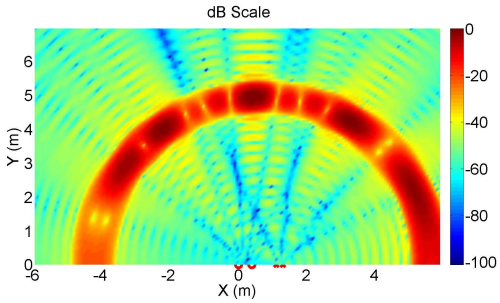

(b) MIMO Array - Log Scale

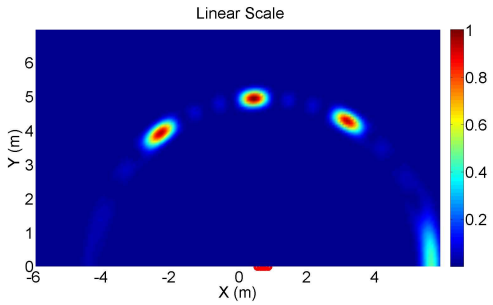

(c) Virtual Array - Linear Scale

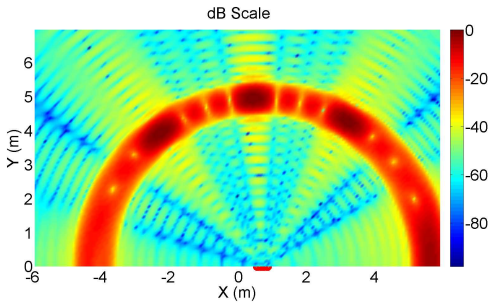

(d) Virtual Array - Log Scale

Figure 6.4: Comparison of simulated images of the point scatterer generated using the MIMO array elements and virtual array elements.

target and major spatial ambiguities on each side are nearly identical, and only the ambiguities for larger array scan angles show any significant difference. An analysis of the images on a log scale, as in Figs. 6.4(b) and 6.4(d), shows some subtle differences in the downrange profile of the target, but the effects are negligible. These results show that the approximation of the MIMO array by a virtual array is valid.

In order to use the MIMO array in a DPC-type SAR application, all M transmitters must operate simultaneously. Therefore, the transmitters should utilize some type of waveform diversity (WD). A few different types of waveforms which may be suitable for imaging are studied in Appendix B. The most obvious choice for the $M = 2$ transmitters case is to use up- and downward chirping linear frequency modulated (LFM) waveforms as defined in the appendix. For a pulse length of 1 microsecond, as is suitable for implementation with the SDR, the maximum cross-correlation of these waveforms is approximately -26 dB, meaning they should be easily separable at the receivers. An important property of the up- and downward chirping LFM waveforms is that they occupy the same frequency band and therefore can be processed coherently. Other waveforms which achieve low cross-correlations through separation in frequency may not focus correctly when imaging.

Fig. 6.5 shows the image of the point scatterer constructed using the real MIMO array and simultaneously measuring all MN elements using LFM waveforms as discussed. These images should be compared directly to Figs. 6.4(a) and 6.4(b) which were constructed using the real MIMO array but forming the MN elements separately. Because of the low cross-correlations between the transmitted waveforms, the images formed using waveform diversity are nearly identical to the images in which

the MIMO elements were measured using perfect separation. In fact, the images are so similar that any discrepancies are visible only on a log scale.

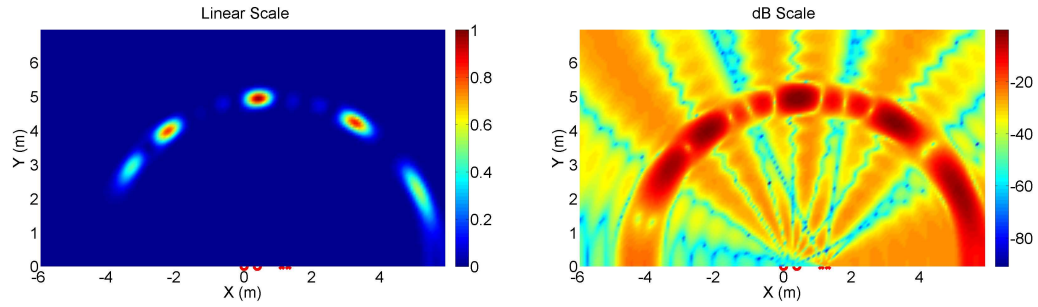

(a) WD - Linear Scale

(b) WD - Log Scale

Figure 6.5: Simulated images of the point scatterer generated using the MIMO array elements and separating the returns at the receivers using waveform diversity (WD) (Up- and downward chirping LFM waveforms).

If the magnitude-squared operation of (6.1) is ignored for a moment, the images in Figs. 6.4(a) and 6.5(a) can be coherently subtracted to compute the error introduced by process of imperfectly separating the returns using waveform diversity, resulting in Fig. 6.6. While the cross-correlation between the two LFM chirp waveforms is small at -26 dB, this has the effect of increasing the range sidelobes of the point scatterer throughout the whole image. The magnitude of the coherent subtraction shows that the maximum error in the image created using waveform diversity is approximately the level of cross-correlation between the two LFM chirp waveforms. Increasing the length of the transmitted pulse should help to minimize this error since increasing the length of the transmitted pulse decreases the cross-correlation between the waveforms.

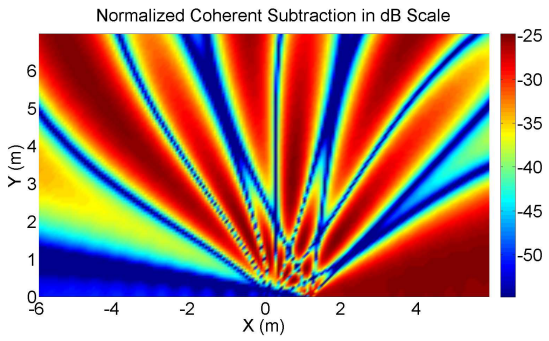

Figure 6.6: Coherent subtraction of the simulated point scatterer images generated by separating the MIMO returns perfectly or using waveform diversity.

6.1.2 Distributed Target Effects

Results in Appendix B show that it may be difficult to properly separate waveforms which occupy the same frequency band when scattered from a distributed target, as this has the effect of increasing the relative cross-correlation of the received signals. Since the goal is to apply a MIMO array using waveform diversity to imaging, this is of particular interest.

The simulation presented in the previous section has been extended here from a simple point target to a target which has some extent in down range and cross range and consists of many complex-valued random scatterers. The scatterers are uniformly spaced with a 2 cm grid spacing (approximately $1/5^{th}$ the downrange resolution) and occupy a rectangular region which is 2 m by 3 m in size. The scattering amplitudes of the complex point scatterers are uncorrelated with one another, and the real and imaginary parts of the amplitudes are independently drawn from a standard normal distribution. The scatterers have been scaled such that the total energy of the target is unity. A MIMO array geometry is used which is similar to the previous array, except

the the spacing has been chosen such that the virtual array elements are separated by $\lambda/4$ thereby removing any spatial ambiguities. Again, the images were produced two ways, either using perfect separation of the waveforms or using waveform diversity with matched filtering. As before, the waveforms chosen are up- and downward chirping LFM waveforms with 500 MHz of bandwidth and a 1000 ns pulse length.

Simulated images of the same realization of the distributed random target are shown in Fig. 6.7. Green markers denote the four corners of the rectangular target in the images. As before, differences between the two images generated using either perfect separation of received waveforms or matched filtering is small when viewed on a linear scale but some discrepancies are visible here. As before, the effects of the non-zero cross-correlation between the waveforms has the effect of raising the sidelobes of the target in the log-scale image of Fig. 6.7(d). The magnitude of the coherent subtraction of Figs. 6.7(a) and 6.7(c) is shown in Fig. 6.8. While results in Appendix B show that scattering from a distributed target can significantly decrease the relative cross-correlations of the received signals from each transmitter, the maximum error between the images generated using waveform diversity and perfectly separated received waveforms is only approximately 6 dB worse for the distributed target than in the point scatterer case.

Figs. 6.9 and 6.10 repeat the same distributed target simulation as before except with a target which is 4 m by 4m, increasing the area of the target from 6 square meters to 16 square meters. Even for this larger target, the error between the two images is still small, with the largest error being approximately -18 dB as is evident from the coherent subtraction.

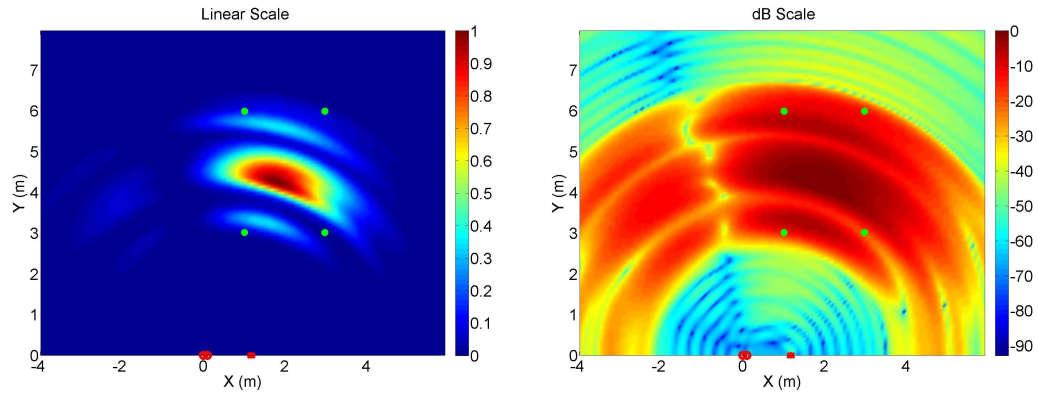

(a) Perfect Separation - Linear Scale

(b) Perfect Separation - Log Scale

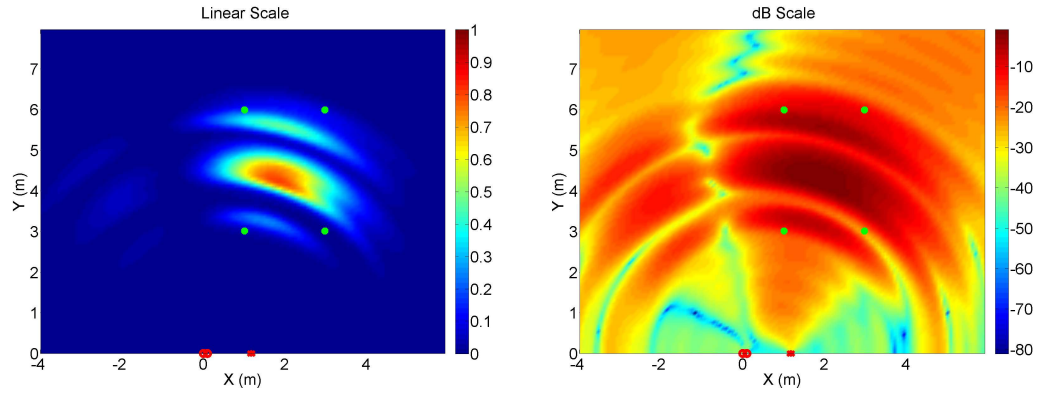

(c) WD - Linear Scale

(d) WD - Log Scale

Figure 6.7: Simulated images of a 2 m by 3 m distributed target generated using MIMO element returns which have been either perfectly separated or separated using waveform diversity (WD). The green markers in the images denote the four corners of the distributed target.

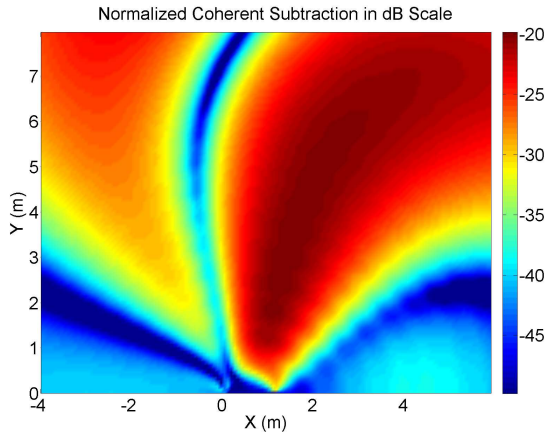

Figure 6.8: Coherent subtraction of the simulated distributed scatterer images generated by separating the MIMO returns perfectly or using waveform diversity. The target size is 2 m by 3 m.

6.2 Experimental Results

The simulation results presented in the previous sections show that a MIMO array using waveform diversity to separate the returns from each transmitter at a given receiver may be used successfully in imaging applications. This section will present measured real-world results in support of the simulated data. The SDR system is well suited to implementing a 2x2 MIMO system utilizing up- and downward chirping LFM transmit waveforms. First, the experimental setup and calibration procedures will be described followed by the measured results.

The experiment was conducted in the anechoic chamber at the ElectroScience Laboratory - The Ohio State University. Two SDR transmit and two receive assemblies were arranged such that the vertically polarized elements were located at the MIMO positions indicated earlier in Fig. 6.2, and the SDR was configured to operate with center frequency 2.75 GHz. An upward chirping LFM waveform was assigned

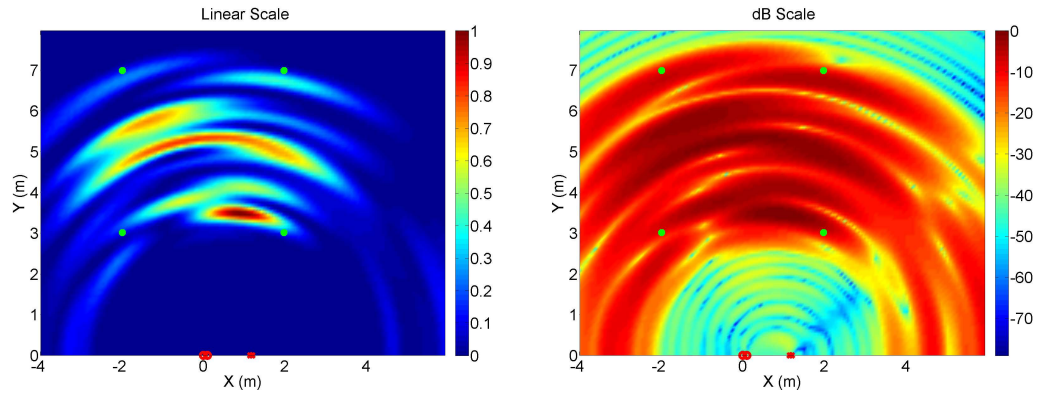

(a) Perfect Separation - Linear Scale

(b) Perfect Separation - Log Scale

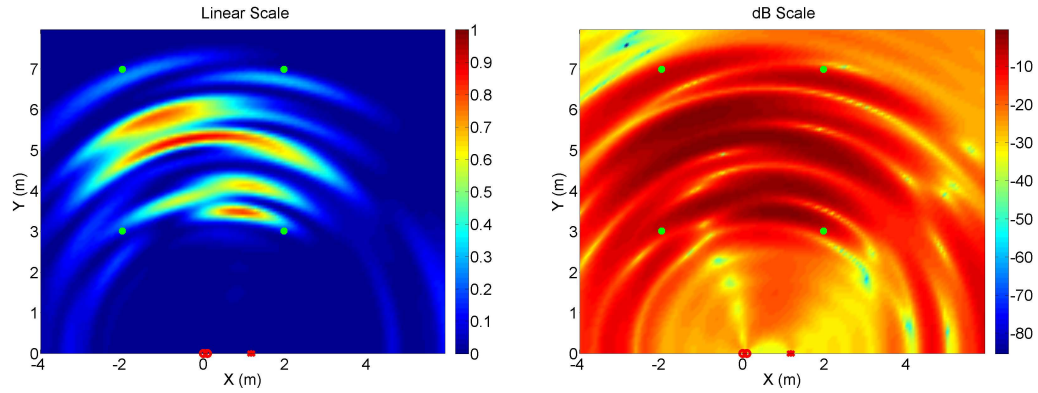

(c) WD - Linear Scale

(d) WD - Log Scale

Figure 6.9: Simulated images of the larger 4 m by 4 m distributed target generated using MIMO element returns which have either been perfectly separated or separated using waveform diversity (WD). The green markers in the images denote the four corners of the distributed target.

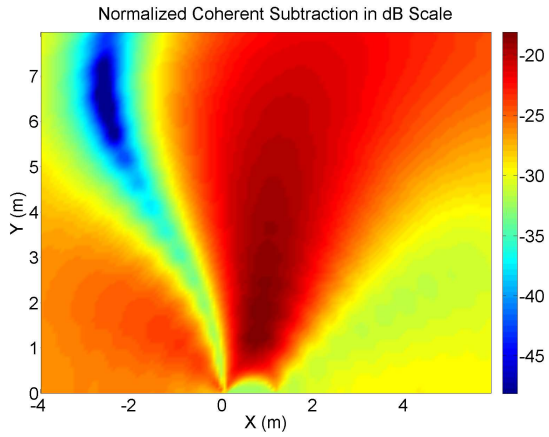

Figure 6.10: Coherent subtraction of the simulated distributed scatterer images generated by separating the MIMO returns perfectly or using waveform diversity. The target size is 4 m by 4 m.

to transmitter channel A, while a downward chirping LFM waveform was assigned to transmitter channel B. Both of these LFM waveforms utilize 500 MHz of bandwidth with a 1 microsecond pulse length. In addition, the SDR software was configured to perform two sets of measurements. The first measurement involved cycling through all four transmitter/receiver pairings, one at a time, in order to form range returns with perfect waveform separation. Since only one transmitter is active at a time, the return for one transmitter/receiver pair is not corrupted by the return from the other transmitter. In the second measurement, all transmitters and receivers were active forming all four MIMO returns simultaneously. This process was repeated three times: once for a measurement of the background with no target present, once for a small metal sphere with a diameter of 6", and once for a larger metal sphere with a diameter of 18". The center of the spheres were located at (x, y) =(0.44 m, 4.94 m) as in the simulation results presented earlier.

Fig.6.11 shows a photograph of the SDR antenna assemblies arranged in the anechoic chamber with the proper spacing. An absorber wall was placed between the transmitters and receivers to attenuate the direct propagation path between them as much as possible. A photograph of the complete measurement setup is given in Fig. 6.12 with the larger sphere positioned at the target location.

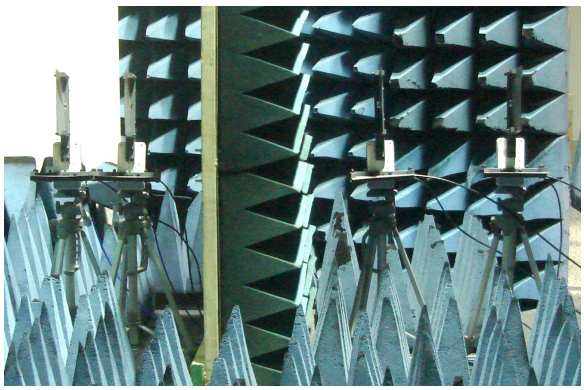

Figure 6.11: Photo of the MIMO array as configured in the ESL compact range. The transmitters are on the right of the image, while the receivers are on the left. An absorber wall was used to attenuate the direct path between transmitters and receivers.

The ability to form an image using Eq. 6.1 assumes that the match-filtered range returns $f_{mn}[p]$ have been normalized in amplitude and phase such that a point scatterer at a given location yields the correct range and phase information for all transmitter and receiver pairs. Due to variations in digital and analog components in the transmit and receive channels, cable lengths, and antenna placements, this will not be the case without some form of calibration. A simple method was proposed in Section 5.1 which used a calibration sphere to normalize the MN range returns with respect to the transmitter and receiver antenna locations. That method was applied

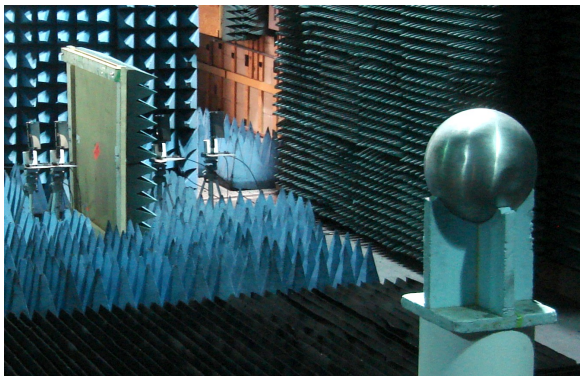

Figure 6.12: Photo of the complete measurement setup with the 18" sphere as a target.

again here, using the response from the smaller sphere to calibrate the response of the larger sphere. The calibrated response of the larger sphere for each pair of elements is denoted here as $f_{mn,ls}[p]$.

Calibrated responses of the large sphere in the time domain are shown in Fig. 6.13 for the case where the MN measurements were switched in time (denoted TD for time diversity) and all measured at once (denoted WD for waveform diversity). The baseband calibration coefficients $C_{mn}(\omega)$ were calculated once using the TD returns for the small sphere and then applied to both TD and WD large sphere returns. The large sphere response in both cases shows as a peak at around 10 m. Since the sphere was approximately broadside to the array, the total round trip distance for each of the MN transmitter/receiver pairs are roughly equal. As should be expected, the range sidelobes in the WD case are higher due to the cross-correlation of the chosen transmit waveforms.

The imaging function in (6.1) can be directly applied to $f_{mn,ls}[p]$ for both the TD and WD cases and the resulting images of the large sphere are shown in Fig. 6.14. The

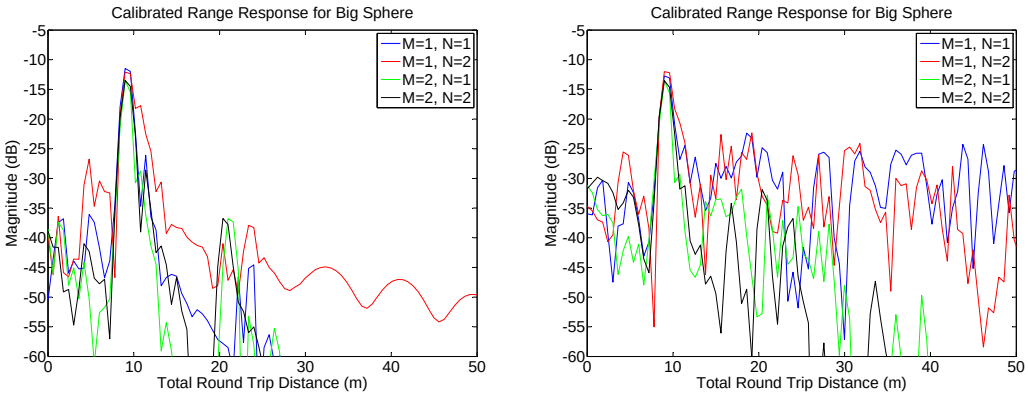

(a) TD (b) WD

Figure 6.13: Calibrated range response ($f_{mn,ls}[p]$) of the larger 18" sphere using either switched time division (TD) or waveform diversity (WD) to form all four pairs of range returns.

images look quite similar on a linear scale. These images derived from experimentally measured data should be compared directly to the simulated images in Figs. 6.4 and 6.5. The simulated images of the point scatterer agree quite well with the measured images of a sphere for both the TD and WD cases. A coherent subtraction of the experimentally measured TD and WD images shows that the maximum difference between the two images is approximately -18 dB, as illustrated in Fig. 6.15.

6.3 Discussion

Simulation results in Section 6.1.1 show that the virtual array approximation of the MIMO array is a valid one. Furthermore, the MBET and bistatic phase approximation studies show that the accuracy of the virtual array approximation should improve as the range to the target is increased. Therefore, it is likely possible

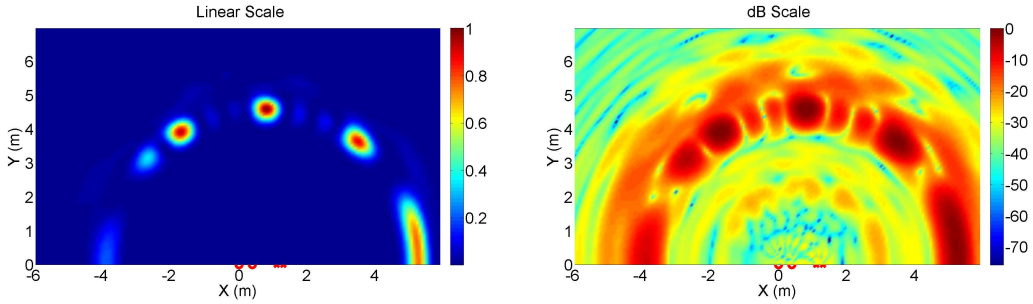

(a) TD - Linear Scale

(b) TD - Log Scale

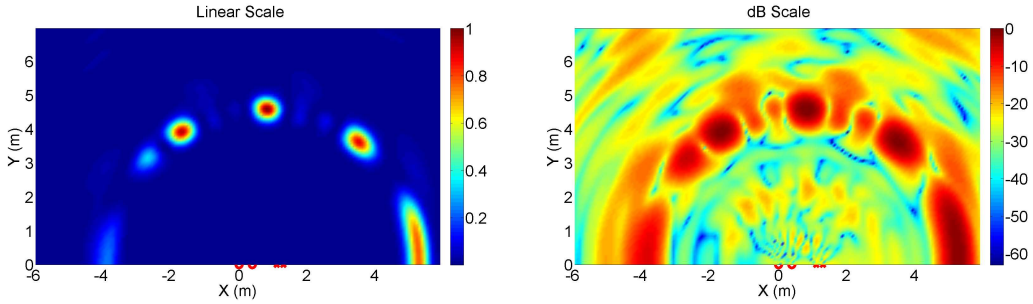

(c) WD - Linear Scale

(d) WD - Log Scale

Figure 6.14: Comparison of images of the 18" sphere using TD or WD to separate the returns at each receiver. 500 MHz LFM up- and down-chirps were used with a pulse length of 1000 ns.

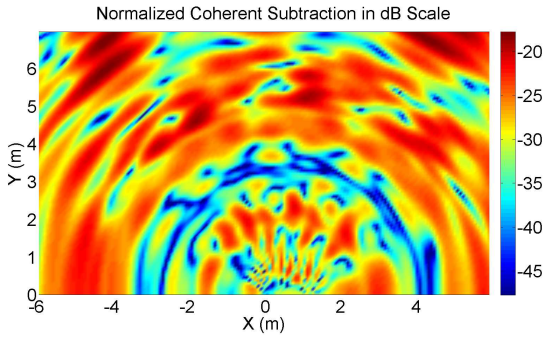

Figure 6.15: Coherent subtraction of the images of the 18" sphere constructed from experimentally measured and calibrated range returns using time division and waveform division.

to treat a sparse MIMO array as a uniformly filled virtual array in imaging techniques for SAR such as DPC, assuming waveform diversity is used.

Simulated images of a distributed random target in Section 6.1.2 attempted to study the effects of target scattering on the ability to successfully separate range returns from multiple transmitters at a given receiver when waveform diversity is used. The simulations showed that scattering from the distributed target adversely affected the resulting image when compared to the case where the returns were separated perfectly, but the errors introduced were not prohibitively large for the waveforms studied.

Finally, the SDR system was utilized to experimentally image a metallic sphere using both time diversity and waveform diversity to form the MIMO array range returns. The images formed from the measured data agree quite well with the simulated images for both the TD and WD cases. In addition to the measured images shown in the previous section which were formed with a 1000 ns pulse length, the sphere was also measured using pulse lengths of 750 ns, 500 ns, and 250 ns. Decreasing the length of the pulse has the effect of increasing the cross-correlation between transmitted waveforms. Shortening the transmitted waveform increases the amount of error in the coherent subtraction of the two images which is a measure of the error introduced by using waveform diversity. However, shortening the pulse length also decreases the signal processing gain inherent in the matched filtering process, thereby degrading the images even in the TD case.

CHAPTER 7

CONCLUSION AND FUTURE WORK

The research presented in this dissertation has focused on improving the accuracy of target models which statistically describe the scattered fields observed by a spatially diverse MIMO array. A new model was developed in Chapter 2 whose bistatic scattering behavior can be tuned to be more representative of some classes of real targets. Specifically, this new model describes a target as a rectangular region consisting of an infinite number of complex scatterers. The amplitudes of these scatterers are zero-mean complex Gaussian random variables whose correlations are described by a Gaussian function of a single new parameter: the correlation length C_d. For $C_d = 0$, the scatterers are uncorrelated and the original model is recovered. However, as C_d is increased, the scatterers become more correlated and the target begins to focus the scattered energy in the forward direction. It is shown that increasing C_d decreases the target detection performance of the system as not all antenna pairs contribute the same amount of information when observing the target.

A new software-defined radar system was built which is capable of characterizing the scattered fields from real targets using a spatially diverse MIMO array. Chapter 3 outlines the design of both the hardware and software which comprise the system. Utilizing a powerful digital baseband transceiver with a 1 GSPS dual-channel ADC

and DAC, the system is capable of generating, receiving, and coherently processing waveforms with up to 500 MHz of bandwidth. Two independent transmit channels and two independent receive channels are available, with a center frequency which can be tuned from 2-18 GHz. The performance and capabilities of the system are explored in Chapter 4 through a series of tests which were performed during different stages of the SDR assembly.

Chapter 5 outlines an experiment which was conducted to evaluate the accuracy of the statistical MIMO target models in describing the scattered fields from a real target. The SDR was set up in the anechoic chamber at the ElectroScience Laboratory with two transmit and four receive assemblies. A small-scale UAV was placed at the center of the chamber on a rotating foam column and six antenna elements were placed about the target. The SDR was then used to measure the scattered fields from the UAV for $MN = 8$ element combinations versus azimuth. Treating these azimuth measurements as independent observations of the target, the covariance matrix describing the scattered fields is estimated. The covariance matrix predicted by the correlated scatterers model is then fitted by varying the size of the random target and also the correlation length C_d. It is shown that the correlation length which best fits the measured data is nearly zero, meaning the uncorrelated scatterers model most accurately models the scattered fields for the particular measured UAV target. In addition, it is shown that the that the statistical models accurately predict the P_{MD} for the MIMO system.

The application of MIMO arrays with co-located antennas to imaging is studied in Chapter 6. First, simulations utilizing the near-field imaging function are presented to analyze the validity of treating an M by N MIMO array as a virtual array with MN

synthetic elements at the center of mass of each transmitter receiver pair. Images created using returns from the sparse MIMO array are compared to those created using returns from synthetic elements at the virtual array locations and show good agreement. Next, the MIMO array returns are simulated using up- and downward chirping LFM waveforms for the independent transmitters to study the effects of imperfect waveform separability on the images. It is shown that the error introduced attempting to image both simple point targets and more complex distributed targets is not prohibitively large. Finally, the SDR system was used to measure the real returns from a metallic sphere with a 2x2 array utilizing the same spacing and waveforms presented in the simulations. The resulting image of the sphere agrees well with the simulations of the point target.

This dissertation explored the application of MIMO techniques using both spatially diverse antennas and co-located antennas. A new statistical scattering model was introduced in an effort to more accurately predict the target detection performance of spatially diverse MIMO systems. The application of sparse MIMO arrays to imaging using orthogonal waveforms was also explored through simulation. The SDR system was used to provide real-world MIMO measurements in support of both of these areas of research. The key contributions of this dissertation are:

- Described a new statistical target model for spatially diverse MIMO radar which extends the Swerling-I model to more accurately predict the multistatic scattering behavior of some classes of targets.

- Outlined a new software-defined radar system with 500 MHz of bandwidth, two independent transmit and receive channels, and a center frequency which is tunable from 2-18 GHz. Because of the flexibility of the SDR, it can be quickly

configured to provide experimental data in support of many different areas of radar research, not just those outlined in this disseration.

- Evaluated the validity of statistical target models in describing the scattered fields and target detection perform using measured data of a UAV. Actual measured radar returns from a small UAV were collected using the SDR.

- The application of a co-located MIMO array using orthogonal waveforms to imaging was studied through simulation. The SDR was then used to provide experimental data in support of the simulations. It was shown that imaging with MIMO arrays using orthogonal waveforms is feasible and can be used to improve next generation SAR imaging systems.

Additional effort is required to further evaluate the statistical MIMO target models. While experimental results for the small UAV presented here show good support for the statistical models, measurements of different classes of targets such as those with simpler geometries might illustrate situations where a larger C_d parameter might be required. In these cases, it might be shown that the detection performance of the MIMO system is degraded. Another area of future work lies in the application of MIMO concepts to imaging. The results presented in this dissertation analyzed the ability to unambiguously separate the returns from each transmitter when scattered from either a point target or a distributed target. This imaging analysis was performed only for a very specific pair of waveforms. Future analysis could include the effects of the transmitted waveforms on the quality of the image and the extension of the MIMO transmit array to greater than two elements. Furthermore, the experimental measurements were of a simple metallic sphere. Experimental measurements

of more complex and distributed scenes are required to further explore the effects of real distributed targets on the ability to unambiguously separate the radar returns.

APPENDIX A

SDR CUSTOM PRINTED CIRCUIT BOARD SCHEMATICS AND LAYOUTS

This appendix contains schematics, layouts, and photos of the four custom printed circuit boards (PCB) which were designed specifically for use in the SDR.

A.1 1 GHz LVPECL Clock Distribution PCB

The SDR digital transceiver contains a dual-channel 1 GSPS ADC and DAC. For coherent radar operation, these samplers share the same sample clock. The SDR sample clock is generated using a Stanford Research Systems CG-635 synthesized clock generator with an ovenized oscillator for low phase noise. This clock generator provides a differential LVPECL clock on two BNC connectors, one connector dedicated to the positive clock signal, and one dedicated to the negative clock signal. The SMT381 and SMT391 modules in the digital transceiver require two identical copies of this clock. In addition, both sampling modules expect the differential clock signals to be combined onto a single cable with the positive signal on the inner conductor and the negative signal on the outer conductor. To achieve this, a custom PCB was designed and fabricated using a 1:10 differential clock driver IC manufactured by ON

Semiconductor [56]. This IC generates 10 replicas of the LVPECL clock provided to it with low skew among the replicas.

The PCB schematic illustrating the input connections and power for this IC is given in Fig. A.1. Eight clock outputs are used, and their output circuitry given in Fig. A.2. Four clock outputs are formatted such that the differential signals are combined onto a signal connector, while the other four outputs are formatted such that the differential signals are separated across two connectors. All LVPECL inputs and outputs include a matching network which provides a 50-ohm impedance to maintain signal integrity for such a fast clock rate.

The physical layout of the 4-layer PCB is shown in Fig. A.3. The clock inputs are located on the bottom edge of the PCB, while the outputs occupy the other three edges. The transmission line lengths for each LVPECL clock output have been equalized to minimize clock skew caused by the physical fanout from the IC. This is the motivation behind the meandering of the transmission lines to each output in the figure. A photo of the final assembled PCB is shown in Fig. A.4. The PCB is mounted inside the computer case near the SMT391 and SMT381 modules, and is powered using +12V from the computer's power supply.

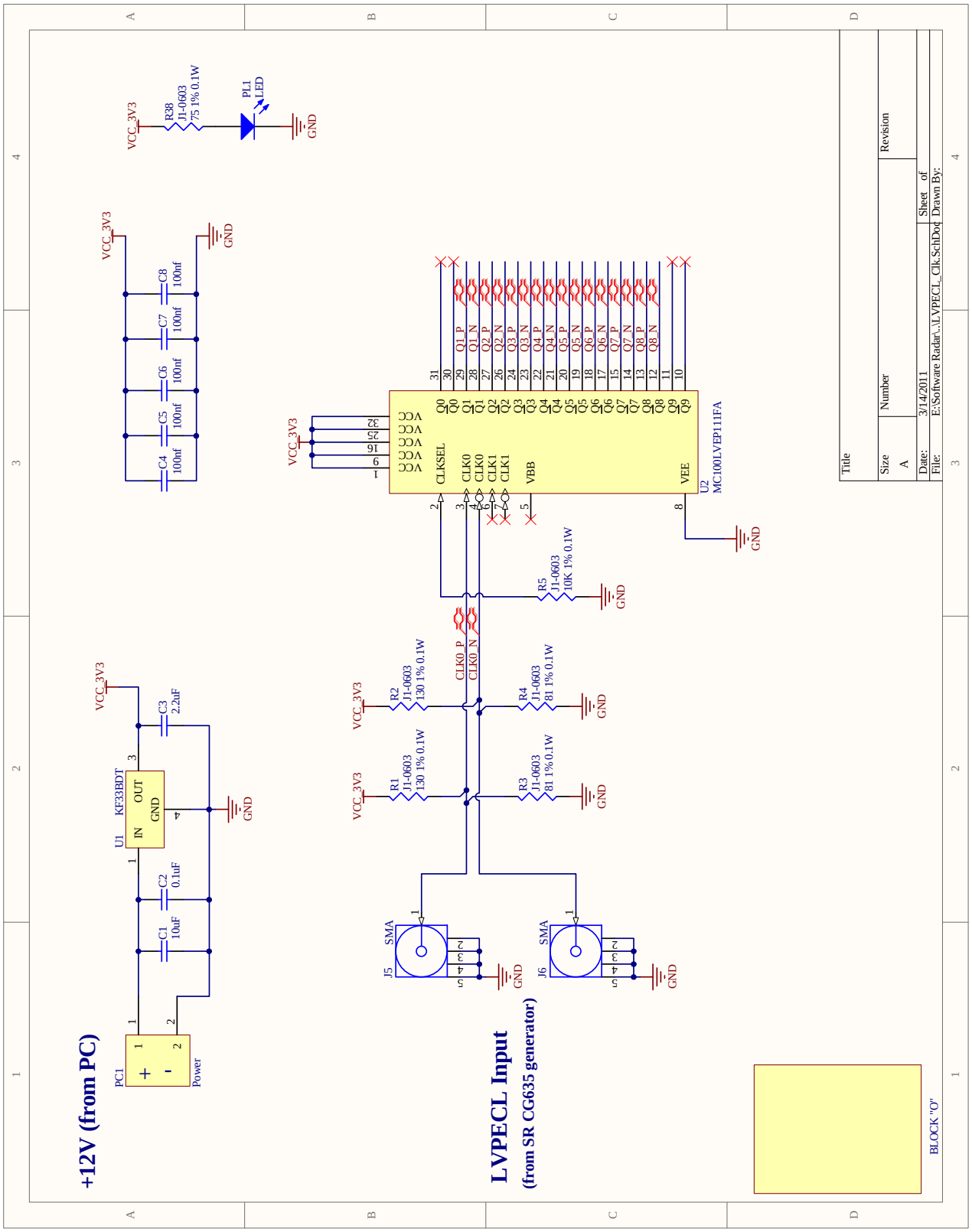

Figure A.1: Schematic of 1 GHz LVPECL clock distribution PCB showing input and LVPECL duplication chip.

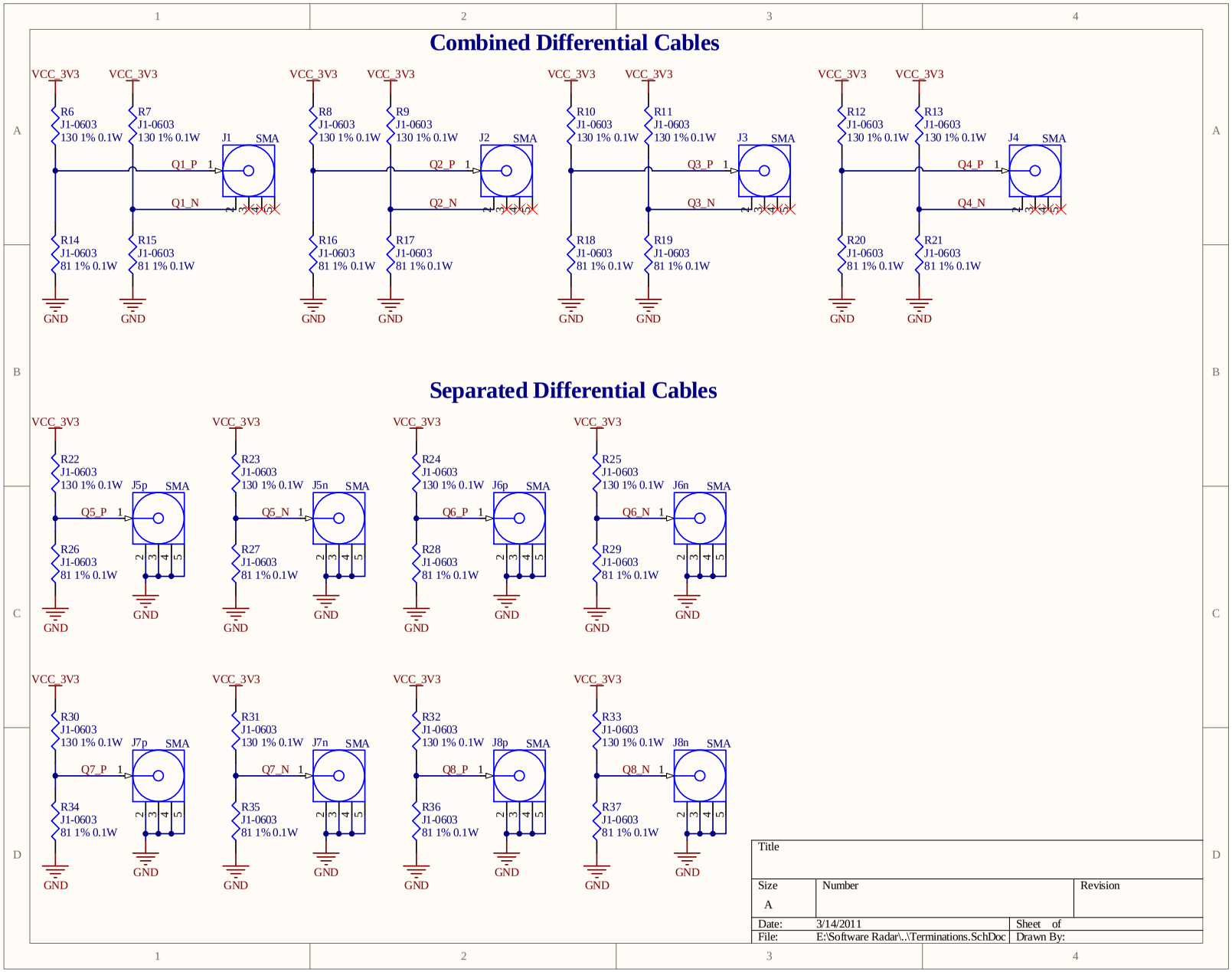

Figure A.2: Schematic of 1 GHz LVPECL clock distribution PCB showing output matching circuitry.

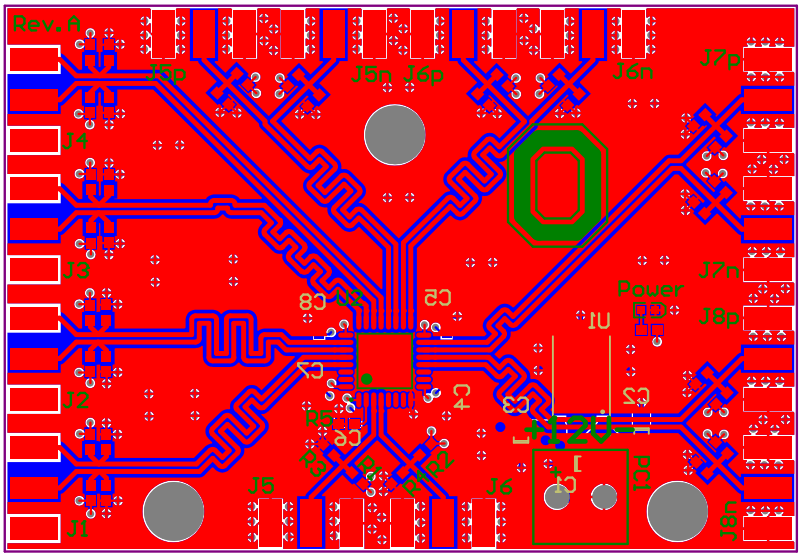

Figure A.3: 1 GHz LVPECL clock distribution PCB layout viewed from the top.

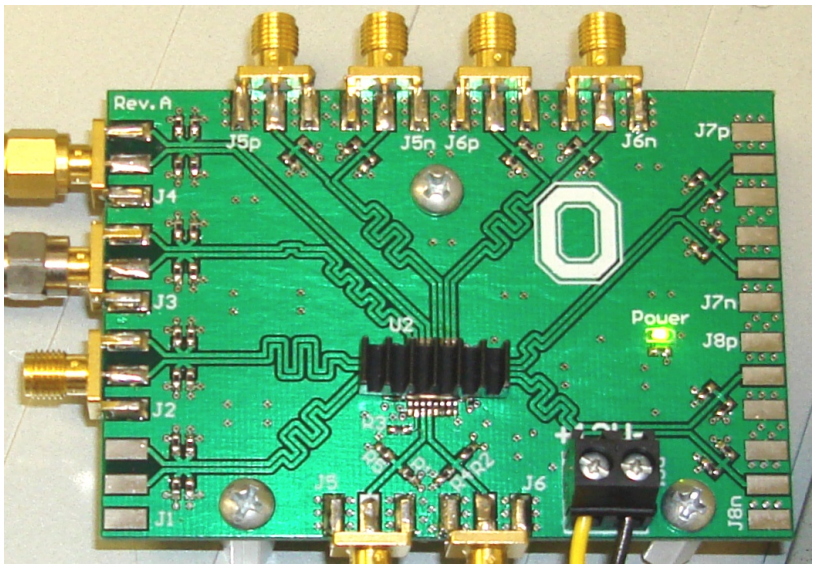

Figure A.4: 1 GHz LVPECL clock distribution populated PCB viewed from the top.

A.2 FPGA Digital Output Buffer PCB

The SDR digital transceiver described in Section 3.2.1, in combination with the computer which contains it, interacts with all RF switches and digitally controlled RF components in the tunable RF front end and antenna switch matrix described in Sections 3.2.2 and 3.2.3. The transmitter FPGA on the SMT368A module in the digital transceiver, in particular, has direct control over the RF switches which comprise the antenna switch matrix. However, the SMT368A has no dedicated general purpose I/O pins which are easily accessible. The module does have two unused comport connections which are physically connected to 12 FPGA I/O pins each. The FPGA digital output buffer PCB described here provides access to these comports using an FMS connector and a level shifting transceiver IC as shown on the left side of the schematic in Fig. A.5. The 12-bit buffered output is available on a standard D-sub-15 connector. The SDR utilizes two of these PCBs to provide 24 bits of control to the antenna switch matrix.

The FPGA digital output buffer PCB was originally designed to convert the 3.3V LVTTL outputs from the FPGA to 5V TTL outputs. However, it was determined later that only 3.3V LVTTL outputs were required. Therefore, the 5V regulator (U2 in Fig. A.5) was left unpopulated in final assembly, and the VCC_5V signal in the schematic was connected directly to VCC_3V. Using this modification, both the inputs and outputs of the buffer IC are 3.3V LVTTL. The physical layout of the 2-layer board as sent for manufacture is shown in Fig. A.6, while a photo of the completely assembled buffer board is shown in Fig. A.7. In the photo, the input FMS cable is on the left, while the output D-sub-15 cable is on the right. Two of these

boards are mounted in the PC case with the digital transceiver, and they are powered using +12V from the PC's power supply.

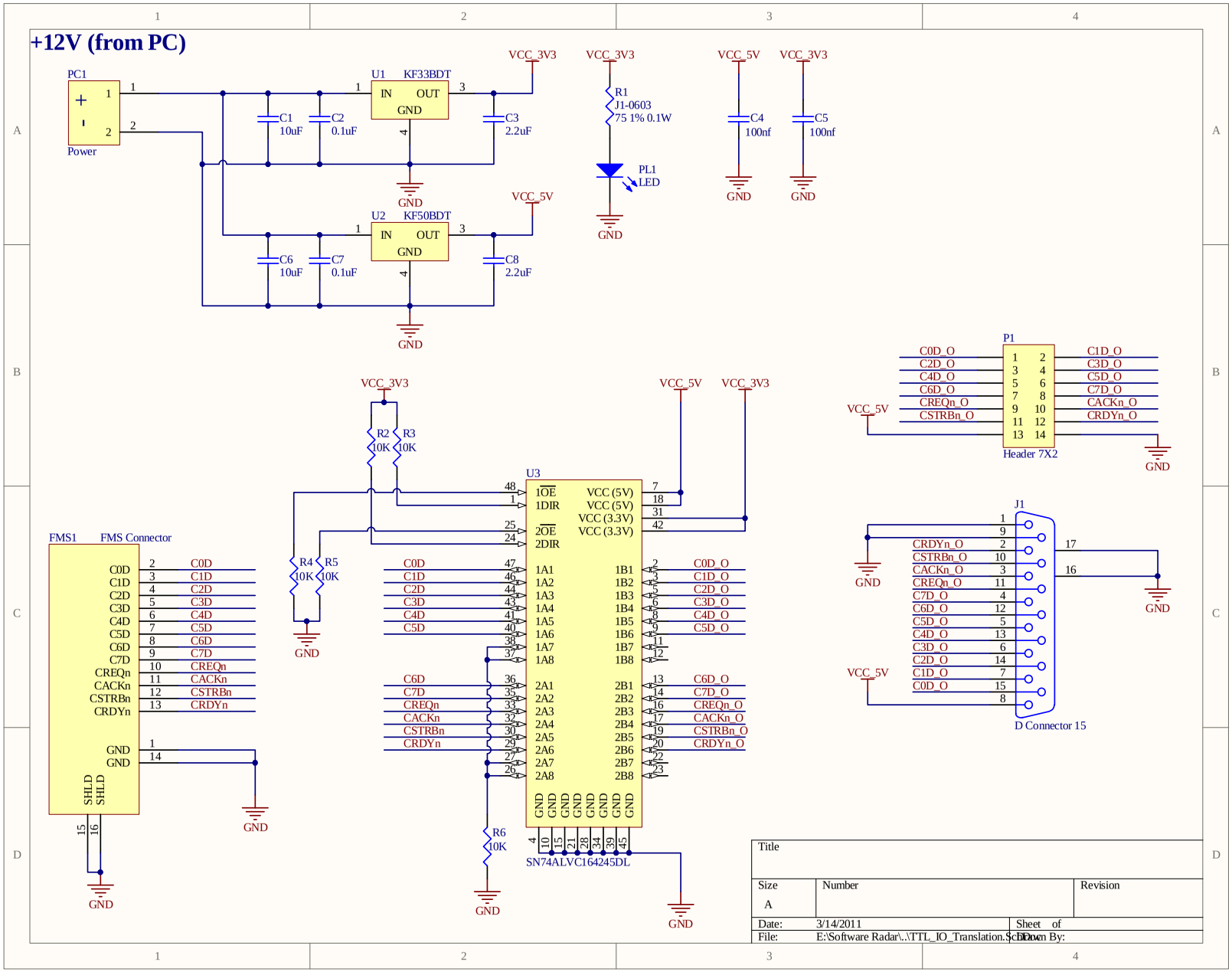

Figure A.5: Schematic of the printed circuit board used to buffer 12 bits of digital outputs from the SDR digital transceiver's transmitter FPGA. The input to the circuit is a flat FMS (ribbon) cable, while the output is a standard D-sub-15 connector.

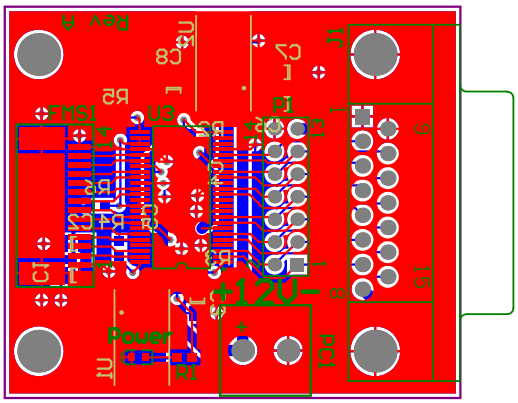

Figure A.6: Layout of the printed circuit board used to buffer 12 bits of digital outputs from the SDR digital transceiver's transmitter FPGA.

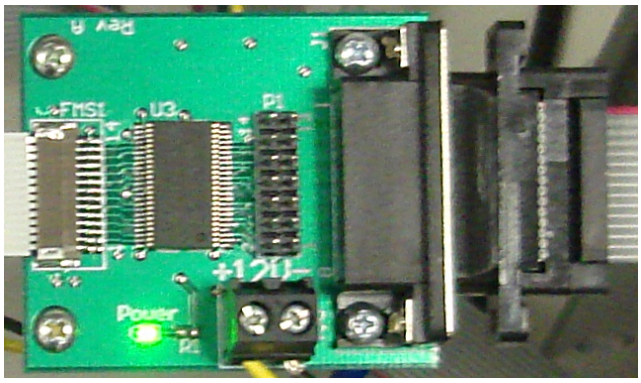

Figure A.7: Photo of the assembled digital output buffer. The SDR transceiver uses two of these for a total of 24 output bits.

A.3 Trigger Input Buffer and LVPECL Translator PCB

It is useful for some applications for the SDR to be able to respond to external trigger inputs. The SMT381 DAC module, connected to the SMT368A transmitter FPGA, has two LVPECL external trigger inputs. However, external trigger signals encountered in practice are typically TTL/LVTTL which is not directly compatible with the LVPECL standard. A schematic of the PCB is given in Fig. A.8. The PCB provides two independent TTL/LVTTL trigger inputs on standard SMA connectors and converts them to LVPECL using a LVTTL-to-LVPECL translator IC. A simple MOSFET circuit (described in [57]) is used on the inputs to ensure full compliance both TTL and LVTTL without damage to the translator IC. The 4-layer layout of the PCB sent for manufacture is shown in Fig. A.9, while the completed and assembled PCB is shown in Fig. A.10. This PCB is mounted inside the PC case with the digital transceiver and is powered using +12V from the PC's power supply.

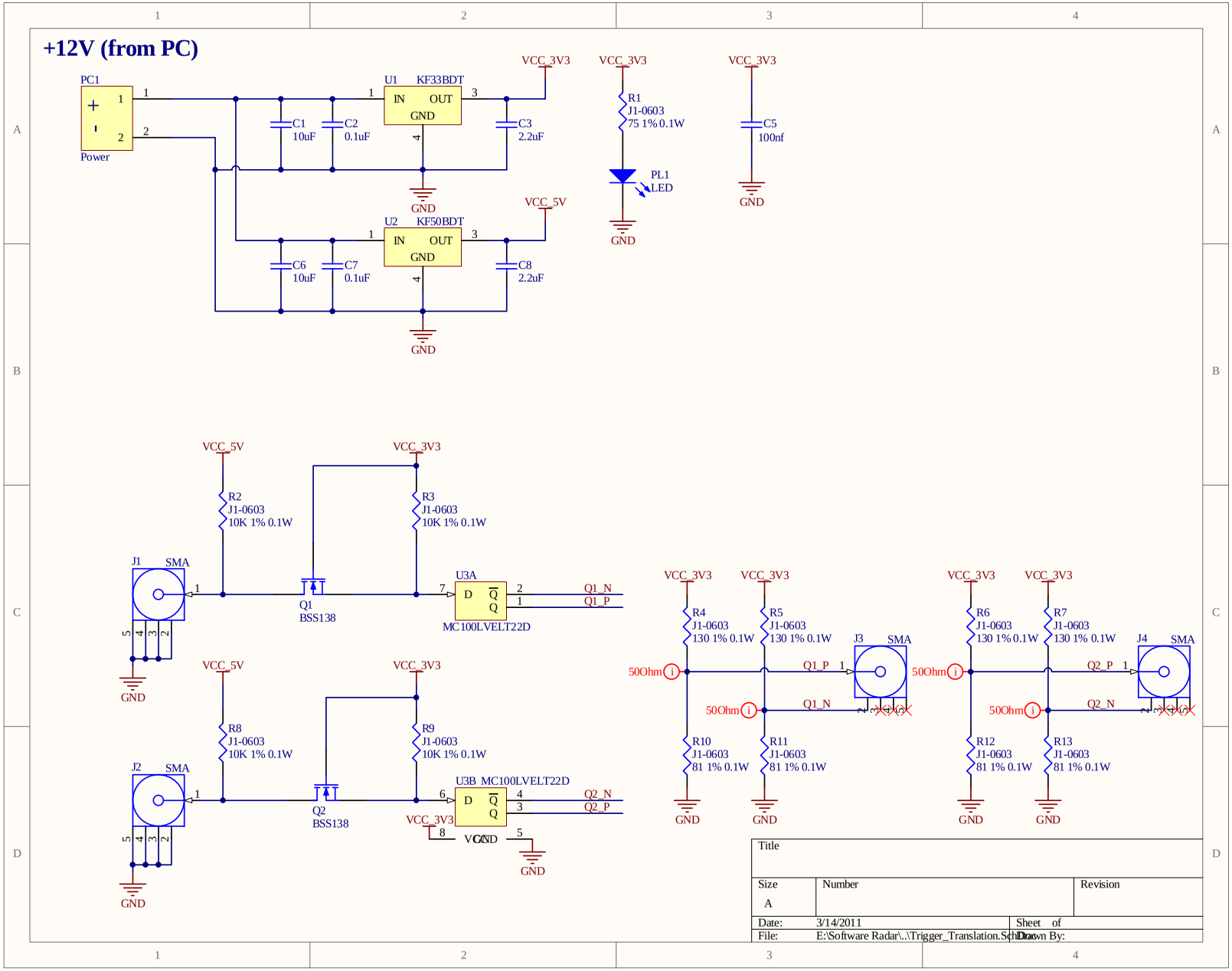

Figure A.8: Schematic of the printed circuit board used translate two incoming trigger signals (TTL/LVTTL) to LVPECL on an SMA cable suitable to be connected to the transmitter FPGA in the SDR digital transceiver.

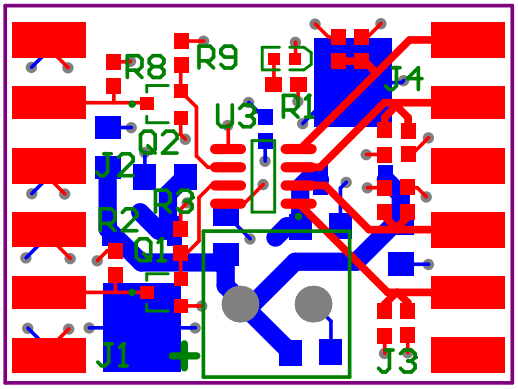

Figure A.9: Layout of the trigger input buffer printed circuit board.

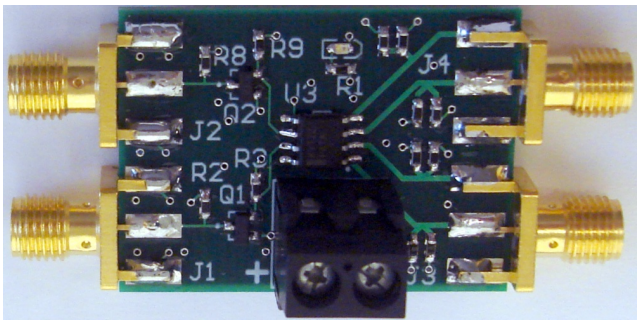

Figure A.10: Photo of the assembled trigger buffer. TTL/LVTTL inputs are on the left, LVPECL outputs are on the right.

A.4 RF Front End Control PCB

The RF front end control PCB serves two distinct purposes. First, it provides a clean way to route the 96 digital outputs from the SDR PC-controlled USB-DIO96H/50 device from *Measurement Computing* [34] to the four RF up- or down-converter boards using two 50-pin ribbon cable connectors as inputs and four 26-pin ribbon cable connectors as outputs, one for each up- or downconverter plate. Second, it decodes the 24 high speed digital outputs from the transmitter FPGA in the SDR to properly control the RF switches in the antenna switch matrix. Table A.12 lists all 24 of these signals along with the physical comport (CP1 or CP4) they are assigned to. As described previously, two *FPGA Digital Output Buffer* PCBs are used to convert the comport connectors to standard D-sub-15 connectors. Cables connect these to two corresponding D-sub-15 connectors on the RF front end control PCB, where they are are routed to an Altera Cyclone II FPGA module [58]. The table also lists the D-sub-15 pin assignments for all 24 signals.

The Altera FPGA contains only combinational logic required to form differential logic signals suitable for driving RF switches from the 24 high speed inputs. However, this FPGA operates with 3.3V LVTTL logic levels, whereas the RF switches require 5V TTL voltage levels. Therefore, level shifting transceiver ICs are required to convert LVTTL to TTL. All high speed control signals required to drive the antenna switch matrix (with the exception of the polarization switches) are routed to the fifth 26-pin ribbon cable connector. The antenna polarization control signals, along with 5V, +12V, and -12V voltages are routed to an eight-position modular 8P8C Ethernet jack. This jack is accessible through a rectangular hole in the custom RF enclosure's

backplate. In this manner, power and polarization switch control is sent over standard Cat-5E Ethernet cables to each antenna assembly.

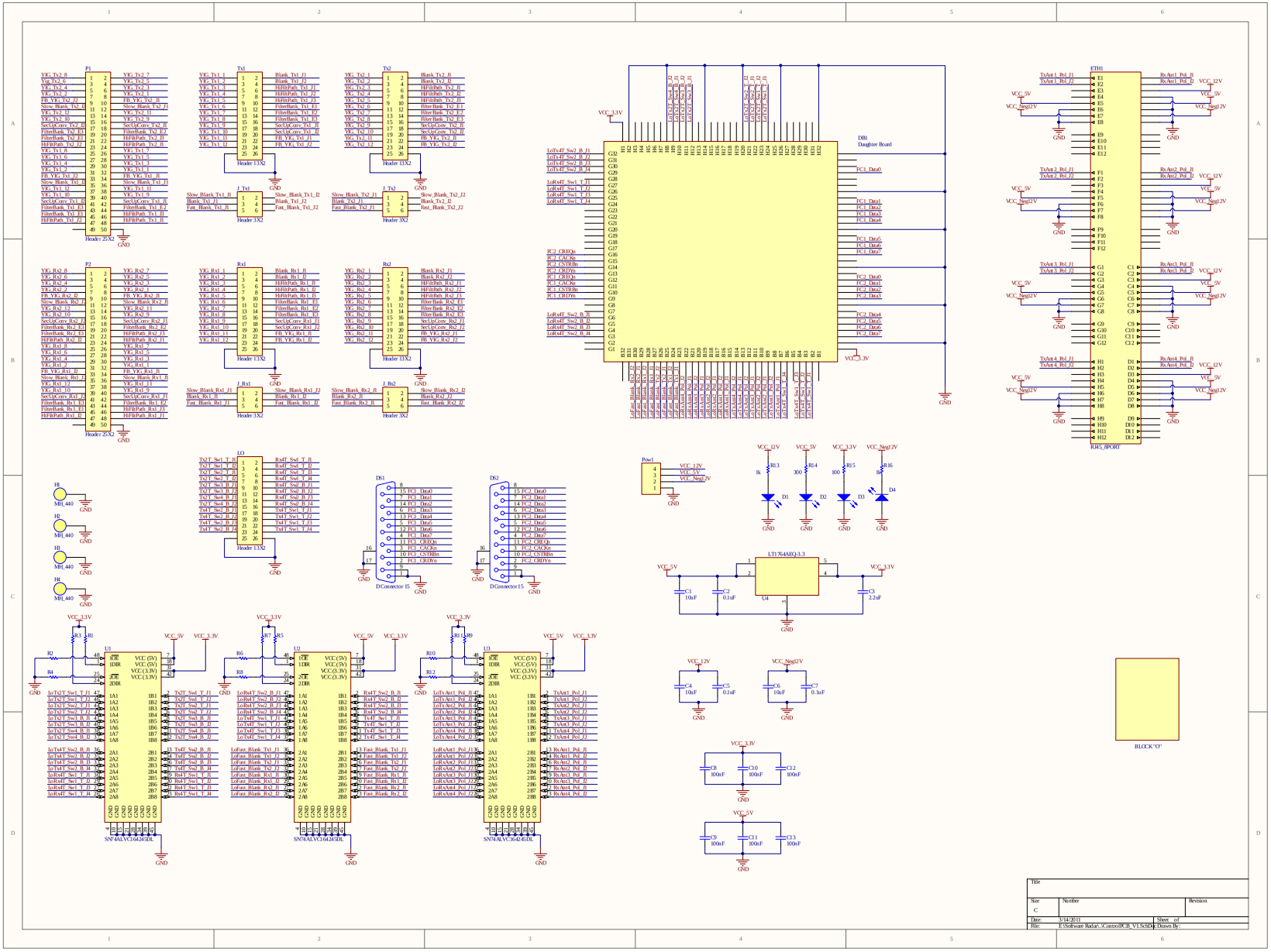

Figure A.11: Schematic of the custom PCB used to fan out control signals to each transmitter and receiver in the SDR's RF front end.

Figure A.12: Comport assignments of the high-speed antenna switch matrix signals along with the corresponding signal name on the *RF front end control PCB* schematic and *FPGA digital output buffer PCB* D-sub pin.

Signal Assignment:	Physical Comport:	Sundance Signal Name:	PCB Signal Name:	D-Sub Pin:
Fast_Blank_Tx1	CP4	Comport4_Data0	FC2_Data0	15
Fast_Blank_Tx2	CP4	Comport4_Data1	FC2_Data1	7
Fast_Blank_Rx1	CP4	Comport4_Data2	FC2_Data2	14
Fast_Blank_Rx2	CP4	Comport4_Data3	FC2_Data3	6
RxPolSel4	CP4	Comport4_Data4	FC2_Data4	13
RXPolSel3	CP4	Comport4_Data5	FC2_Data5	5
RxPolSel2	CP4	Comport4_Data6	FC2_Data6	12
RxPolSel1	CP4	Comport4_Data7	FC2_Data7	4
TxPolSel4	CP4	Comport4_NREQ	FC2_CREQn	11
TxPolSel3	CP4	Comport4_NACK	FC2_CACKn	3
TxPolSel2	CP4	Comport4_NSTRB	FC2_CSTRBn	10
TxPolSel1	CP4	Comport4_NRDY	FC2_CRDYn	2
TxChanSel4	CP1	Comport1_Data0	FC1_Data0	15
TxChanSel3	CP1	Comport1_Data1	FC1_Data1	7
TxChanSel2	CP1	Comport1_Data2	FC1_Data2	14
TxChanSel1	CP1	Comport1_Data3	FC2_Data3	6
Rx4PortB	CP1	Comport1_Data4	FC2_Data4	13
Rx4PortB	CP1	Comport1_Data5	FC2_Data5	5
Rx4PortA	CP1	Comport1_Data6	FC2_Data6	12
Rx4PortA	CP1	Comport1_Data7	FC2_Data7	4
Tx4PortB	CP1	Comport1_NREQ	FC2_CREQn	11
Tx4PortB	CP1	Comport1_NACK	FC2_CACKn	3
Tx4PortA	CP1	Comport1_NSTRB	FC2_CSTRBn	10
Tx4PortA	CP1	Comport1_NRDY	FC2_CRDYn	2

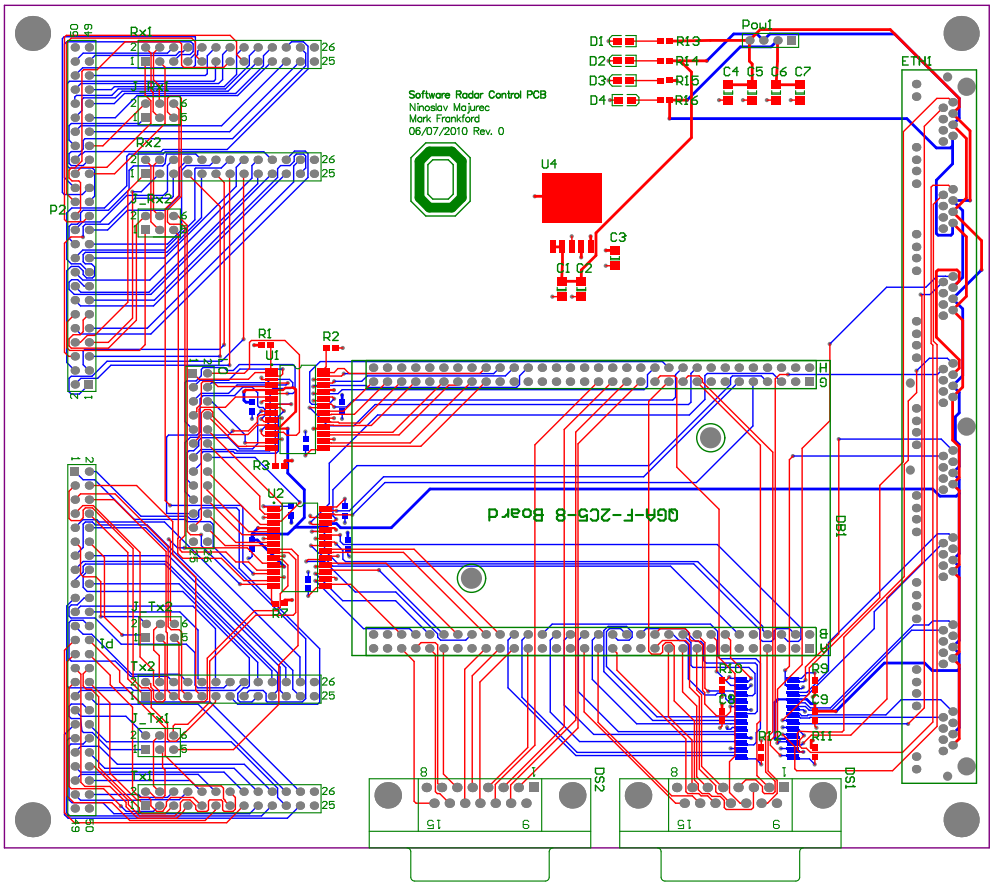

Figure A.13: Control PCB layout viewed from the top.

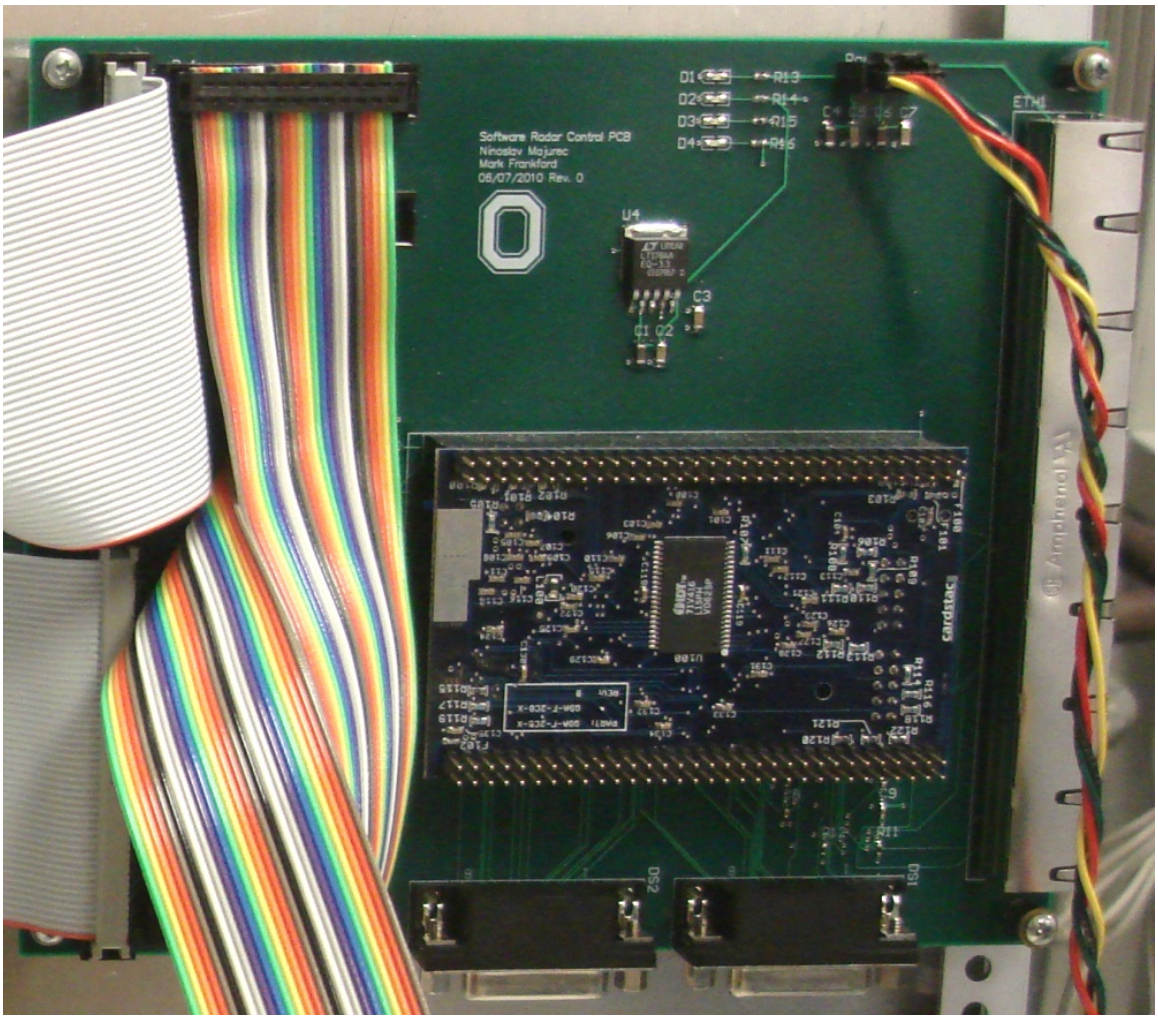

Figure A.14: Control PCB assembled and installed in the SDR front end. There are five rainbow ribbon cables, one for each plate in the custom RF enclosure. The eight-position modular 8P8C Ethernet jack is located along the right edge of the board.

APPENDIX B

EXPLORATION OF MIMO WAVEFORMS FOR IMAGING APPLICATIONS

For the purpose of forming MIMO virtual arrays using waveform diversity, it is useful to study the ability of a receiver to separate the time-domain scattered fields from multiple transmitters, particularly when scattering from a complex target. The complex target in this case occupies many range cells. Two different types of orthogonal transmit waveforms will be studied: those separated in frequency and those that occupy the same frequency band. These waveforms $s_m(t)$ have a finite bandwidth B which corresponds to a monostatic range resolution of $\frac{c}{2B}$ in meters, where c is the speed of light. A Monte Carlo simulation has been developed wherein the complex target is extended to occupy a large number of range cells such that $\Delta x = \Delta y >> \frac{c}{2B}$. The superposition of range returns from all transmitters is calculated at the receiver and the result is processed using matched filters for each waveform. The effectiveness of this procedure will be studied for different waveforms to analyze their applicability to various MIMO radar applications such as target detection and SAR imaging.

B.1 Received Signal Model

Given that the Fourier transform of the analytic baseband waveform $s_m(t)$ associated with the m^{th} transmitter is $S_m(f)$, the received signal at the n^{th} receiver after modulation and demodulation with a carrier frequency f_c can be written in the frequency domain as an integral over the area of the target as shown in (B.1).

$$R_{mn}(f) = \iint_{\Delta x \Delta y} S_m(f)\, e^{-j\left|\overrightarrow{r_m}(x,y)\right| k_c(f)} e^{-j\left|\overrightarrow{r_n}(x,y)\right| k_c(f)} \Sigma(x,y)\, dxdy \tag{B.1}$$

The two exponential terms in (B.1) account for the range to and from the target, where the vectors $\overrightarrow{r_m}(x,y)$ and $\overrightarrow{r_n}(x,y)$ are defined to point from transmitter m or receiver n respectively to each point on the target. $k_c(f)$ is the electromagnetic wavenumber of the bandpass signal, namely $k_c(f) = \frac{2\pi(f+f_c)}{c}$ where f_c is the center frequency of the radar. It should be noted here that no narrowband assumptions have been applied in calculating these phase shifts. $\Sigma(x,y)$ is the complex scattering coefficient defined for all points on the target, and it is assumed that the magnitude of $\Sigma(x,y)$ has been normalized such that the total "energy" of the target is unity regardless of its total size.

The total field $Y_n(f)$ in the frequency domain present at receiver n is the superposition of the fields due to all M receivers as shown.

$$Y_n(f) = \sum_{m=1}^{M} R_{mn}(f) \tag{B.2}$$

The time-domain result $y_n(t)$ is therefore the inverse Fourier transform of $Y_n(f)$. A matched filtering operation is then performed for each transmitted waveform to separate the returns resulting from each transmitter. The optimal matched filter in

the presence of white noise for the m^{th} transmitted waveform is given by [59].

$$h_m(t) = s_m^*(\tau - t) \tag{B.3}$$

where τ is the length of the transmitted pulse. The resulting pulse-compressed signals are the convolution of the received fields and the appropriate matched filter as shown.

$$f_{mn}(t) = \int_{-\infty}^{\infty} y_n(s) h_m(s-t) ds \tag{B.4}$$

Therefore, for a MIMO radar with M transmitters and N receivers, there are $M \times N$ pulse-compressed range returns $f_{mn}(t)$.

B.2 Discrete-Time Model for Monte Carlo Simulation

A discrete-time Monte Carlo simulation has been developed in Matlab which implements the received signal model outlined in the previous section for multiple realizations of a random target and additive white Gaussian noise. It is assumed that the MIMO radar modeled here utilizes digital transmitters and receivers with sampling frequency f_s and sample period $T = 1/f_s$ such that the maximum instantaneous bandwidth B of the transmitted and received signals is $f_s/2$. The discrete-time transmit waveforms for each transmitter are $s_m[p]$ where $p = t/T$ and have a fixed length $\tau = PT$. Each transmit pulse has been normalized such that the average power in each is

$$\frac{E}{M} = \frac{1}{P} \sum_{p=1}^{P} |s_m[p]|^2 \tag{B.5}$$

where E is the combined average power of all M transmitters. The SNR at receiver n can therefore be defined as

$$SNR = \frac{E}{\sigma_w^2} \tag{B.6}$$

where σ_w^2 is the variance of an additive complex white Gaussian noise vector $w_n[p]$ present in the receiver.

The complex target with an infinite number of scatterers defined over a continuous region with size $\Delta x \times \Delta y$ is broken up into a rectangular grid where each small area of the grid has the dimensions $dx \times dy$. The dimensions dx and dy are chosen such that they are much smaller than the shortest wavelength in the simulation, namely $\lambda_{min} = c/\left(f_c + f_s/2\right)$. A random complex scattering amplitude $A[x, y]$ is assigned to each discrete portion of the surface and a spatial filter based on the 2-D discrete Fourier transform (DFT) of Eq. (2.5) is applied to enforce the correlation between scatterers as a function of C_d. The resulting amplitudes are then normalized such that the sum of all scatterers in the discretized target is unity. The vectors $\overrightarrow{r_m}(x, y)$ and $\overrightarrow{r_n}(x, y)$ are calculated from the m^{th} transmitter to the center of each discrete scatterer, and from the center of each scatterer to the n^{th} receiver respectively.

The continuous-time received signal model in Eq. (B.1) is approximated by the discrete-time equation:

$$R_{mn}[k] = \sum_{[x,y]} S_m[k] e^{-j\left|\overrightarrow{r_m}(x,y)\right| k_c(f[k])} e^{-j\left|\overrightarrow{r_n}(x,y)\right| k_c(f[k])} A[x, y] \tag{B.7}$$

The double integrals have been replaced by a summation over all $[x, y]$, the coordinates of the centers of each discretized piece of the complex target. Furthermore, $S_m[k]$ is the DFT of $s_m[p]$ which has been zero-padded to length L, where L has been chosen such that it is large enough to prevent aliasing at the longest ranges expected in the simulation and also to allow for the entire target to be match-filtered. The frequency vector $f[k]$ here corresponds to the discretized baseband frequency vector shifted to the center frequency of operation, and is defined on the interval $(-f_s/2, f_s/2] + f_c$ with length L.

The discrete time-domain signal at receiver n with additive noise is computed by combining the sum of the inverse DFTs (IDFT) of $R_{mn}[k]$ with the Gaussian noise vector $w_n[p]$ as in Eq. (B.8).

$$y_n[p] = IDFT\left\{\left(\sum_{m=1}^{M} R_{mn}[k]\right)\right\} + w_n[p] \tag{B.8}$$

For the Monte Carlo simulation, $y_n[p]$ is calculated I times and is coherently averaged before being match-filtered using $h_m[p]$, a conjugated and order-reversed version of $s_m[p]$, resulting in $f_{mn}[p]$. This result will contain the wanted signal due to the m^{th} transmitted waveform as well as interference from both noise and non-zero contributions from the other waveforms. This can be quantified by the signal to interference-plus-noise ratio (SINR).

B.3 Monte Carlo Setup and Waveforms

The discrete-time Monte Carlo simulation of scattering from a complex target is performed for two classes of waveforms: those separated in frequency and those that occupy the same frequency band. While the simulation developed is capable of calculating the time-domain returns from multiple transmitters and receivers arbitrarily spaced around a two-dimensional target, a much simpler geometry will be utilized here. When a transmitter and receiver operate in a bistatic configuration, the range resolution achievable is dependent on the bistatic angle between them [60]. Larger bistatic scattering angles result in worse range resolution, such that targets must be further separated to be resolved. This affect would complicate the comparison of the various waveforms, so to avoid this, the MIMO geometry in Fig. B.1 is utilized. Here,

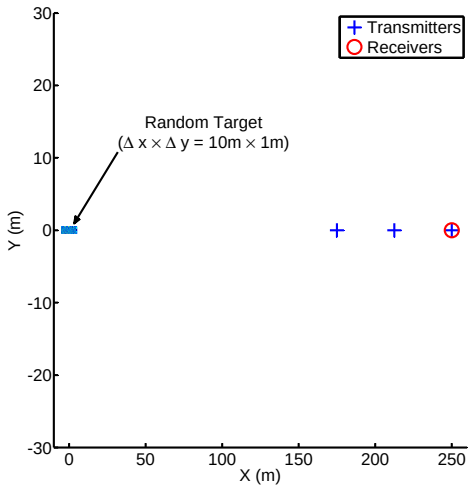

Figure B.1: Experimental pseudo-monostatic MIMO geometry.

the three transmitters and single receiver are configured in a pseudo-monostatic geometry where the bistatic angle between the receiver and various transmitters is 0°, but the target has different apparent ranges for each transmitter/receiver pair.

The apparent range of the target for each of the three pairs is the range from a virtual phase center located halfway between the transmitter and receiver locations. Table B.1 gives the locations of the transmit and receive elements along with the locations of the corresponding virtual phase centers. A complete listing of the rest of the parameters used in this simulation is given in Table B.2. The target is $10m \times 1m$ located at the origin and oriented along the x-axis. The scatterers which make up the target are assumed to be uncorrelated in this case, such that $C_d = 0m$.

Table B.1: Receiver, transmitters, and virtual phase center locations.

Label	Location (x,y) in Meters	Virtual Phase Center Location
Rx m=1	(250, 0)	
Tx n=1	(250, 0)	(250, 0)
Tx n=2	(212.5, 0)	(231.25, 0)
Tx n=3	(175, 0)	(212.5, 0)

Table B.2: Monte Carlo simulation parameters.

Symbol	Value	Description
M	2 or 3	Number of independent transmitters and orthogonal waveforms
N	1	Number of independent receivers
f_c	2 GHz	Center frequency
f_s	1 GSPS	Baseband sampling frequency ($1 * 10^9$ samples-per-second)
B	500 MHz	Instantaneous bandwidth ($= f_s/2$)
T	1 ns	Sample period ($1/f_s$)
τ	1 us	Pulse length
P	1000 samples	Number of samples in each transmit pulse
λ_{min}	0.12 m	Shortest wavelength corresponding to maximum frequency of $f_c + B/2$
$dx = dy$	0.024 m	Target discretization
Δx	10 m	Target Size: X dimension
Δy	1 m	Target Size: Y dimension
C_d	0 m	Correlation distance
SNR	30 dB	Signal-to-noise ratio
I	100	Number of Monte Carlo iterations coherently averaged

B.3.1 Waveforms Separated in Frequency

Ideal MIMO waveforms have a single narrow peak in their autocorrelation function which implies that the waveforms pulse-compress well, while low cross-correlations between waveforms ensure that separate waveforms do not interfere with each other after pulse-compression when received simultaneously. "Orthogonal" waveforms are those which are deemed to have sufficiently small cross-correlations. The cross-correlation of two discrete waveforms is defined as [59]

$$\rho_{ab}[q] = \sum_{p=-\infty}^{\infty} s_a[p] s_b^*[p+q] \tag{B.9}$$

with an identical definition for the autocorrelation when $a = b$. Equation (B.9) can also be written in in the frequency domain as [7]

$$\rho_{ab}[q] = \int_{-\infty}^{\infty} S_a(\omega) S_b^*(\omega) e^{i\omega q} \frac{d\omega}{2\pi} \tag{B.10}$$

where $S_a(\omega)$ and $S_b(\omega)$ are the discrete-time Fourier transforms (DTFT) of the deterministic sequences $s_a[q]$ and $s_b[q]$ respectively. Clearly, if $S_a(\omega)$ and $S_b(\omega)$ can be defined to be non-zero only on disjoint frequency bands, the resulting cross-correlation between the two waveforms can be made to be zero. The linear frequency modulated (LFM), or chirp, waveforms studied here utilize this fact to achieve very small cross-correlations.

LFM waveforms have the simple analytic form [61]:

$$s(t) = exp\left(j\pi\left[2f_{start}t + Kt^2\right]\right), 0 \leq t \leq \tau \tag{B.11}$$

The starting frequency of the chirp is defined as f_{start}, and the variable $K = B_{chirp}/\tau$ is the chirp rate where B_{chirp} is the total bandwidth of the chirp. If it is assumed that

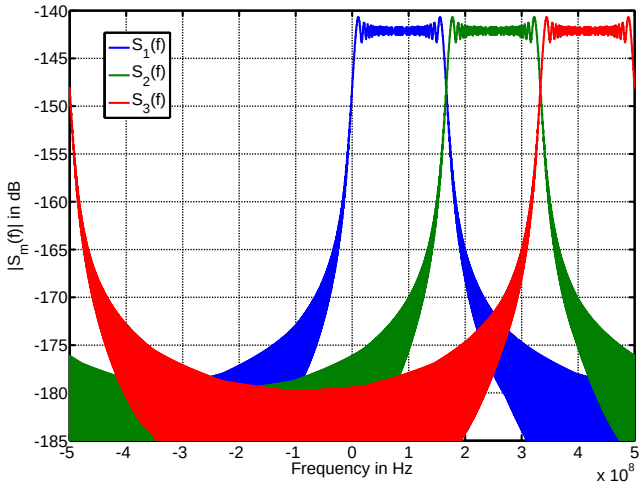

Figure B.2: DFTs of three LFM chirp waveforms in the frequency domain

the receiver has a bandwidth B and M orthogonal chirps are required, each must have $B_{chirp} \leq B/M$ to ensure orthogonality between the M waveforms, with f_{start} being staggered by B/M for each waveform.

An example of $M = 3$ LFM waveforms, each having a bandwidth of $500MHz/3 = 166.7MHz$, is shown in the frequency domain in Fig. B.2. Utilizing a Hamming window, the autocorrelation and cross-correlations of each of the waveforms with the others are given in Fig. B.3. Clearly, the LFM chirp waveform in conjunction with a Hamming window has desirable autocorrelation properties with a narrow peak located at time lag zero and very small side lobes. The maximum cross-correlation between waveforms for the simulation parameters chosen is better than 45 dB below the peak of the autocorrelation, which is expected as the three waveforms occupy primarily disjoint spectra.

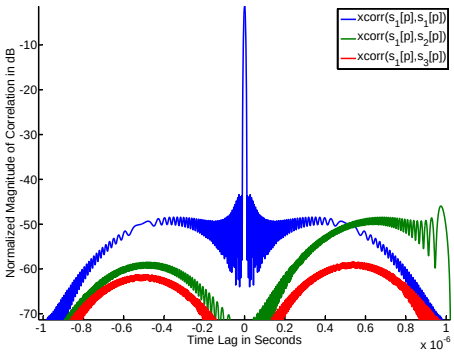

(a) LFM Waveform 1

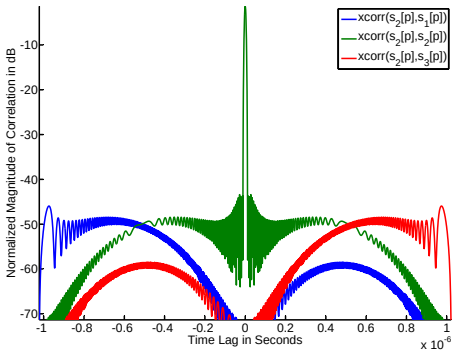

(b) LFM Waveform 2

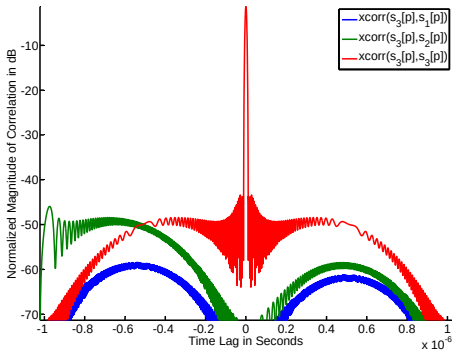

(c) LFM Waveform 3

Figure B.3: Auto- and cross-correlations of three LFM chirp waveforms which are separated in frequency.

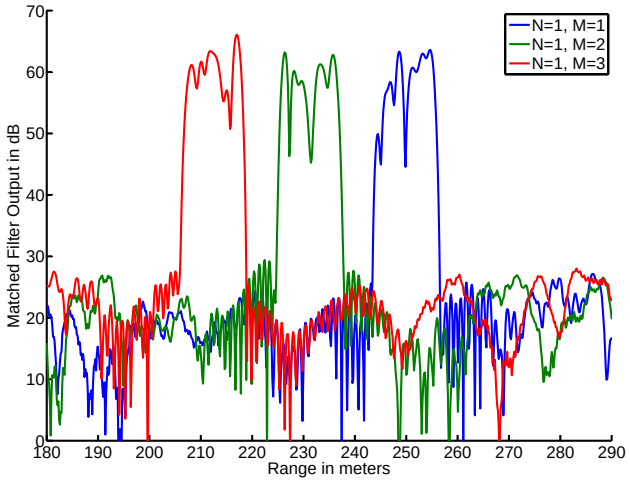

Figure B.4: Matched-filter responses $f_{m1}[p]$ for three LFM chirp waveforms versus range in meters.

The pulse-compressed waveforms $f_{m1}[p]$ have been calculated using the method described above for $M = 3$ transmitter locations. Recall that this involves passing the superposition of the returns from all three transmitters through matched filters. The magnitude of the result in dB is given in Fig. B.4. The 10m-length target at the origin is clearly present at all three ranges corresponding to the virtual phase centers in Table B.1.

An important result from Fig. B.4 is that the magnitude of the range response from the target is different for each transmitted waveform. While the cross-correlations between the transmitted waveforms are non-zero, they are very small and are better than 45 dB below the maximum pulse compression gain. While not shown here, it has been verified that the cross-correlations are not the cause of this behavior by studying the returns for each waveform separately at the receiver without the presence

of the other two waveforms and observing the same variation in the range responses. Instead, the variations in the range responses can be attributed to the waveforms themselves. Since the three transmitted waveforms occupy different frequency bands, the scattered field due to each point in the distributed complex target exhibits a different phase shift at the receiver for each waveform. The fields then interfere differently resulting in non-uniform range returns across different waveforms. The next section introduces two new sets of waveforms which occupy the same frequency bands and have the potential to mitigate this effect.

B.3.2 Waveforms with Same Frequency Band

As opposed to the LFM waveforms in separate frequency bands presented in the previous section, the waveforms in this section occupy the same frequencies. These waveforms will be analyzed for the full bandwidth of 500 MHz and a limited bandwidth of B=166.7 MHz for comparison to the orthogonal LFM waveforms.

The first waveform to be presented is based on random phase noise. It's DFT has the form:

$$S_m[k] = \begin{cases} Ae^{j\phi[k]} & , \quad 0 \leq \frac{2\pi k f_s}{P} \leq B \\ 0 & , \quad elsewhere \end{cases} \tag{B.12}$$

The amplitude A is constant versus frequency, while the phase term ϕ is a random vector whose independent entries have a uniform distribution such that $\phi[k] \sim U(0, 2\pi)$. Three realizations of the DFT of the noise waveform for $A = 1$ are shown in Fig. B.5 for B=166.7 MHz and in Fig. B.6 for B=500 MHz. An IDFT is utilized to calculate the time domain samples of the corresponding transmit waveforms, and they are normalized to have the same energy E/M.

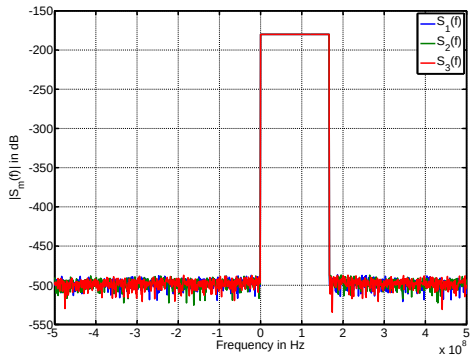

(a) DFT Magnitude

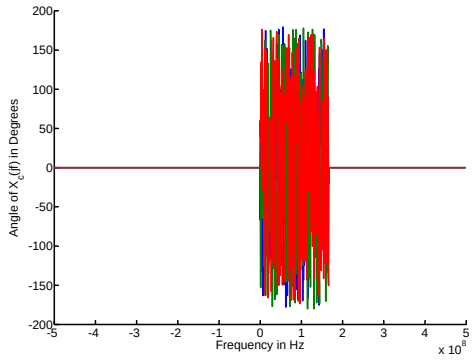

(b) DFT Phase

Figure B.5: DFTs of three noise waveforms in the frequency domain with bandwidths of 166.7 MHz

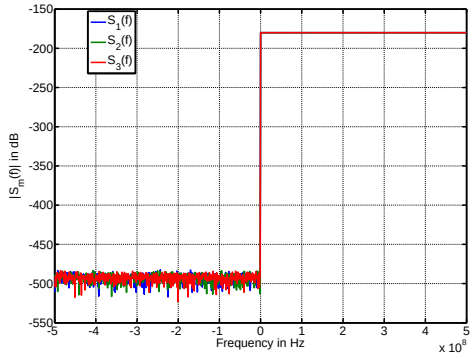

(a) DFT Magnitude

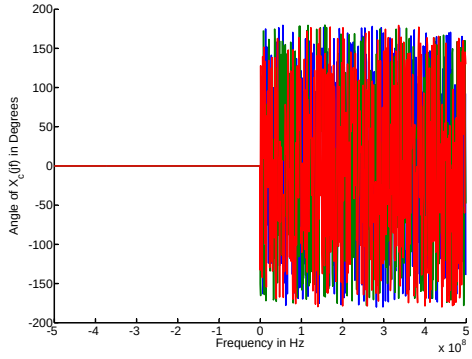

(b) DFT Phase

Figure B.6: DFTs of three noise waveforms in the frequency domain with bandwidths of 500 MHz

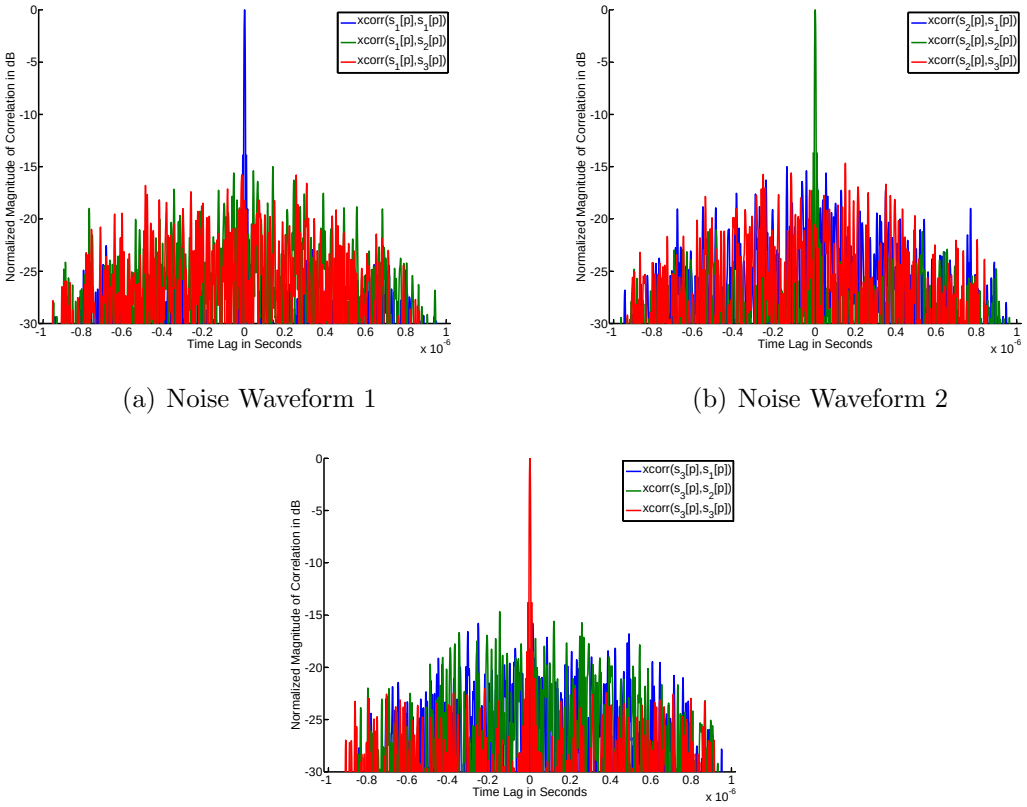

(a) Noise Waveform 1

(b) Noise Waveform 2

(c) Noise Waveform 3

Figure B.7: Auto- and cross-correlations of three phase-noise waveforms with bandwidths of 166.7 MHz.

The waveforms $S_m[k]$ for $m = 1$ to M are not orthogonal. However, they do exhibit a narrow autocorrelation function and cross-correlation levels of -15 and -20 dB below the main peak for the simulation parameters utilized (P=1000 samples, B=166.7 MHz or 500 MHz respectively). These properties are illustrated in Figs. B.7 and B.8. It should be noted that the cross-correlation between the noise waveforms can be decreased by increasing the time-bandwidth product τB. However, a reasonable pulse length is assumed here for fixed B.

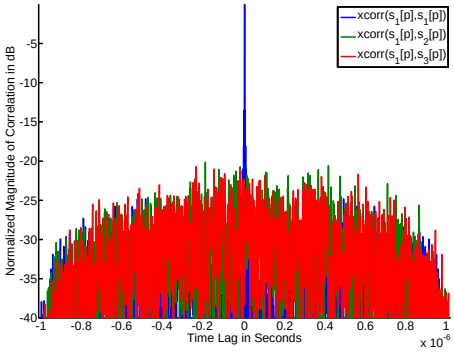

(a) Noise Waveform 1

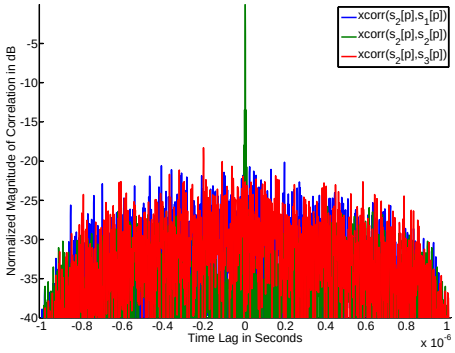

(b) Noise Waveform 2

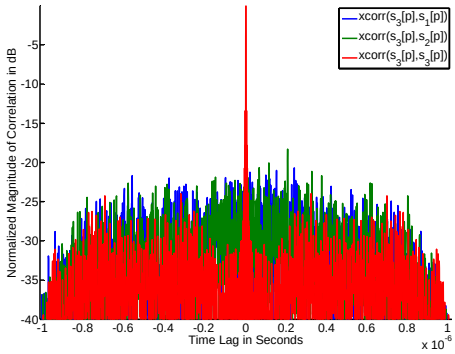

(c) Noise Waveform 3

Figure B.8: Auto- and cross-correlations of three noise waveforms with bandwidths of 500 MHz.

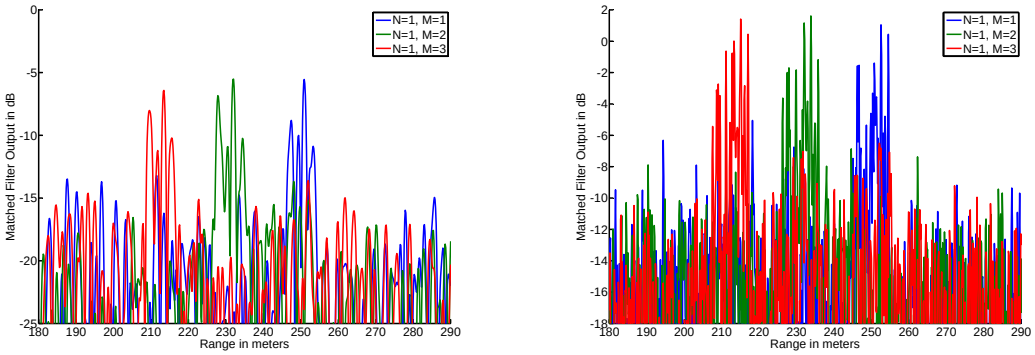

(a) One-third Bandwidth

(b) Full Bandwidth

Figure B.9: Match-filter responses $f_{m1}[p]$ for three random noise waveforms.

As was done previously, the pulse-compressed waveforms $f_{m1}[p]$ are computed to test the receiver's ability to separate the three noise waveforms. The results are given in Fig. B.9 for both bandwidths. In both cases, the range responses for all three waveforms are similar. If the waveforms are processed separately (not shown here), the target response is nearly identical for all three waveforms. However, interference primarily due to correlations between the waveforms has a much greater effect than in the orthogonal LFM case presented previously. Here, the target is only 5-10 dB above the noise and interference. One advantage of the noise waveform though is that the increased bandwidth improves the range resolution by a factor of M over the orthogonal LFM case.

A second group of LFM waveforms is presented in this section which is only possible for $M = 2$. These waveforms are the up- and downward chirping LFM signals which are defined in the time domain as

$$s_1(t) = exp\left(j\pi\left[Kt^2\right]\right), 0 \leq t \leq \tau \tag{B.13}$$

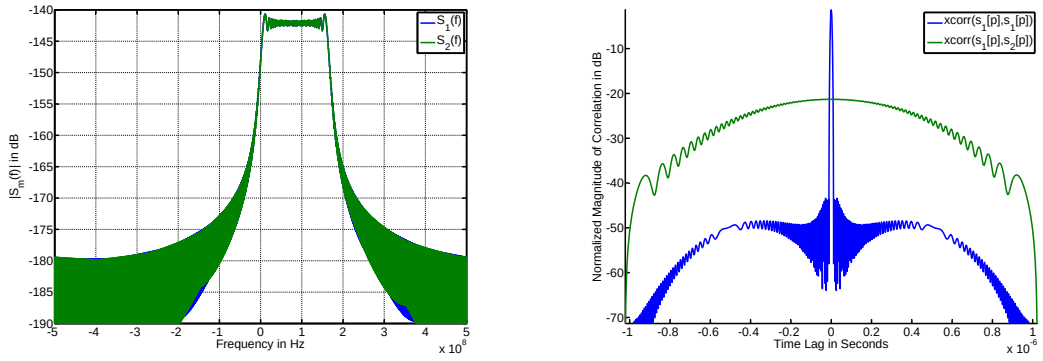

(a) Frequency domain

(b) Cross-correlations

Figure B.10: Frequency domain and cross-correlations of two chirps: one with positive (up) K and one with negative (down) K, and a total bandwidth of 166.7 MHz.

and

$$s_2(t) = exp\left(j\pi\left[2B_{chirp}t - Kt^2\right]\right), 0 \leq t \leq \tau \tag{B.14}$$

for the up- and downward chirps respectively.

The DFTs of both the up and down chirps are presented in Fig. B.10(a) for B=166.7 MHz. The magnitudes are identical to each other and to the first waveform in Fig. B.2. The auto- and cross-correlations of the two chirps are given in Fig. B.10(b), also for 166.7 MHz bandwidth. It is not surprising that the autocorrelation function is the same as those in Fig. B.3. However, the cross-correlation is significantly different. Without a Hamming window, the cross-correlation would be nearly flat at approximately -25 dB below the autocorrelation peak. With the Hamming window, as is shown in the figure, the maximum cross-correlation is approximately -21 dB but rolls off for larger time lags. Figs. B.11(a) and B.11(b) show this same behavior for chirps with 500 MHz bandwidth. In this case, the maximum cross-correlation is -26 dB.

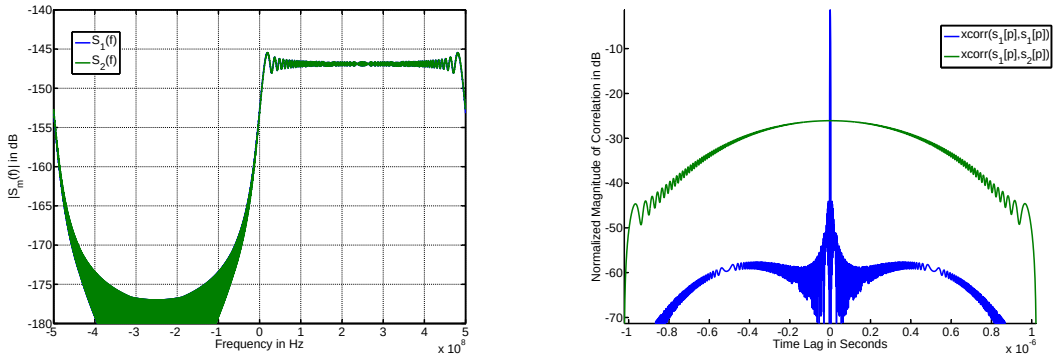

(a) Frequency domain

(b) Cross-correlations

Figure B.11: Frequency domain and cross-correlations of two chirps: one with positive (up) K and one with negative (down) K, and a total bandwidth of 500 MHz.

The two separated range returns are given in Fig. B.12 for both bandwidths. The matched filters perform similarly to those of the noise waveforms in terms of rejecting interference from other waveforms. This is expected as the maximum cross-correlation levels were similar for both sets of waveforms. Again, the range returns for both are similar, with differences being primarily the result of interference due to non-zero cross-correlations between the waveforms.

B.4 Discussion

The simulation parameters in Table B.2 were chosen to be achievable by a real-world radar system. A 500 MHz instantaneous bandwidth yields a downrange resolution of approximately 0.3 m. The target is 10 m in length and therefore occupies 30 range bins, enough to model variations in the target range response. With a center frequency of 2 GHz, the shortest wavelength is $c/(2.5GHz)$ or 0.12 m. The target was discretized such that the smallest scatterer is one fifth of a wavelength on a side

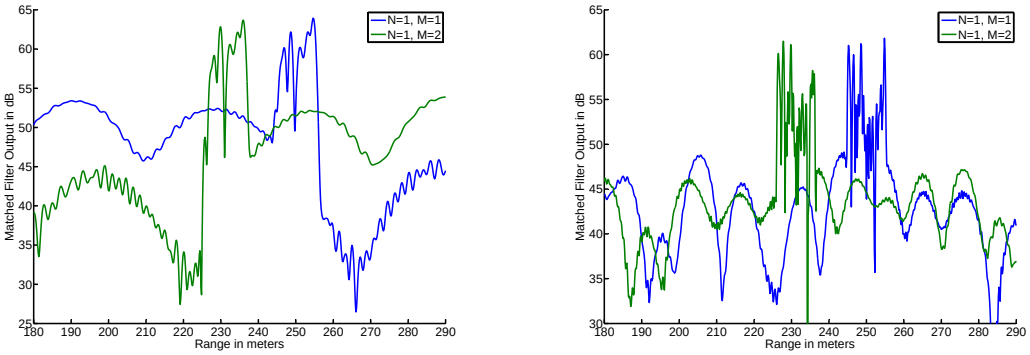

(a) One-third Bandwidth

(b) Full Bandwidth

Figure B.12: Match-filter responses $f_{m1}[p]$ for two up-down LFM chirp waveforms.

to ensure that the target fading in range would be modeled accurately. The complex amplitudes of the scatterers were uncorrelated ($C_d = 0$), and the same random realizations of the complex target were utilized for all waveform simulations presented in the previous section.

While the simulated measurements of a complex target presented here were corrupted by additive white Gaussian noise, the SNR was quite high at 30dB. This was deliberate such that the performance of the matched filtering for each set of waveforms was primarily limited by interference due to cross-correlations between waveforms, not additive noise. It was shown that waveforms which occupy disjoint frequency bands have good cross-correlation properties and therefore exhibit higher SINRs after matched filtering. However, the target model consists of many scatterers located at different ranges, and the interference of these scatterers with one another is frequency dependent. Therefore, the range returns for waveforms with disjoint frequency support are not identical, even if interference from simultaneously transmitted

waveforms is not included in the calculation. While this may not be critical for some applications, it may be important for other applications where the MN returns need to be processed jointly, such as synthetic aperture radar (SAR) imaging and target parameter estimation. In an attempt to generate waveforms with identical support in frequency, it was found that the cross-correlation of these waveforms was less than ideal. This is inherent in Eq. (B.10) which implies that it is impossible for two waveforms to occupy the same frequency bands and still have zero cross-correlation [7]. Therefore, a trade off in waveform design can be made between waveforms which have the same frequency support and therefore have similar range returns and waveforms which have better cross-correlation statistics.

Of the three waveform types presented, the noise based waveform is the only one which has the same frequency support for all waveforms and is extendable to $M > 2$. It should also be noted that the cross-correlation can be increased for a fixed bandwidth $f_s/2$ by increasing the length of the pulse. Fig. B.13 shows the average maximum cross-correlation of two noise waveforms in dB versus pulse length. Doubling the pulse length only decreases the cross-correlation by approximately 3 dB, so it is clear that the cross-correlation achievable will be limited by reasonable pulse lengths for a particular application.

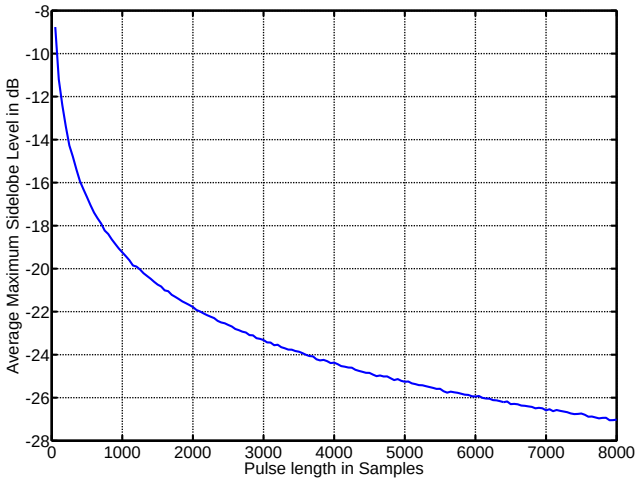

Figure B.13: Average maximum cross-correlation level versus pulse length in samples for the noise waveforms.

BIBLIOGRAPHY

[1] J. Klare. Digital beamforming for a 3D MIMO SAR - improvements through frequency and waveform diversity. *Geoscience and Remote Sensing Symposium, 2008. IGARSS 2008. IEEE International*, 5:V –17 –V –20, July 2008.

[2] M. Weib and J. Ender. A 3D imaging radar for small unmanned airplanes - ARTINO. *Radar Conference, 2005. EURAD 2005. European*, pages 209 –212, October 2005.

[3] J. Klare, M. Weiss, O. Peters, A. Brenner, and J. Ender. ARTINO: A new high resolution 3D imaging radar system on an autonomous airborne platform. *Geoscience and Remote Sensing Symposium, 2006. IGARSS 2006. IEEE International Conference on*, pages 3842 –3845, August 2006.

[4] D. W. Bliss, K. W. Forsythe, S. K. Davis, G. S. Fawcett, D. J. Rabideau, L. L. Horowitz, and S. Kraut. GMTI MIMO radar. In *Waveform Diversity and Design Conference, 2009 International*, pages 118 –122, February 2009.

[5] Jian Li, P. Stoica, and Xumin Zhu. MIMO radar waveform synthesis. *Radar Conference, 2008 IEEE*, pages 1 –6, May 2008.

[6] C.M. Teixeira. Performance bounds on MIMO radar with optimized coded constant modulus waveforms. In *Radar Conference, 2010 IEEE*, pages 304 –309, May 2010.

[7] K. W. Forsythe and D. W. Bliss. MIMO radar waveform constraints for GMTI. *Selected Topics in Signal Processing, IEEE Journal of*, 4(1):21 –32, February 2010.

[8] Chen Duofang, Chen Baixiao, and Zhang Shouhong. Multiple-input multiple-output radar and sparse array synthetic impulse and aperture radar. *Radar, 2006. CIE '06. International Conference on*, pages 1–4, October 2006.

[9] Chen Baixiao, Zhang Shouhong, Wang Yajun, and Wang Jun. Analysis and experimental results on sparse-array synthetic impulse and aperture radar. *Radar, 2001 CIE International Conference on, Proceedings*, pages 76–80, 2001.

[10] Chen Baixiao, Liu Hongliang, and Zhang Shouhong. Long-time coherent integration based on sparse-array synthetic impulse and aperture radar. *Radar, 2001 CIE International Conference on, Proceedings*, pages 1062–1066, 2001.

[11] E. Fishler, A. Haimovich, R. Blum, L. Cimini, D. Chizhik, and R. Valenzuela. Spatial diversity in radars-models and detection performance. *Signal Processing, IEEE Transactions on [see also Acoustics, Speech, and Signal Processing, IEEE Transactions on]*, 54(3):823–838, March 2006.

[12] E. Fishler, A. Haimovich, R. Blum, D. Chizhik, L. Cimini, and R. Valenzuela. MIMO radar: an idea whose time has come. *Radar Conference, 2004. Proceedings of the IEEE*, pages 71–78, April 2004.

[13] E. Fishler, A. Haimovich, R. Blum, L. Cimini, D. Chizhik, and R. Valenzuela. Performance of MIMO radar systems: advantages of angular diversity. *Signals, Systems and Computers, 2004. Conference Record of the Thirty-Eighth Asilomar Conference on*, 1:305–309, November 2004.

[14] D.J. Rabideau and P. Parker. Ubiquitous MIMO multifunction digital array radar. In *Signals, Systems and Computers, 2003. Conference Record of the Thirty-Seventh Asilomar Conference on*, volume 1, pages 1057–1064, November 2003.

[15] D.R. Kirk, J.S. Bergin, P.M. Techau, and J.E. Don Carlos. Multi-static coherent sparse aperture approach to precision target detection and engagement. *Radar Conference, 2005 IEEE International*, pages 579–584, May 2005.

[16] Nikolaus H. Lehmann, Alexander M. Haimovich, Rick S. Blum, and Len Cimini. High resolution capabilities of MIMO radar. *Signals, Systems and Computers, 2006. ACSSC '06. Fortieth Asilomar Conference on*, pages 25–30, October-November 2006.

[17] Chaoran Du, John S. Thompson, and Yvan Petillot. Predicted detection performance of MIMO radar. *Signal Processing Letters, IEEE*, 15:83–86, 2008.

[18] D. R. Fuhrmann and J. VanderLaan. Detection of complex point targets in a MIMO radar system with distributed assets and partially correlated signals. In *Radar Conference, 2010 IEEE*, pages 1134 –1139, May 2010.

[19] Jerome I. Glaser. Bistatic RCS of complex objects near forward scatter. *Aerospace and Electronic Systems, IEEE Transactions on*, AES-21(1):70 –78, January 1985.

[20] Y. S. Chesnokov and M. V. Krutikov. Bistatic RCS of aircrafts at the forward scattering. In *Radar, 1996. Proceedings., CIE International Conference of*, pages 156 –159, October 1996.

[21] Mark T. Frankford, Joel T. Johnson, and Emre Ertin. Including spatial correlations in the statistical MIMO radar target model. *Signal Processing Letters, IEEE*, 17(6):575–578, June 2010.

[22] M. T. Frankford and J. T. Johnson. Predictions of the spatially correlated statistical MIMO radar target model. In *Proc. URSI National Radio Science Meeting*, January 2010.

[23] I.S. Gradshteyn and I.M. Ryzhik. *Table of Integrals, Series, and Products*, chapter 3, 8, pages 333, 880. Academic Press, 6th edition, 2000.

[24] H. Vincent Poor. *An Introduction to Signal Detection and Estimation*. Springer-Verlag, 2nd edition, 1994.

[25] Merrill I. Skolnik. *Radar Handbook*, chapter 8, pages 8.3–8.36. McGraw-Hill, 3rd edition, 2008.

[26] Merrill I. Skolnik. *Introduction to Radar Systems*. McGraw-Hill, New York, 3rd edition, 1989.

[27] Mark A. Richards, James A. Scheer, and William A. Holm, editors. *Principles of Modern Radar*, volume I: Basic Principles. SciTech Publishing, 2010.

[28] *TIM-40 MODULE SPECIFICATION Including TMS320C44 Addendum*. available online at `http://www.sundance.com/docs/TIM_Spec_v1_12.pdf`. Version 1.12.

[29] *SMT Comm-port Buffering*. available online at `ftp://ftp2.sundance.com/Pub/documentation/pdf-files/comm-port.pdf`. Revision 1.06.

[30] *Specifications of the Sundance High-speed Bus Standard*. available online at `http://www.sundance.com/Docs/SHB%20Technical%20Specification.pdf`. Revision 5.1.

[31] *Sundance Multiprocessor Technology Ltd.* available online at `http://www.sundance.com/`, 2011.

[32] J. Langley, P. Hall, and P. Newham. Balanced antipodal vivaldi antenna for wide bandwidth phased arrays. *Microwaves, Antennas and Propagation, IEE Proceedings*, 143(2):97 –102, April 1996.

[33] E. Gazit. Improved design of the vivaldi antenna. *Microwaves, Antennas and Propagation, IEE Proceedings H*, 135(2):89 – 92, April 1988.

[34] *Measurement Computing*. available online at `http://www.mccdaq.com`, 2011.

[35] *3L Diamond*. available online at `http://www.3l.com/what-is-3l-diamond`, 2011.

[36] Johnson M. Hart. *Windows System Programming*. Addison-Wesley Professional, 4th edition, February 2010.

[37] J. M. P. Langlois, D. Al-Khalili, and R. J. Inkol. Polyphase filter approach for high performance, FPGA-based quadrature demodulation. *J. VLSI Signal Process. Syst.*, 32(3):237–254, 2002.

[38] *Atmel Dual 8-bit 1 Gsps ADC - AT84AD001B Smart ADC*. available online at `http://www.atmel.com/dyn/resources/prod_documents/doc2153E.pdf`, 2006.

[39] *MLB Bat 3 UAV Brochure*. available online at `http://www.spyplanes.com/pdf_new/bat3_brochure.pdf`, 2011.

[40] Donald Barrick, Clarence Krichbaum, George T. Ruck, and William Stuart. *Radar Cross Section Handbook*. Plenum Press, 1970.

[41] A. Currie and M. A. Brown. Wide-swath SAR. *Radar and Signal Processing, IEEE Proceedings*, 139(2):122–135, April 1992.

[42] G. Krieger, N. Gebert, and A. Moreira. Unambiguous SAR signal reconstruction from nonuniform displaced phase center sampling. *Geoscience and Remote Sensing Letters, IEEE*, 1(4):260–264, October 2004.

[43] O. Arikan and D. C. Munson, Jr. Analysis and simulation of a new algorithm for spotlight-mode synthetic aperture radar. *Acoustics, Speech, and Signal Processing, 1989. ICASSP-89., 1989 International Conference on*, pages 1453 –1455, May 1989.

[44] M. Suess, B. Grafmueller, and R. Zahn. A novel high resolution, wide swath SAR system. *Geoscience and Remote Sensing Symposium, 2001. IGARSS '01. IEEE 2001 International*, 3(3):1013 –1015, 2001.

[45] R. K. Moore, J. P. Claassen, and Y. H. Lin. Scanning spaceborne synthetic aperture radar with integrated radiometer. *Aerospace and Electronic Systems, IEEE Transactions on*, AES-17(3):410 –421, May 1981.

[46] M. Younis, C. Fischer, and W. Wiesbeck. Digital beamforming in SAR systems. *Geoscience and Remote Sensing, IEEE Transactions on*, 41(7):1735 – 1739, July 2003.

[47] G. Krieger, N. Gebert, and A. Moreira. Multidimensional waveform encoding: A new digital beamforming technique for synthetic aperture radar remote sensing. *Geoscience and Remote Sensing, IEEE Transactions on*, 46(1):31–46, January 2008.

[48] Constantine A. Balanis. *Antenna Theory: Analysis and Design*. John Wiley & Sons, Inc., 2nd edition, 1997.

[49] Dean L. Mensa. *High Resolution Radar Cross-Section Imaging*. Artech House, 2nd edition, 1991.

[50] Jr. J. W. Crispin and K. M. Siegel. *Methods of radar cross-section analysis*. Academic Press, 1969.

[51] C. J. Bradley, P. J. Collins, D. G. Falconer, J. Fortuny-Guasch, and A. J. Terzuoli. Evaluation of a near-field monostatic-to-bistatic equivalence theorem. *Geoscience and Remote Sensing, IEEE Transactions on*, 46(2):449 –457, February 2008.

[52] R. E. Kell. On the derivation of bistatic RCS from monostatic measurements. *Proceedings of the IEEE*, 53(8):983 – 988, August 1965.

[53] K. E. Browne, R. J. Burkholder, and J. L. Volakis. Through-wall opportunistic sensing system utilizing a low-cost flat-panel array. *Antennas and Propagation, IEEE Transactions on*, 59(3):859 –868, March 2011.

[54] R. J. Burkholder, P. Chang, Y. Bayram, R. J. Marhefka, and J. L. Volakis. Model-based near-field imaging of objects inside a room. In *Antennas and Propagation Society International Symposium, 2007 IEEE*, pages 1469 –1472, June 2007.

[55] J. H. G. Ender and J. Klare. System architectures and algorithms for radar imaging by MIMO-SAR. *Radar Conference, 2009 IEEE*, pages 1–6, May 2009.

[56] *2.5V / 3.3V 1:10 Differential ECL/PECL/HSTL Clock Driver*. available online at `http://www.onsemi.com/pub_link/Collateral/MC100LVEP111-D.PDF`. Rev. 17.

[57] Herman Schutte. Bi-directional level shifter for I^2C-bus and other systems. Technical report, Philips Semiconductors Systems Laboratory Eindhoven, The Netherlands, 1997.

[58] *Quicgate Cyclone II EP2C8 ControllerFPGA Module*. available online at `http://www.dallaslogic.com/prod_quicgate.htm`, 2011.

[59] Mark A. Richards. *Fundamentals of Radar Signal Processing.* McGraw-Hill, 2005.

[60] Nicholas Willis. *Bistatic Radar.* SciTech Publishing, 2nd edition, 2005.

[61] Wen-Qin Wang, Qicong Peng, and Jingye Cai. Novel MIMO SAR for urban remote sensing applications. *The International Archives of the Photogrammetry, Remote Sensing and Spatial Information Sciences*, XXXVII(B6b):139–144, 2008.